UCLA
UCLA Electronic Theses and Dissertations

Title
Controlled Stabilization of Alfv&#65533;n Eigenmodes in DIII-D and Validation of Theory and Simulations

Permalink
https://escholarship.org/uc/item/0gv408v1

Author
Tang, Shawn

Publication Date
2021

Peer reviewed|Thesis/dissertation

eScholarship.org Powered by the California Digital Library
University of California

UNIVERSITY OF CALIFORNIA
Los Angeles

Controlled Stabilization of Alfvén Eigenmodes in DIII-D and Validation of Theory and Simulations

A dissertation submitted in partial satisfaction
of the requirements for the degree
Doctor of Philosophy in Physics

by

Shawn Tang

2021

© Copyright by
Shawn Tang
2021

ABSTRACT OF THE DISSERTATION

Controlled Stabilization of Alfvén Eigenmodes in DIII-D and Validation of Theory and Simulations

by

Shawn Tang
Doctor of Philosophy in Physics
University of California, Los Angeles, 2021
Professor Troy A. Carter, Chair

Understanding the interaction between wave excitation and damping is essential in the advancement of research on magnetized plasmas in space, laboratory, and astrophysical settings. Alfvén waves can be excited across all of these settings, and in fusion research plasmas such as tokamak plasmas, they are present due to energetic particles from neutral beam injection and fusion reactions. The interplay between wave-particle interaction and damping processes is at the core of understanding wave excitation.

In the work presented in this dissertation, an experiment was designed to investigate high frequency Alfvén waves excited through Doppler-shifted cyclotron resonance with energetic particles from neutral beam injection in the DIII-D tokamak. These waves, compressional (CAE) and global (GAE) Alfvén eigenmodes, typically have frequencies close to the ion cyclotron frequency f_{ci}; the frequency and amplitude of these modes was measured with the Ion Cyclotron Emission (ICE) diagnostic. The experiment utilized the unique capability of the DIII-D neutral beams to separately control the energy and injection rate. A parametric scan across many magnetic fields and beam geometries was performed to study the dependencies of these modes on various plasma parameters.

An energetic ion density threshold was observed during a discharge in which the voltage of an off-axis co-injecting beam was held constant while the current was ramped down by 40%. During this discharge, a spectrum of high frequency AEs at $f = 0.58 f_{ci}$ was stabilized via a controlled energetic ion density ramp for the first time in a fusion research

plasma. This observation demonstrates an important property of resonant AEs: that the growth rate of these waves is set by the balance between fast-ion drive and damping processes. The controlled stabilization of this mode also validates previous simulations done on high frequency AEs in which an instability threshold was observed by varying the beam density without changing the shape of the distribution.

The scaling of the amplitude of this wave with the beam injection rate was found to be consistent with predictions for single mode collisional saturation near marginal stability. Analytic theory found that for the observed beam injection rate threshold, the mode was near marginal stability throughout the entire beam ramp. This is notably different from previous simulations of CAEs/GAEs that were in the collisionless regime and often far from marginal stability.

Modeling codes such as TRANSP and ORB_GC were used to model and analyze the fast-ion distribution for this discharge. This analysis found that the modes were likely excited by a high energy subset of the fast-ion population with strong gradients in parallel velocity space. Resonance analysis of this subset of the fast-ion population, in conjunction with considerations from dispersion relations, shows that the mode is likely a shear-polarized GAE. This marks the first identification of a GAE excited through Doppler-shifted cyclotron resonance with sub-Alfvénic energetic ions, a first in fusion research plasmas.

The dissertation of Shawn Tang is approved.

Christoph Niemann

George Morales

Walter Gekelman

Neal A. Crocker

Troy A. Carter, Committee Chair

University of California, Los Angeles

2021

To Mom and Dad

TABLE OF CONTENTS

1 Introduction **1**

1.1 Tokamaks 2

1.1.1 Flux functions 3

1.1.2 Particle orbits 4

1.2 MHD instabilities 5

1.2.1 The sawtooth instability 7

1.3 Motivation 9

1.4 Outline of the dissertation 11

2 Theoretical background of Doppler-shifted cyclotron resonant Alfvén eigenmodes **12**

2.1 MHD Waves 13

2.2 Waves in an anisotropic medium 16

2.3 Dielectric tensor in cold plasma approximation 17

2.4 Dispersion relation 18

2.5 Eigenmodes and radial structure in a tokamak 19

2.5.1 Compressional Alfvén eigenmodes 19

2.5.2 Global Alfvén eigenmodes 20

2.6 Fast-ion drive for anisotropic beam distribution 23

2.7 Resonance condition 25

2.8 Damping sources 26

3 The DIII-D tokamak **29**

3.1 Overview of DIII-D 29

3.2 Neutral beam injection . . . 30
3.2.1 Beam geometry . . . 32
3.2.2 Variable beam perveance . . . 34
3.3 Diagnostics on DIII-D . . . 36
3.3.1 Motional Stark effect (MSE) . . . 37
3.3.2 Charge exchange recombination (CER) . . . 37
3.3.3 Electron cyclotron emission (ECE) . . . 40
3.3.4 Thomson scattering . . . 40
3.3.5 Multi-channel CO_2 interferometer . . . 42
3.3.6 Fast-ion loss detector (FILD) . . . 42
3.3.7 Fast-ion deuterium-alpha detector (FIDA) . . . 45
3.4 Magnetic fluctuation measurements via ICE coils . . . 46
3.4.1 Data analysis . . . 49

4 Experimental design . . . 51
4.1 Plasma conditions and considerations . . . 51
4.2 Parametric scans . . . 52
4.2.1 Beam perveance scans . . . 55
4.2.2 Magnetic field scans . . . 57
4.3 Measurements of Alfvén eigenmodes . . . 57
4.3.1 Dependence on beam geometry . . . 58
4.3.2 Dependence on other plasma parameters . . . 59

5 Controlled fast-ion density ramp stabilizing AEs . . . 64
5.1 Stabilization of AEs . . . 65
5.2 Effects of sawtooth oscillations on mode stability . . . 69

5.2.1 The Kadomtsev Model 69
5.2.2 Sawtooth oscillations during experiment 72
5.3 Damping considerations 74
5.4 Beam current scaling with mode power 76
5.5 Comparison of AE frequency and amplitude with theoretical expectations . . 79
5.5.1 Orbit-averaged resonance condition 79
5.5.2 Modeling codes 79
5.5.3 The ORB_GC code 79
5.5.4 The TRANSP code 80
5.5.5 Equilibrium reconstruction via EFIT 82
5.5.6 The hybrid MHD code HYM 83
5.6 Analysis of fast-ion population with TRANSP 85
5.7 Identification of a GAE 87
5.8 Comparison with analytic theory 88

6 Summary and Conclusions 92
6.1 Review of results 92
6.2 Diagnostic development 93
6.3 Future work 93

LIST OF FIGURES

1.1 B_t, B_p, and I_p in a tokamak. The total magnetic field (shown in red) causes the field lines to follow a helical trajectory around the torus. Typical coordinates of a tokamak are also shown (z, R, a, φ, θ). The magnetic axis, at R_0, is shown in green. 2

1.2 (a) The banana orbit of a trapped particle with its projection onto a poloidal plane. (b) Diagram illustrating drift surfaces for the orbit of a passing particle. (c) Diagram illustrating drift surfaces for the banana orbit of a trapped particle. Figures taken from Ref.[1]. 6

1.3 Electron cyclotron emission (ECE) diagnostic data showing the temperature at (a) the core of the plasma and (b) the edge. 8

1.4 Taken from Ref. [7]. The correlation between GAE activity, T_e flattening, and an increase in χ_e in NSTX H-mode discharges heated by neutral beams at varying powers. 9

2.1 Magnetic field perturbation of MHD waves: (a) shear Alfvén waves propagate parallel to the magnetic field and (b) magnetosonic waves propagate perpendicular to the magnetic field. 15

2.2 From Ref. [14], the CAE mode structure is calculated from simulation. The effective potential V_{eff} is shown in black with the shaded region marking where $V_{\text{eff}} < 0$ and the wave can propagate. The primary mode fluctuation $\delta B_{\parallel}$ is localized in this potential well. The other fluctuations, $\delta B_{\perp}$ and $\delta E_{\parallel}$, near major radius $R = 0.6$ m, arise due to mode conversion to a kinetic Alfvén wave at the location of the resonance where $V_{\text{eff}} = 0$. 19

2.3 Taken from Ref. [10], showing the dispersion relation for a $n = 4$ shear Alfvén wave in the cylindrical approximation without toroidal coupling (dashed lines) and in the toroidal approximation (solid). 21

2.4 Taken from Ref. [18], (a) the Alfvén continuum for $n = -3$ in an NSTX plasma calculated by the NOVA simulation code, with GAE frequency shown by the dashed line; (b) the mode structure of the GAE for two dominant poloidal harmonics. 22

3.1 Cutaway view of DIII-D showing three of the four neutral beam injectors [37]. . 30

3.2 The anatomy of a DIII-D beamline, taken from the DIII-D internal website. . . 32

3.3 Top view of DIII-D showing the neutral beam system. An example beam injection geometry is labeled for the beam at 150 for the tangential and perpendicular beamlines. The two ICE systems are also shown at their approximate location on the machine [44]. 33

3.4 The voltage of the 150R beam is held constant while the beam current is ramped down by approximately 40%, taken from discharge #172026. 35

3.5 Taken from Ref. [42]. This schematic shows the geometry of the 16-chord MSE diagnostic on DIII-D. 38

3.6 (a) The plan view and (b) the cross section view of the CER system, showing where the chords are in the DIII-D vessel. 39

3.7 Electron temperature (T_e) profile as a function of normalized effective plasma radius ρ for a DIII-D discharge measured from the ECE radiometer [6]. 40

3.8 Viewing chords of the DIII-D Thomson scattering system. The red lines indicate the chords on the core laser path; the blue indicate chords on the divertor path; and the green indicate the horizontal/tangential chords. 41

3.9 The two-color interferometer layout on DIII-D [54]. 43

3.10 A schematic of the FILD diagnostic [55]. 44

3.11 (a) Cross-section and (b) plan view of DIII-D showing poloidal projection of the 2 FIDA systems and their viewing chords, taken from Ref. [57]. 45

3.12 The ICE diagnostic consisting of (a) a set of antenna straps at 180°, (b) a set of tile antennae at 240°, and a tile probe used for bandpass measurements [44]. . 47

3.13 Electronic components of the ICE diagnostic [44]. 48

3.14 An example of the raw signal obtained from one of the magnetic field sensing loops of ICE System 2. Several bursts of magnetic fluctuations are seen in response to neutral beam injection. 50

4.1 For this experiment, the plasma was chosen to be an inner wall-limited, elliptical plasma. The flux surfaces from an equilibrium reconstruction are shown, with the last closed flux surface shown in bold. 53

4.2 The beam programming for the experiment. Each of the six beams with different injection geometries is cycled through during each discharge, preceded by a < 100 ms period of diagnostic beam blips. 54

4.3 Diagnostic beam blips used during the experiment. These blips occurred before the start of each beam-on period. 55

4.4 Beam perveance scans performed during the experiment. Sequentially, the beam current and voltage were varied separately. 56

4.5 The toroidal magnetic field B_t was ramped from $\sim 2.0 \rightarrow 1.3$ T during a magnetic field scan. The plasma current I_p was ramped concurrently to keep B_t/I_p constant. 57

4.6 During a $B_t = 1.28$ T discharge, beam injection rate scans were performed at constant high beam voltage of $V_b \sim 75$ keV for six different beam geometries. Different beams excited modes at different frequencies, and four of the six total geometries were found to excite modes. 58

4.7 A B_t threshold of ~ 1.6 T was observed for the excitation of high frequency AEs during a B_t ramp discharge. 60

4.8 The $0.5 f_{ci}$ line is plotted on top of the AE spectrum during a B_t ramp, showing that the frequencies of the modes are consistent with analytic theory predicting unstable AEs above $f/f_{ci} > 0.5$. 61

4.9 The Alfvén velocity v_A is plotted on top of the AE spectrum during a B_t ramp, showing that the frequency of the modes is proportional to v_A. 61

4.10 An n_e scan in which the electron density is increased by a factor of ~ 2 shows the frequencies of the unstable modes are not proportional to the Alfvén speed v_A. 62

4.11 Within a burst of mode activity, the frequency scales with the Alfvén speed (drawn in green). 63

5.1 Profiles for ion temperature T_i, electron temperature T_e, electron density n_e, and tokamak safety factor q during the experiment. 66

5.2 (a) $|\delta b|^2$ spectrum on a logarithmic scale showing a highly coherent spectrum of high-frequency Alfvén eigenmodes at $f \sim 5550$ kHz. (b) The raw fluctuation trace from the ICE loops. (c) Mode power $|\delta b|^2$ versus time and (d) beam injection rate versus time. Mode onset is ~ 10 ms after turn-on of the 150R beam, and the mode shuts off once beam injection rate crosses a threshold of ~ 18.5 A. 68

5.3 Mode power versus frequency at mode onset ($t = 2260$ ms) shows the highest power, narrow band peak at 5520 kHz. 69

5.4 (a) The raw fluctuation trace from the ICE loops and (b) the RMS power, averaged over each 1 μs, versus time for the time range during which the mode is excited. 70

5.5 (a) The raw fluctuation trace from the ICE loops and (b) the RMS power, averaged over each 1 μs, versus time for the time range during which the mode is stabilized and then briefly re-excited. (c) The time window around mode stabilization in detail showing the exponential decay of the voltage envelope. 71

5.6 Development of the magnetic field structure during the sawtooth instability according to Kadomtsev's model, following Ref. [1]. The shaded region shows where $q < 1$, and the $m = 1$ instability displaces it and restores q at the core to unity. 72

5.7 ECE data showing electron temperature at the outer region of the plasma modulating during sawtooth oscillations. The red line indicates the time that the 150R beam turns on. 73

5.8 (a) Electron density and (b) electron temperature at the magnetic axis over the time range of the current ramp, calculated from TRANSP. 75

5.9 The poloidal electron beta of the plasma during the current ramp, calculated from TRANSP. 76

5.10 Mode power $|\delta b|^2$ versus beam injection rate I_b shows that the mode is unstable for a threshold of $I_b \sim 18.5$ A. The theoretical scaling $|\delta b|^2 \sim (1 - I_{b,\text{threshold}}/I_b)$ [68] is shown in red. 77

5.11 From Ref. [28], the growth rate γ of a CAE is shown versus the beam density. . 78

5.12 Neutron emission rates from measurement and from TRANSP simulation show good agreement in this study from Ref. [72]. 81

5.13 Taken from Ref.[28]. Frequency versus toroidal mode number for GAEs (red) and CAEs (blue) from experimental measurements and HYM simulations. . . . 84

5.14 Fast-ion density as a function of pitch $v_\parallel/v$ and energy in keV, for times (a) before beam turn-on and (b) after mode onset, averaged over $\rho < 0.3$. The resonance lines for $n = -28, p = 0, 5$ are plotted. 86

5.15 Predictions from analytic theory showing counter-propagating GAEs driven unstable by NBI with normalized injection velocity $v_0/v_A = 0.8$ and $v_\parallel/v \approx 0.3$ at frequencies of $0.5 < f/f_{ci} < 0.8$ 90

LIST OF ACRONYMS

MHD	Magnetohydrodynamics
ICE	Ion Cyclotron Emission
AE	Alfvén Eigenmode
CAE	Compressional Alfvén Eigenmode
GAE	Global Alfvén Eigenmode
DCR	Doppler-shifted Cyclotron Resonance
NBI	Neutral Beam Injection
VBP	Variable Beam Perveance
ELM	Edge Localized Mode
OMFIT	One Modeling Framework for Integrated Tasks
FFT	Fast Fourier Transform
ICRF	Ion Cyclotron Range of Frequencies
PCS	Plasma Control System
MSE	Motional Stark Effect
CER	Charge Exchange Recombination
ECE	Electron Cyclotron Emission
BES	Beam Emission Spectroscopy
PCI	Phase Contrast Imaging
FILD	Fast-Ion Loss Detector
FIDA	Fast-Ion Deuterium-Alpha
EMIC	Electromagnetic Ion Cyclotron
NSTX	National Spherical Torus Experiment
JET	Joint European Torus
TEXTOR	Tokamak Experiment for Technology Oriented Research
MAST	Mega Ampere Spherical Tokamak
PPPL	Princeton Plasma Physics Laboratory

LIST OF SYMBOLS

a	minor radius of tokamak	cm
R_0	major radius of magnetic axis	cm
R	major radius coordinate	cm
r	minor radius coordinate	cm
φ	toroidal angle	rad
θ	poloidal angle	rad
B_t	toroidal magnetic field	T
B_p	poloidal magnetic field	T
I_p	plasma current	MA
β	plasma beta	
p	plasma pressure	Pa
ρ_r	gyroradius	m
ρ_{eff}	normalized effective plasma radius	
ρ_m	mass density	kg/cm^3
ψ	magnetic flux function	
ψ_N	normalized toroidal flux	
q	tokamak safety factor	
n_e	electron density	cm^{-3}
T_e	electron temperature	keV
q	tokamak safety factor	
Π	beam perveance	
V_b	beam voltage	keV
I_b	beam current	A
n_b	beam density	cm^{-3}
v_b	beam velocity	m/s
v_A	Alfvén velocity	m/s
k	wave number	m^{-1}

f	frequency	Hz
t	time	s
χ	pitch	
ω	angular frequency	rad/s
ω_{ci}	ion cyclotron frequency	rad/s
ω_ϕ	toroidal orbit frequency	rad/s
ω_θ	poloidal orbit frequency	rad/s
$\langle \cdots \rangle$	orbit-averaged quantity	
n	toroidal mode number	
m	poloidal mode number	
s	toroidicity-induced sideband number	
$\lvert\delta b\rvert^2$	mode power	arb.
γ	mode growth rate	
γ_d	mode growth rate from fast-ion drive	
γ_L	mode damping rate	
c	speed of light	3.0×10^8 m/s
μ_0	vacuum permeability	$4\pi \times 10^{-7}$ N/A^2
ϵ_0	vacuum permittivity	8.85×10^{-12} F/m
m_i	ion mass	3.34×10^{-27} kg
m_e	electron mass	9.11×10^{-34} kg
q_e	electron charge	1.602×10^{-19} C

ACKNOWLEDGMENTS

First and foremost, I would like to thank my advisors, Professor Troy Carter and Dr. Neal Crocker. Thank you for your steadfast support and boundless patience, and above all else for the kindness you showed me throughout the years.

I am grateful to my many collaborators at UCLA, NSTX(-U), and DIII-D for answering my endless questions and always going above and beyond to help. Among these are Tony Peebles, Steve Vincena, Lothar Schmitz, Terry Rhodes, Walter Gekelman, and George Morales at UCLA; Walter Guttenfelder, Stan Kaye, Eric Fredrickson, and Nikolai Gorelenkov at PPPL; and Craig Petty, David Pace, Mike Van Zeeland, Richard Buttery, Brian Grierson, Bob Pinsker, and the rest of the DIII-D team.

I want to especially thank Elena Belova and Jeff Lestz for all the helpful discussions and collaboration on research. It was truly my privilege to work with you and I hope we can continue to work together in the future. Another thank you is owed to Bill Heidbrink for everything he taught me about energetic particles, Alfvén waves, and being an experimentalist.

I also want to thank Kathreen Thome for her mentorship and guidance over the years. Thank you for supporting me throughout my graduate career, for inspiring me to pursue fusion research, and most of all for being an amazing friend.

I am grateful for the friends I made during graduate school at UCLA: Eve Emmanuelidu, Erin Hansen, Seth Pree, Gary Chen, Riju Dasgupta, Sam Witte, Rhyan Ghosh, Ana Martynova, and Trey Elson for the late nights and early mornings, and for being my family away from home.

To Jeff Robertson, thank you for your unwavering friendship, for having faith in me, and for knowing my worth when I didn't know it myself.

A special thanks to my best friend, Sheila Ho. At times the light of your love was the only thing guiding me forward. I would not be where I am without you.

I want to thank the mental health teams at the UCLA Resnick Hospital, at Balance Treatment Center, and at Resilience Treatment Center for... everything. For the

immeasurable kindness they showed me. And a particularly special thank you to Dr. Amy Crowder for showing me how to be vulnerable, and above all, how to be kind to myself.
I am grateful to Megan Chun for being my quarantine partner and for bringing sanity back into my life at a time where there wasn't a lot of it.
Thank you to those whose love and support have guided me over the years: An, Brian, Long, Shannon, Raechel, Emily, Shadi, Brita, and Omar.
To Josh Winner, thank you for helping me find the beauty in this world again.
Thank you to Charlie and to Oliver, for loving me.
Finally, I want to thank my crazy, weird family. To my brothers, Evan, Andrew, and Elliott: thank you for watching over me and picking me up when I fall. To my chemist parents who raised a physicist daughter: thank you for always believing in me, for fostering my love of science, for never letting me think for a second that I could be anything less than brilliant.

VITA

2013	B.A., Physics University of California, Berkeley
2015	M.S., Physics University of California, Los Angeles
2012	Berkeley Physics Undergraduate Research Scholar
2014-15	UCLA Graduate Student Association Representative
2018	U.S. DOE Office of Science Graduate Student Research (SCGSR) Award

PUBLICATIONS AND PRESENTATIONS

Tang, S.X., Carter, T.A., Crocker, N.A., Heidbrink, W.W., Pinsker, R.I., Thome, K.E., Van Zeeland, M.A., Belova, E.V., Lestz, J.B. "Stabilization of Alfvén Eigenmodes in DIII-D via Controlled Energetic Ion Density Ramp and Validation of Theory and Simulations." Physical Review Letters **126**, 155001 (2021).

Invited Talk, 62nd Annual APS-DPP. S.X. Tang with Carter, T.A., Crocker, N.A., Heidbrink, W.W., Lestz, J.B., Pinsker, R.I., Thome, K.E., Van Zeeland, M.A., and Belova, E.V. "Stabilization of Alfvén Eigenmodes in DIII-D via Controlled Energetic Ion Density Ramp and Validation of Theory and Simulations." Memphis, TN (2020).

CHAPTER 1

Introduction

Nuclear fusion has long been considered the future of clean energy. For decades, scientists have sought to understand how to harness the energy released as a result of a reduction in total mass during the fusion reactions of hydrogen nuclei – the same reactions that power the sun. To do so would promise a nearly endless supply of energy without carbon emissions, as the fuel sources for nuclear fusion reactions are deuterium, found readily in sea water, and tritium, which can be obtained from lithium, an abundant resource.

$$\begin{aligned} D^2 + T^3 &\rightarrow He^4 + n^1 + 17.6 \text{ MeV} \\ D^2 + D^2 &\rightarrow He^3 + n^1 + 3.27 \text{ MeV} \\ D^2 + D^2 &\rightarrow T^3 + H^1 + 4.03 \text{ MeV} \\ D^2 + He^3 &\rightarrow He^4 + H^1 + 18.3 \text{ MeV} \end{aligned} \tag{1.1}$$

Eq.1.1: Nuclear fusion reactions that can occur with deuterium [1].

The main challenge in obtaining a positive energy balance in fusion reactions is maintaining the high temperature and density of the particles for a sufficiently long time. Thermonuclear fusion refers to the process by which the thermal velocities of the nuclei are increased through heating to induce the required reactions [1]. At the required temperature for this to occur (over 100 million degrees Celsius), the particles are fully ionized and form a plasma. Confinement of a plasma presents its own challenges, and devices like the z-pinch [2] and the stellarator [3] have attempted to achieve a stable plasma equilibrium without significant success. The tokamak is a device that confines

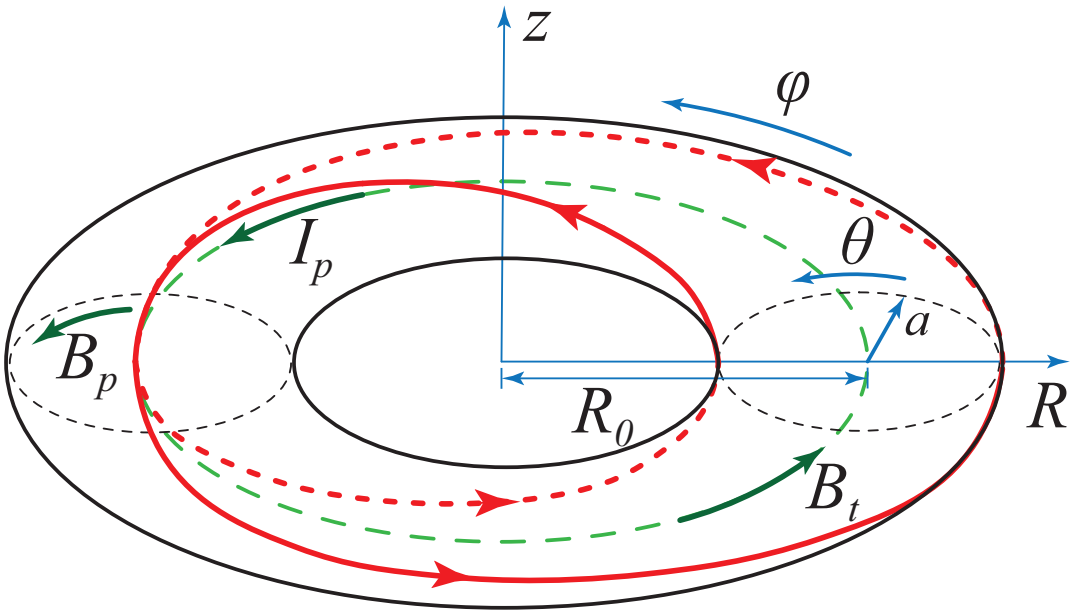

Figure 1.1: B_t, B_p, and I_p in a tokamak. The total magnetic field (shown in red) causes the field lines to follow a helical trajectory around the torus. Typical coordinates of a tokamak are also shown (z, R, a, φ, θ). The magnetic axis, at R_0, is shown in green.

plasma in a toroidal geometry through strong electromagnetic fields, and is considered the leading candidate for a fusion reactor with break-even or positive energy output.

1.1. Tokamaks

Tokamaks confine plasma toroidally through a magnetic field. The primary component of the magnetic field is toroidal (B_t) and produced through strong poloidal currents in external coils. The plasma itself produces a toroidal current (I_p), which then gives rise to a poloidal magnetic field B_p (it should be noted that the B_p is also comprised of other sources such as coils used for plasma shaping). An illustration of B_t, I_p, and B_p is shown in Fig. 1.1. From Ampère's law, the variation of the toroidal field with respect to radius can easily be found to be $B_t \propto 1/R$ [1].

The total magnetic field, formed by B_t and B_p, follows a helical trajectory around the torus. An illustration of a field line is shown in Fig. 1.1 in red. Fig. 1.1 also shows the

toroidal coordinate system, where R is the major radius, a is the minor radius, θ is the poloidal angle, and φ is the toroidal angle. R_0 indicates the magnetic axis, and the aspect ratio of a tokamak is defined as the ratio of the major radius to the minor radius R/a. Because axisymmetric equilibria (independent of toroidal angle φ) is generally considered in tokamaks, a cylindrical coordinate system (R, z, φ) is often used.

The total field can be visualized as an infinite set of toroidal magnetic surfaces, with field lines that wind around the torus on their respective magnetic surface in a helix [1]. Considering axisymmetric equilibrium, the magnetic force on the plasma must balance the force due to the plasma pressure. This implies that magnetic surfaces are surfaces with no pressure gradient. These magnetic surfaces are referred to as magnetic flux surfaces, as the poloidal magnetic flux function ψ is a constant on each surface. This flux function is important in solving for tokamak equilibria, and a more in-depth derivation and explanation follows in the next section. The normalized effective plasma radius ρ_{eff} based on toroidal flux is often used in tokamak physics, where $\rho_{\text{eff}} = \sqrt{\psi_N}$, and ψ_N is the normalized toroidal flux, with $\psi = 0$ at the magnetic axis and $\psi = 1$ at the last closed flux surface.

The safety factor q in a tokamak describes the relative "twist" of a field line. Each field line follows a helical trajectory along its corresponding flux surface, and returns to its starting point after some change of toroidal angle $\Delta\varphi$. The q-value of this line would then be $q = \frac{\Delta\varphi}{2\pi}$. Fig. 1.1 shows a $q = 2$ field line in red that returns to its starting point after two rotations around the torus. An approximate definition of q in a tokamak is $q = \frac{aB_t}{RB_p}$. It is also apparent that each flux surface has a constant q.

1.1.1. Flux functions

The magnetic force must balance the force due to the plasma pressure at all points in the plasma, and this can be expressed as:

$$\boldsymbol{J} \times \boldsymbol{B} = \nabla p \tag{1.2}$$

where $\boldsymbol{J}$ is the current density.

From this it follows that

$$\begin{aligned} \boldsymbol{B} \cdot \nabla p &= 0 \\ \boldsymbol{J} \cdot \nabla p &= 0 \end{aligned} \tag{1.3}$$

which indicates that magnetic surfaces have constant pressure, and that current lines lie in magnetic surfaces.

The poloidal magnetic flux function ψ is a function that is determined by the poloidal flux in each magnetic surface. ψ is necessarily a constant on each surface, so

$$\boldsymbol{B} \cdot \nabla \psi = 0 \tag{1.4}$$

Using a cylindrical coordinate system, since $\nabla \cdot \boldsymbol{B} = 0$,

$$\frac{1}{R}\frac{\partial}{\partial R}(RB_R) + \frac{\partial B_z}{\partial z} = 0 \tag{1.5}$$

it follows that the poloidal magnetic field is related to the poloidal magnetic flux function ψ as:

$$B_R = -\frac{1}{R}\frac{\partial \psi}{\partial z}, \qquad B_z = \frac{1}{R}\frac{\partial \psi}{\partial R} \tag{1.6}$$

There necessarily also exists a current flux function $f = f(\psi)$ and is related to poloidal current density as:

$$J_R = -\frac{1}{R}\frac{\partial f}{\partial z}, \qquad J_z = \frac{1}{R}\frac{\partial f}{\partial R} \tag{1.7}$$

It also follows that

$$f = \frac{RB_\varphi}{\mu_0} \tag{1.8}$$

This derivation was taken from Ref. [1].

1.1.2. Particle orbits

A charged particle in a uniform magnetic field follows a Larmor orbit, which is a helical orbit comprised of a circular orbit with gyroradius $\rho_r = \frac{mv_\perp}{qB}$ with constant velocity along the magnetic field, where m is the mass of the particle, $v_\perp$ is the velocity perpendicular to

the field, q is the charge, and B is the magnitude of the magnetic field. In a non-uniform magnetic field, this motion is subject to drifts of the guiding center of the Larmor orbit due to $\boldsymbol{E} \times \boldsymbol{B}$ effects, ∇B effects, curvature of B, and/or polarization effects from a time-varying electric field $\boldsymbol{E}$. An in-depth derivation of these drifts can be found in Ref. [1].

In tokamaks, the non-uniform magnetic field results in two types of guiding center orbits: passing and trapped. Passing particles will orbit around the torus because they have an adequately large parallel velocity with respect to the magnetic field, and their trajectory is illustrated in Fig. 1.2(b). Trapped particles have low parallel velocity with respect to the magnetic field. Because B_t varies as $1/R$, the outer side of the torus has a weaker magnetic field. As particles move towards the region of higher field, they undergo a magnetic mirror effect that causes their trajectory to reflect [1]. These particles are trapped in the low field side of the torus, bouncing back and forth, and the orbit of these trapped particles is known as a banana orbit. Fig. 1.2(a) shows the banana orbit and its projection onto a poloidal plane, and Fig. 1.2(c) shows the trajectory of a trapped particle.

1.2. MHD instabilities

Tokamaks are subject to a wide range of instabilities, including equilibrium scale events that can disrupt plasma confinement and cause current collapse, such as edge localized modes (ELMs) or neoclassical tearing modes [1]. The results presented in this thesis are from L-mode (low confinement) discharges in DIII-D. In comparison to H-mode (high confinement) plasmas, ELMs are not typically present and the effect of other instabilities that can disrupt plasma operation are reduced; this is true of the plasmas in the results discussed here. A comprehensive summary of the different types of instabilities present in tokamaks can be found in Ref. [1]. These instabilities are collectively referred to as magnetohydrodynamic (MHD) instabilities as they can be approximated by MHD plasma theory.

MHD is a model that treats the plasma as a conducting fluid in order to describe the

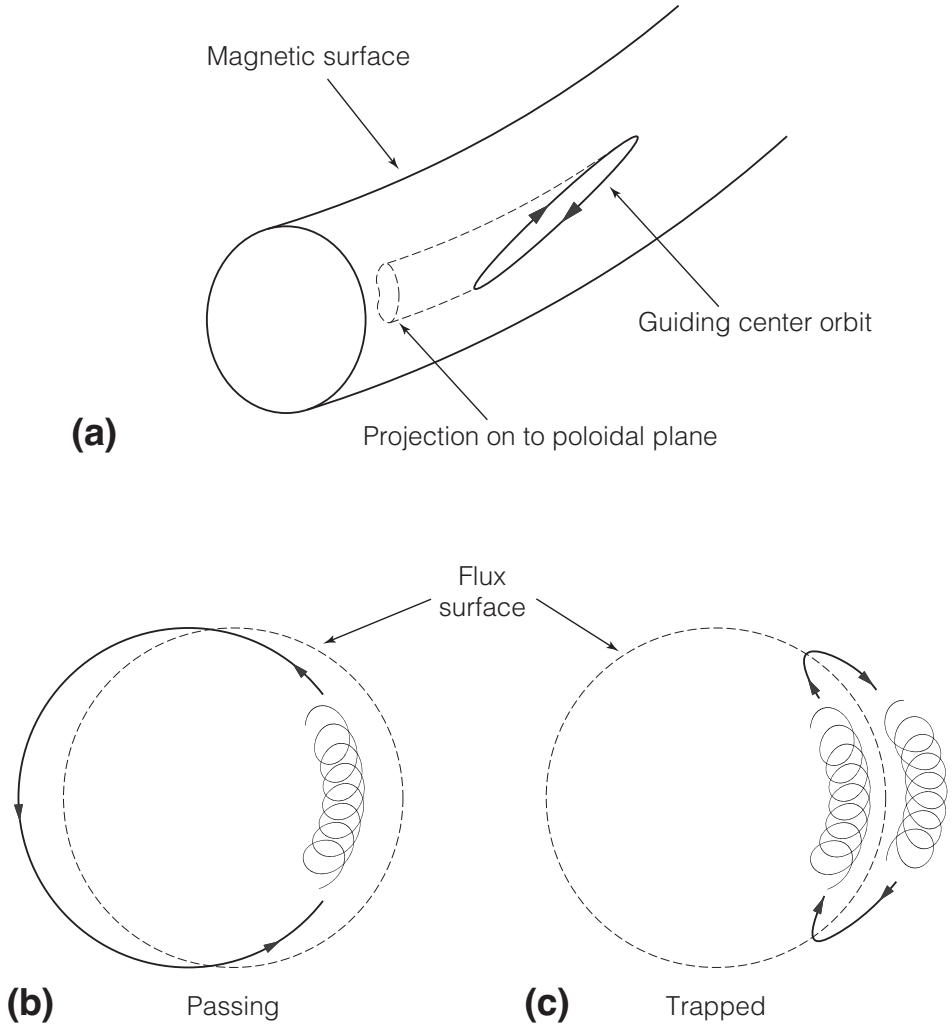

Figure 1.2: (a) The banana orbit of a trapped particle with its projection onto a poloidal plane. (b) Diagram illustrating drift surfaces for the orbit of a passing particle. (c) Diagram illustrating drift surfaces for the banana orbit of a trapped particle. Figures taken from Ref.[1].

equilibrium. Ideal MHD describes plasmas with Maxwellian particle distributions, strong collisionality, and negligible resistivity (no diffusion). It does not take into account kinetic effects. Despite its limitations, MHD theory is sufficient in describing many important properties of plasma instabilities in tokamaks and has been shown to be approximately qualitatively accurate in experiment [4].

The set of ideal MHD equations combines the fluid equations and Maxwell's equations [1]:

$$
\begin{aligned}
\frac{\mathrm{d}\rho_m}{\mathrm{d}t} &= -\rho_m \nabla \cdot \boldsymbol{v} \\
\rho_m \frac{\mathrm{d}\boldsymbol{v}}{\mathrm{d}t} &= \boldsymbol{J} \times \boldsymbol{B} - \nabla p \\
\frac{\mathrm{d}p}{\mathrm{d}t} &= -\gamma p \nabla \cdot \boldsymbol{v} \\
\mu_0 \boldsymbol{J} &= \nabla \times \boldsymbol{B} \\
\frac{\partial \boldsymbol{B}}{\partial t} &= -\nabla \times \boldsymbol{E} \\
\boldsymbol{E} + \boldsymbol{v} \times \boldsymbol{B} &= 0
\end{aligned}
\tag{1.9}
$$

Eq. 1.9: Ideal MHD equations.

where $\rho_m \simeq m_i n$ is the mass density, $\boldsymbol{v}$ is the fluid velocity, p is the plasma pressure, $\boldsymbol{J}$ is the current density, $\boldsymbol{B}$ and $\boldsymbol{E}$ are the magnetic and electric fields, $\gamma = 5/3$ is the ratio of specific heats, and μ_0 is the vacuum permeability.

These equations can be linearized to solve for instabilities that arise in MHD plasmas by perturbing quantities and solving for wave-like solutions that vary as $e^{i(\boldsymbol{k}\cdot\boldsymbol{r}-\omega t)}$, where ω is the angular frequency, $\boldsymbol{k}$ is the wavenumber, and $\boldsymbol{r}$ is the displacement. In a tokamak, toroidal axisymmetry is assumed and the equilibrium is constant along the toroidal angle φ. The eigenfunction wave solutions to the ideal MHD equations can thus be expressed as $e^{i(m\theta - n\varphi)}$ as long as the variation in the poloidal angle θ is sufficiently small [1]. Conventionally, the eigenvalues m and n are used to describe the poloidal and toroidal mode number of the corresponding wave, respectively.

1.2.1. The sawtooth instability

Sawtooth oscillations are a relaxation that occurs in the core of the tokamak, appearing as a slow rise followed by a sharp drop in temperature and density that gives the instability its name. Unlike other macro-scale instabilities, its existence does not typically lead to a disruption in plasma confinement. The plasma core recovers after each sawtooth crash, and the instability occurs repeatedly. Sawtooth oscillations are a ubiquitous instability in

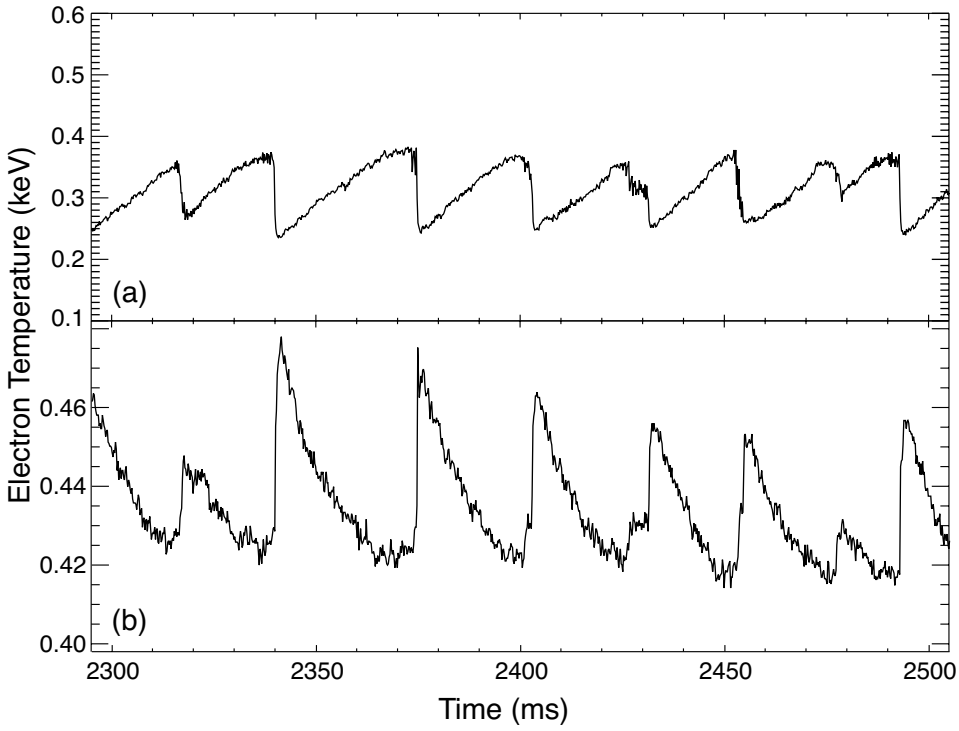

Figure 1.3: Electron cyclotron emission (ECE) diagnostic data showing the temperature at (a) the core of the plasma and (b) the edge.

that they occur under a wide range of plasma conditions in all tokamaks, both conventional and spherical.

The sawtooth instability begins with a perturbation that develops at the $q = 1$ flux surface. The temperature and density in the core of the plasma rise slowly and linearly with time, and as the core temperature increases, the q in the core drops below unity. This causes a fast collapse of the temperature and density. During this collapse, hot electrons in the core are quickly expelled and transported across flux surfaces to colder regions of the plasma, accompanied by a flattening of the temperature and density profiles [5]. The cycle repeats as core temperature and density are again increased through heating.

An example of sawteeth is shown in Fig. 1.3, where the electron temperature (T_e) is measured through the electron cyclotron emission (ECE) diagnostic [6]. Fig. 1.3(a) shows T_e in the core of the plasma during sawtooth oscillations; the temperature rises during the ramp and then experiences a crash as the thermal energy is dissipated to the outer region

of the plasma. This pattern is inverted in the outer region, as seen in Fig. 1.3(b).

1.3. Motivation

The focus of this dissertation is on compressional (CAE) and global (GAE) Alfvén eigenmodes, which are a type of MHD wave that are excited through Doppler-shifted cyclotron resonance (DCR) with energetic particles in tokamak plasmas. These waves typically have frequencies that are close to the ion cyclotron frequency f_{ci}.

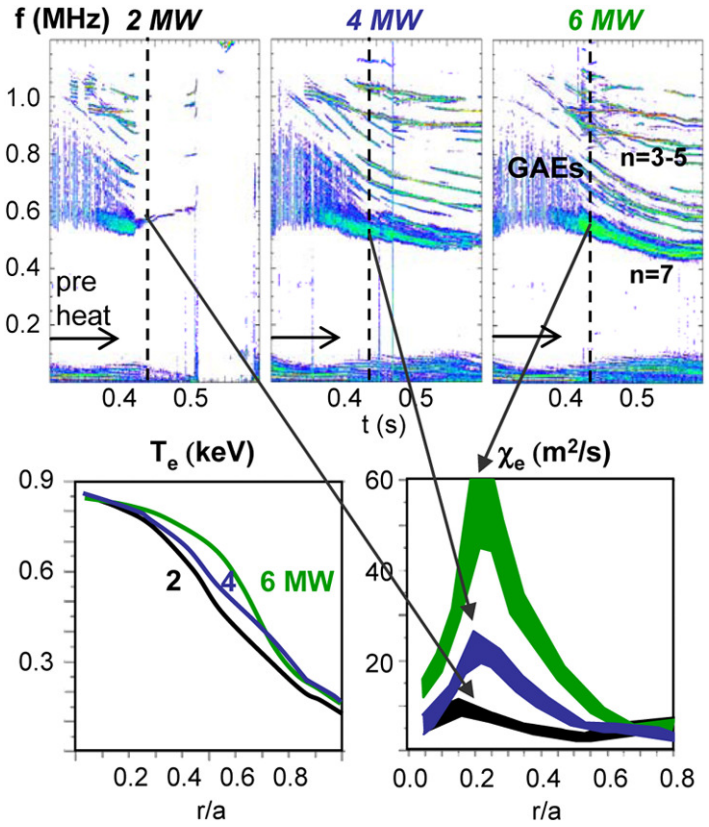

Figure 1.4: Taken from Ref. [7]. The correlation between GAE activity, T_e flattening, and an increase in χ_e in NSTX H-mode discharges heated by neutral beams at varying powers.

Understanding the interaction between Alfvén waves, energetic particle drive, and wave damping is essential in advancing research on magnetized plasmas in space, laboratory, and astrophysical settings. Alfvén waves can be resonantly excited by high energy cosmic rays and cause them to scatter, leading to transport [8]. Energetic protons in the Earth's

radiation belts can excite Electromagnetic Ion Cyclotron (EMIC) waves that contribute to scattering and precipitation of trapped relativistic electrons [9]. And in tokamak plasmas, energetic particles from heating schemes such as neutral beam injection (NBI) and fusion reactions can excite Alfvén waves by creating gradients in the ion velocity distribution at the location of the wave-particle resonance [10]. Wave-particle interaction and damping are at the core of understanding wave excitation and particle scattering processes across all of these settings.

CAEs and GAEs have been found to correlate with enhanced core electron transport in the National Spherical Torus Experiment (NSTX) [7]. This is shown in Fig. 1.4: as the power of the neutral beam increases, GAEs are excited in the plasma. GAE activity is correlated with a flattening of the electron temperature (T_e) profile, and with an increase in the electron heat diffusivity χ_e. Notably, the safety factor q-profile and the electron density n_e profile were the same in all discharges during this transport correlation. This correlation is important because it shows that advancing our understanding of the role of these waves in electron thermal transport is essential for developing a predictive capability for current and future fusion experiments. Future burning plasmas such as those on ITER will be primarily heated by NBI and energetic alpha particles from fusion reactions which can excite AEs and cause anomalous transport.

1.4. Outline of the dissertation

This dissertation focuses on the study of CAE/GAE activity in DIII-D and its dependence on plasma parameters. The major result presented here is the stabilization of a high frequency AE through a controlled energetic ion density ramp.

First, the theoretical background of these AEs, which are driven unstable through Doppler-shifted cyclotron resonance with fast-ions, is presented. The dispersion relation for these waves is derived in the finite-frequency limit ($\omega \sim \omega_{ci}$), as well as the fast-ion drive for these modes in an anisotropic beam distribution. Finally, the resonance conditions for DCR are shown.

The DIII-D tokamak and its diagnostics are discussed next, with emphasis on neutral beam injection and its capabilities. Specifically, the DIII-D tokamak features NBI that uniquely uses its ability to separately vary beam voltage and current. The various diagnostics on DIII-D will be discussed with particular emphasis on the Ion Cyclotron Emission (ICE) diagnostic, which is used to measure magnetic fluctuations and give spectral information about CAE/GAEs. This will be followed with a description of the experimental design, including plasma conditions and considerations.

Finally, the analysis showing the controlled fast-ion density ramp stabilizing the mode is presented. The comparison with analytic theory is given, showing that the mode amplitude scaling with beam injection rate is consistent with collisional saturation near marginal stability. Modeling codes are used to compare the frequency and amplitude of the AE with theoretical expectations. Specifically, TRANSP and ORB_GC are used for resonance analysis of the fast-ion population, allowing the identification of a resonant population of energetic particles that are likely responsible for mode drive. Through this analysis and considerations from dispersion relations, the mode is identified as a shear-polarized GAE, the first identification of a GAE excited by sub-Alfvénic beam ions in a fusion research plasma.

CHAPTER 2

Theoretical background of Doppler-shifted cyclotron resonant Alfvén eigenmodes

Compressional (CAE) and global (GAE) Alfvén eigenmodes are a type of MHD wave that are driven unstable by energetic ions from neutral beam injection. The free energy destabilizing these modes is provided by fast-ions that are Doppler-shifted cyclotron resonant with the AEs.

This chapter will first show CAE/GAE theory in the framework of MHD, in which CAEs correspond to the compressional and GAEs correspond to the shear branches of MHD waves. This will be generalized to show the derivation for the CAE/GAE dispersion relations in the local approximation for a cold plasma. Following, fast-ion drive and damping will be derived assuming a two-component plasma consisting of a cold bulk plasma and a hot fast-ion population. Finally, the resonance conditions for CAE/GAEs will be discussed, which includes the condition for Doppler-shifted cyclotron resonance and the orbit-averaged resonance equation.

2.1. MHD Waves

Beginning with the MHD equations, first shown in Section 1.3, which combine the fluid equations and Maxwell's equations:

$$\begin{aligned} \frac{\mathrm{d}\rho_m}{\mathrm{d}t} &= -\rho_m \nabla \cdot \boldsymbol{v} \\ \rho_m \frac{\mathrm{d}\boldsymbol{v}}{\mathrm{d}t} &= \boldsymbol{J} \times \boldsymbol{B} - \nabla p \\ \frac{\mathrm{d}p}{\mathrm{d}t} &= -\gamma p \nabla \cdot \boldsymbol{v} \\ \mu_0 \boldsymbol{J} &= \nabla \times \boldsymbol{B} \\ \frac{\partial \boldsymbol{B}}{\partial t} &= -\nabla \times \boldsymbol{E} \\ \boldsymbol{E} + \boldsymbol{v} \times \boldsymbol{B} &= 0 \end{aligned} \tag{1.9}$$

In order to solve for MHD waves, we linearize these equations by perturbing quantities and solve for wave-like solutions that vary as $\exp[i(\boldsymbol{k} \cdot \boldsymbol{r} - \omega t)]$. Equilibrium quantities will be denoted with the 0 symbol.

In Cartesian coordinates, without loss in generality we can assume that the equilibrium magnetic field is $\boldsymbol{B_0} = B_0 \hat{z}$ and the wave vector is $\boldsymbol{k} = k_\perp \hat{x} + k_\parallel \hat{z}$.

Define the Alfvén velocity as:

$$v_A^2 \equiv \frac{B_0}{\mu_0 \rho_0} = \frac{B_0}{\mu_0 n m} \tag{2.1}$$

and the sound speed as:

$$v_s^2 \equiv \frac{\gamma p_0}{\rho_0} \tag{2.2}$$

Letting θ be the angle between $\boldsymbol{B_0}$ and $\boldsymbol{k}$, for a non-trivial solution, the determinant of the matrix

$$\begin{bmatrix} \omega^2 - k^2 v_A^2 - k^2 v_s^2 \sin^2\theta & 0 & -k^2 v_s^2 \sin\theta\cos\theta \\ 0 & \omega^2 - k^2 v_A^2 \cos^2\theta & 0 \\ -k^2 v_s^2 \sin\theta\cos\theta & 0 & \omega^2 - k^2 v_s^2 \cos^2\theta \end{bmatrix} \tag{2.3}$$

must be zero.

This leads us to the dispersion relation for MHD waves:

$$(\omega^2 - k^2 v_A^2 \cos^2\theta)\left[\omega^4 - \omega^2 k^2 (v_A^2 + v_s^2) + k^4 v_A^2 v_s^2 \cos^2\theta\right] = 0 \tag{2.4}$$

or:

$$(\omega^2 - k_\parallel^2 v_A^2)\left[\omega^4 - \omega^2 k^2 (v_A^2 + v_s^2) + k^2 k_\parallel^2 v_A^2 v_s^2\right] = 0 \tag{2.5}$$

corresponding to three non-trivial solutions.

The first of these is the shear Alfvén wave, which has the dispersion relation

$$\omega = k_\parallel v_A \tag{2.6}$$

The other two solutions correspond to the slow and fast magnetosonic wave, with the dispersion relations

$$\omega = k v_\pm \tag{2.7}$$

where

$$v_\pm^2 = \frac{1}{2}\left[v_A^2 + v_s^2 \pm \sqrt{(v_A^2 + v_s^2)^2 - 4 v_A^2 v_s^2 \cos^2\theta}\right] \tag{2.8}$$

The shear Alfvén wave is a transverse wave and propagates parallel to the equilibrium magnetic field $\boldsymbol{B_0}$, while the magnetosonic wave is a longitudinal wave that propagates perpendicular to $\boldsymbol{B_0}$. In the cold plasma limit, letting $v_s \to 0$, the magnetosonic dispersion relation is reduced to

$$\omega = k v_A \tag{2.9}$$

which is the dispersion relation for the compressional Alfvén wave.

The perturbation of the magnetic field by shear and compressional Alfvén waves is shown in Fig. 2.1. Shear Alfvén waves propagate parallel to the equilibrium magnetic field B_0 and tend to bend the magnetic field lines, while magnetosonic waves propagate perpendicular to B_0 and tend to compress the magnetic field lines.

GAEs are a type of shear Alfvén wave, and CAEs are, of course, compressional. The dispersion relations for shear and compressional Alfvén waves (Eqs. 2.6 and 2.9) derived in this section apply to Alfvén waves in a cold, uniform plasma and serve as a general approximation for the AEs discussed in this dissertation. A more accurate dispersion relation is derived in the next section.

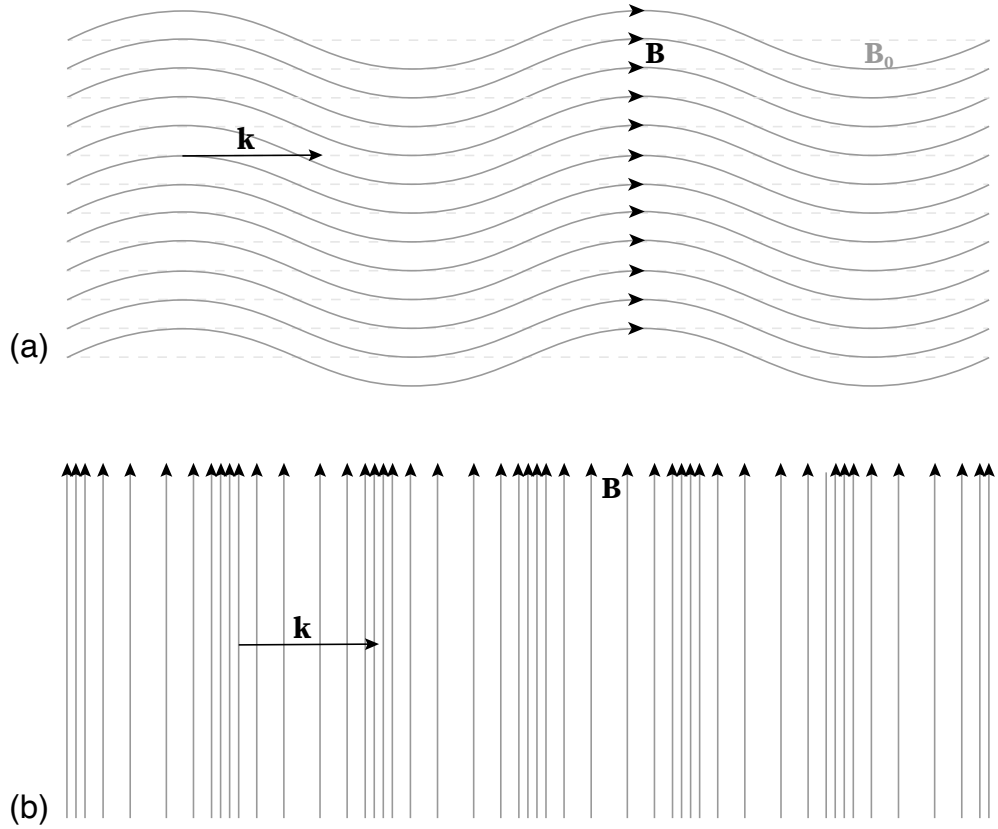

Figure 2.1: Magnetic field perturbation of MHD waves: (a) shear Alfvén waves propagate parallel to the magnetic field and (b) magnetosonic waves propagate perpendicular to the magnetic field.

2.2. Waves in an anisotropic medium

The derivation that follows is for plasma waves in an anisotropic medium. We begin with three of Maxwell's equations:

$$\begin{aligned} \boldsymbol{J} &= \overleftrightarrow{\sigma} \cdot \boldsymbol{E} \\ \nabla \times \boldsymbol{E} &= -\frac{\partial \boldsymbol{B}}{\partial t} \\ \nabla \times \boldsymbol{B} &= \frac{1}{c^2}\frac{\partial \boldsymbol{E}}{\partial t} + \mu_0 \boldsymbol{J} \end{aligned} \tag{2.10}$$

where $\overleftrightarrow{\sigma}$ is the conductivity tensor.

Again, we linearize by assuming waves of the form $\exp[i(\boldsymbol{k} \cdot \boldsymbol{r} - \omega t)]$. Define the dielectric tensor $\overleftrightarrow{\varepsilon}$ as

$$\overleftrightarrow{\varepsilon} = 1 - \frac{\overleftrightarrow{\sigma}}{i\omega\varepsilon_0} \tag{2.11}$$

where $\varepsilon_0 = 8.854 \times 10^{-12}\ \mathrm{F \cdot m^{-1}}$ is the vacuum permittivity. With some algebra, Eq. 2.10 reduces to

$$\boldsymbol{k}(\boldsymbol{k} \cdot \boldsymbol{E}) - k^2 \boldsymbol{E} + \frac{\omega^2}{c^2}\overleftrightarrow{\varepsilon} \cdot \boldsymbol{E} \tag{2.12}$$

Define the index of refraction n as:

$$n \equiv \frac{kc}{\omega} \tag{2.13}$$

Then for a non-trivial solution the following must be satisfied:

$$\left| \varepsilon_{ij} - n^2\big(\delta_{ij} - \frac{k_i k_j}{k^2}\big) \right| = 0 \tag{2.14}$$

As in the previous section, without loss in generality we may assume $\boldsymbol{B_0} = B_0\hat{z}$ and $\boldsymbol{k} = k_\perp \hat{x} + k_\parallel \hat{z}$. Additionally, in the MHD limit we may assume that E_z is negligible, so the dispersion is determined by:

$$\begin{vmatrix} \varepsilon_{11} - n_\parallel^2 & \varepsilon_{12} \\ \varepsilon_{21} & \varepsilon_{22} - n^2 \end{vmatrix} = 0 \tag{2.15}$$

2.3. Dielectric tensor in cold plasma approximation

In order to solve for the dispersion relation, the dielectric tensor must be determined. This is done so through the cold plasma formulation, in which the thermal motion of the particles is ignored (i.e. $\omega/k \gg v_{\text{th}}$). In the cold plasma formulation the plasma is assumed to be homogeneous and quasineutral; the background plasma is assumed to have $\boldsymbol{E_0} = 0$ and $\boldsymbol{B} = \boldsymbol{B_0}$. Taking $\boldsymbol{B_0} = B_0\hat{z}$, we start with the equation of motion

$$m\frac{\partial \boldsymbol{v}}{\partial t} = q(\boldsymbol{E} + \boldsymbol{v} \times \boldsymbol{B}) \tag{2.16}$$

and perturb $\boldsymbol{v}, \boldsymbol{E} \propto \exp[i(\boldsymbol{k}\cdot\boldsymbol{r} - \omega t)]$. Noting that $\boldsymbol{J} = qn\boldsymbol{v} = \overleftrightarrow{\sigma} \cdot \boldsymbol{E}$, and defining the plasma frequency as:

$$\omega_p^2 = \frac{q^2 n}{\varepsilon_0 m} \tag{2.17}$$

and the cyclotron frequency as:

$$\omega_c = \frac{qB_0}{m} \tag{2.18}$$

we arrive at a general expression for the dielectric tensor $\overleftrightarrow{\varepsilon}$, where the subscript j denotes particle species.

$$\varepsilon = \begin{bmatrix} 1 - \sum_j \frac{\omega_{pj}^2}{\omega^2 - \omega_{cj}^2} & -i\sum_j \frac{\omega_{cj}}{\omega}\frac{\omega_{pj}^2}{\omega^2 - \omega_{cj}^2} & 0 \\ i\sum_j \frac{\omega_{cj}}{\omega}\frac{\omega_{pj}^2}{\omega^2 - \omega_{cj}^2} & 1 - \sum_j \frac{\omega_{pj}^2}{\omega^2 - \omega_{cj}^2} & 0 \\ 0 & 0 & 1 - \sum_j \frac{\omega_{pj}^2}{\omega^2} \end{bmatrix} \tag{2.19}$$

This can also be written as

$$\varepsilon = \begin{bmatrix} S & -iD & 0 \\ iD & S & 0 \\ 0 & 0 & P \end{bmatrix} \tag{2.20}$$

with

$$
\begin{aligned}
S &= 1 - \sum_j \frac{\omega_{pj}^2}{\omega^2 - \omega_{cj}^2} \\
D &= \sum_j \frac{\omega_{cj}}{\omega} \frac{\omega_{pj}^2}{\omega^2 - \omega_{cj}^2} \\
P &= 1 - \sum_j \frac{\omega_{pj}^2}{\omega^2}
\end{aligned}
\tag{2.21}
$$

2.4. Dispersion relation

Using the values from the dielectric tensor $\overleftrightarrow{\varepsilon}$ found in the previous section, we solve for the dispersion relation using Eq. 2.15. Following the notation from Ref. [11], we define $\overline{\omega} = \omega/\omega_{ci0}$, $N = kv_A/\omega$, $A = \frac{1}{1-\overline{\omega}^2}$, $F^2 = k_\parallel^2/k^2$, and $G = 1 + F^2$, with ω_{ci0} being the ion cyclotron frequency on-axis. The dispersion relation in uniform geometry is

$$
N^2 = \frac{AG}{2F^2}\left[1 \pm \sqrt{1 - \frac{4F^2}{AG^2}}\right] \tag{2.22}
$$

with the "–" solution corresponding to CAEs and the "+" solution corresponding to GAEs. In the low frequency limit ($\omega \ll \omega_{ci}$) this dispersion relation reduces to Eqs. 2.6 and 2.9. Importantly, Eq. 2.22 takes into account finite-frequency effects which were precluded by previous studies of CAE/GAEs such as those in Refs. [12, 13] and others.

Finite-frequency effects also affect the polarization of CAE/GAEs [14]. In the simplest model in the MHD formulation described in Section 2.1, CAEs are polarized such that $\boldsymbol{E} = E\hat{y}$, perpendicular to the wave vector $\boldsymbol{k} = k_\perp\hat{x} + k_\parallel\hat{z}$, and propagate perpendicular to the equilibrium magnetic field $\boldsymbol{B_0} = B_0\hat{z}$; shear Alfvén waves such as GAEs are polarized such that $\boldsymbol{E} = E\hat{x}$, parallel to the perpendicular wave vector $\boldsymbol{k}_\perp = k_\perp\hat{x}$, and propagate parallel to $\boldsymbol{B_0}$. After taking into account finite-frequency effects, the polarizations of CAE/GAEs become mixed such that both waves have $|E_x| \approx |E_y|$ in the limit of $k_\parallel \gg k_\perp$ [14].

2.5. Eigenmodes and radial structure in a tokamak

In practice, CAE/GAEs are subject to spatial irregularities in toroidal geometries and thus have spatial dependence in non-uniform plasmas that depend on equilibrium plasma profiles and on the details of the toroidal geometry.

2.5.1. Compressional Alfvén eigenmodes

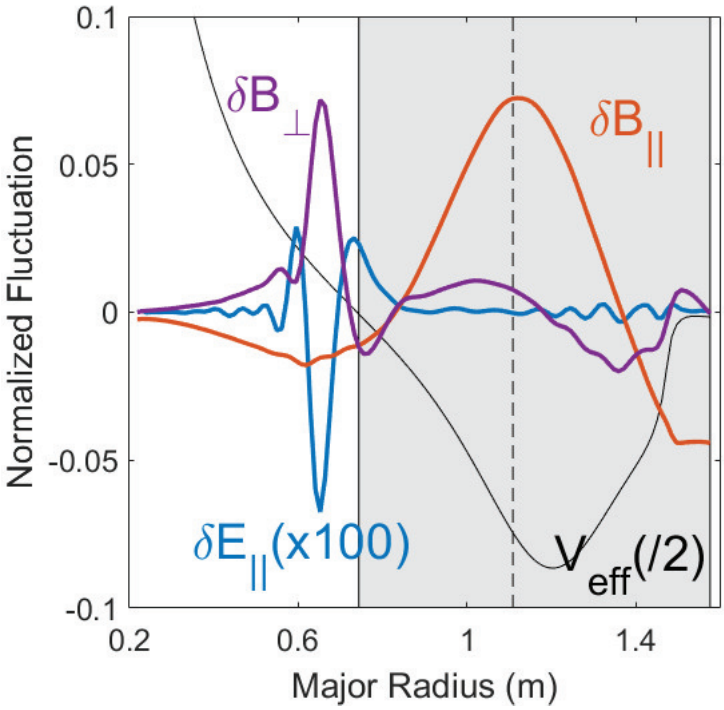

Figure 2.2: From Ref. [14], the CAE mode structure is calculated from simulation. The effective potential V_{eff} is shown in black with the shaded region marking where $V_{\text{eff}} < 0$ and the wave can propagate. The primary mode fluctuation $\delta B_{\parallel}$ is localized in this potential well. The other fluctuations, $\delta B_{\perp}$ and $\delta E_{\parallel}$, near major radius $R = 0.6$ m, arise due to mode conversion to a kinetic Alfvén wave at the location of the resonance where $V_{\text{eff}} = 0$.

In toroidal geometry, boundary conditions imposed on CAEs give rise to a discrete spectrum of eigenfrequencies and eigenfunctions. Detailed derivations of the toroidal eigenmodes have been performed in references such as Refs. [15] and [16]. For the research presented here, it is sufficient to approximate that CAEs are poloidally localized in a

effective potential "well" in the R-z plane where $V_{\text{eff}}(r,\theta) = k_{\|}^2 + \omega^2/v_A^2 \approx \frac{n^2 v_A^2}{R^2}$, such that the wave propagates in regions where $\frac{n^2 v_A^2}{R^2} - \omega^2 < 0$ and is evanescent where $\frac{n^2 v_A^2}{R^2} - \omega^2 > 0$. CAEs are typically edge-localized in tokamaks at the low field side [12]. Fig. 2.2 shows the mode structure of a CAE as calculated through simulation, taken from Ref. [14], localized within the potential well where $V_{\text{eff}} < 0$. In this simulation, the other coherent fluctuations $\delta B_\perp$ and $\delta E_\|$ arise from mode conversion to a kinetic Alfvén wave where $V_{\text{eff}} = 0$.

2.5.2. Global Alfvén eigenmodes

Shear Alfvén waves in toroidal geometry have radial dependence approximately through the general dispersion relation

$$\omega = k_\|(r) v_A(r) \tag{2.23}$$

The parallel wave vector $k_\|$ has radial dependence; in the cylindrical approximation of a tokamak plasma it can be expressed as

$$k_\| = \frac{n - m/q(r)}{R} \tag{2.24}$$

where n is the toroidal mode number, m is the poloidal mode number, r is the minor radius, R is the major radius, and $q(r) = \frac{rB_t}{RB_p}$ is the tokamak safety factor.

Shear Alfvén waves satisfying this dispersion relation are part of the Alfvén continuum. However, these waves are strongly damped through phase mixing because they have different phase velocities across its radial extent, causing rapid dispersion of the wave packet [10] – this is known as continuum damping.

In toroidal geometry, however, frequency gaps exist due to periodicity constraints on the Alfvén speed v_A [10, 17]. This is illustrated in Fig. 2.3, taken from Ref. [10]. Discrete shear Alfvén waves can exist within these frequency gaps ("gap modes") that do not experience the strong continuum damping; the most important of these is the toroidicity-induced Alfvén eigenmode (TAE) which exists due to the toroidal coupling of poloidal harmonics of continuum modes [17].

In addition to continuum and gap modes, another type of shear Alfvén wave exists in

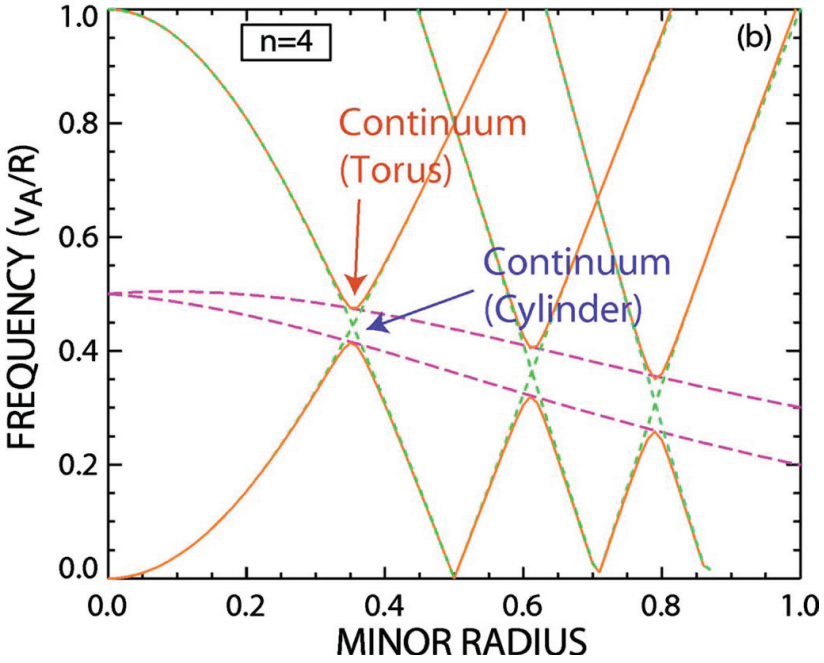

Figure 2.3: Taken from Ref. [10], showing the dispersion relation for a $n = 4$ shear Alfvén wave in the cylindrical approximation without toroidal coupling (dashed lines) and in the toroidal approximation (solid).

tokamak plasmas – "extremum" modes. These modes exist because of an extremum in the frequency of the Alfvén continuum, causing the radial variation of v_A to vanish and forming an effective potential well with radial localization near the location of the extremum (where $d(k_\parallel(r)v_A(r))/dr = 0$). These modes have frequencies just above or below an extremum in the Alfvén continuum – GAEs fall into this category.

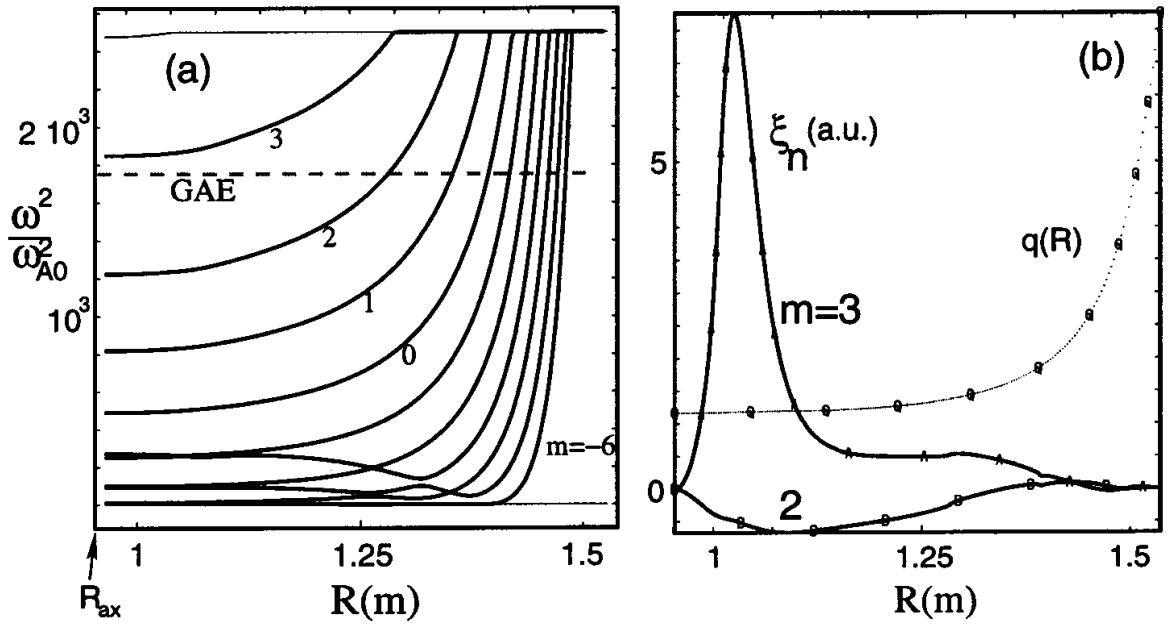

Figure 2.4: Taken from Ref. [18], (a) the Alfvén continuum for $n = -3$ in an NSTX plasma calculated by the NOVA simulation code, with GAE frequency shown by the dashed line; (b) the mode structure of the GAE for two dominant poloidal harmonics.

GAEs exist below a minimum of the Alfvén continuum [10, 13, 19], and form at a minimum in the q-profile that leads to an extremum in the continuum. GAEs are commonly observed on spherical tokamaks like NSTX(-U) [20, 21, 22, 23, 13]. The mode structure of a GAE is shown for an NSTX plasma, calculated through simulation, in Fig. 2.4, taken from Ref. [18]. Fig. 2.4(a) shows the $n = -3$ Alfvén continuum with the dashed line indicating the frequency of the GAE. Fig. 2.4(b) shows the mode structure of the GAE for two dominant poloidal harmonics, radially localized near the minimum in the continuum. Tokamak plasmas such as the ones studied in this dissertation typically feature flat q profiles, so GAEs are expected to be core-localized near the magnetic axis.

2.6. Fast-ion drive for anisotropic beam distribution

CAE/GAEs are driven unstable by Doppler-shifted cyclotron resonant fast-ions from NBI [24]. A main source of mode drive is anisotropy in the beam ion velocity distribution function [13, 18], with the energy source for the instability being provided by a "bump on tail" in the $v_\perp$ direction. The excitation of these modes requires large enough velocity space gradients to overcome damping from the background plasma through processes like phase mixing [25] and Landau damping [11].

Fast-ion drive and damping is derived by assuming a two-component homogeneous plasma consisting of the bulk plasma in the cold plasma limit and a hot kinetic fast-ion population. The full analytic derivation may be found in Ref. [11], and the derivation presented here follows that reference closely to produce a simplified equation for the growth rate.

In the previous section it was found that the general dispersion relation is given by

$$\begin{vmatrix} \varepsilon_{11} - n_\parallel^2 & \varepsilon_{12} \\ \varepsilon_{21} & \varepsilon_{22} - n^2 \end{vmatrix} = 0 \tag{2.15}$$

where it was assumed, without loss of generality, that the equilibrium magnetic field is $\boldsymbol{B_0} = B_0\hat{z}$ and the wave vector is $\boldsymbol{k} = k_\perp\hat{x} + k_\parallel\hat{z}$.

The bulk plasma components may be described using the cold plasma formulation:

$$\delta_{ij} + \varepsilon_{ij}^{th,e} + \varepsilon_{ij}^{th,i} = \begin{bmatrix} S & -iD \\ iD & S \end{bmatrix} \tag{2.25}$$

where S, D are defined as in Eq. 2.21, and the superscripts e, i refer to electrons and ions respectively.

S and D may be approximated by taking $\omega \ll \omega_{pe}, |\omega_{ce}|$, giving

$$\begin{aligned} S &\approx Ac^2/v_A^2 \\ D &\approx -\overline{\omega}Ac^2/v_A^2 \end{aligned} \tag{2.26}$$

where A and $\overline{\omega}$ are defined earlier as $A = 1/(1-\overline{\omega}^2)$ and $\overline{\omega} = \omega/\omega_{ci0}$.

Defining $K_{ij} = v_A^2 \varepsilon_{ij}^b / c^2$ and $y = \omega^2/(k^2 v_A^2) = N^{-2}$, where the superscript b denotes the beam component, the full dispersion is

$$(y - F^2 A^{-1} - y A^{-1} K_{11})(y - A^{-1} - y A^{-1} K_{22}) - y^2(\overline{\omega} + A^{-1} K_{12})^2 = 0 \tag{2.27}$$

This dispersion relation is solved perturbatively to first order in $K_{ij} \sim n_b/n_e \ll 1$ by letting $\omega = \omega_0 + \omega_1$ with $\omega_1 \ll \omega_0$:

$$\frac{\omega_1}{\omega_0} = \frac{y_0[K_{11}(y_0 - A_0^{-1}) - 2\overline{\omega_0} y_0 |K_{12}| + (y_0 - F^2 A_0^{-1}) K_{22}]}{2(y_0^2 - F^2)} \tag{2.28}$$

The full analytic solution for this is solved by calculating the tensor elements K_{ij}. The growth rate can be solved for as $\gamma_{\mathrm{EP}} = \mathrm{Im}(\omega_1)$, and the full derivation and expression for γ_{EP} may be found in Ref. [11]. For the purposes of this dissertation it is sufficient to simplify this as:

$$\gamma_{\mathrm{EP}} \propto - n_{\mathrm{EP}} \int h(\chi, v) \frac{\partial f_{\mathrm{EP}}(\chi, v)}{\partial \chi} d\chi \Big|_{v_{b\parallel} = v_{\parallel,\mathrm{res}}} \tag{2.29}$$

showing that CAE/GAE drive from fast-ions (γ_{EP}) is an integral over velocity space gradients from the fast-ion distribution, with one term dominating because anisotropy is large. Here, $\chi = v_\parallel / v$ is the fast-ion pitch, and $h(\chi, v)$ is a positive function including finite Larmor radius effects, $k_\perp$ dependencies, and other terms which weight velocity space. The integral is taken along a $v_{b\parallel} = v_{\parallel,\mathrm{res}}$ resonance contour where $v_{b\parallel}$ is the parallel velocity of the injecting beam. Eq. 5.7 is valid for sub-cyclotron modes driven by DCR. f_{EP} is the normalized fast-ion distribution ($\int f_{\mathrm{EP}}(\boldsymbol{v}) d^3\boldsymbol{v} = 1$) and the partial derivative $\partial f_{\mathrm{EP}}/\partial \chi$ is taken at constant energy. The value of n_{EP} determines the fast-ion number density. From Eq. 5.7 it can be seen that fast-ion drive occurs when $\partial f_{\mathrm{EP}}/\partial \chi < 0$, and that fast-ion damping occurs when $\partial f_{\mathrm{EP}}/\partial \chi > 0$.

2.7. Resonance condition

The tensor elements K_{ij} from the previous section can be calculated as [11]:

$$K_{ij} = \frac{n_b}{n_e}\frac{\omega_{ci}^2}{\omega}\int v_\perp dv_\perp dv_\parallel \sum_{\ell=-\infty}^{\infty} \frac{v_\perp^2 g_{ij}^\ell(\xi)}{\omega - k_\parallel v_\parallel - \ell\omega_{ci}}\hat{\pi} f_0 \tag{2.30}$$

with

$$\hat{\pi} = \frac{1}{v_\perp}\frac{\partial}{\partial v_\perp} + \frac{k_\parallel}{\omega}\left(\frac{\partial}{\partial v_\parallel} - \frac{v_\parallel}{v_\perp}\frac{\partial}{\partial v_\perp}\right) \tag{2.31}$$

and

$$g_{ij}^\ell(\xi) = \begin{pmatrix} \ell^2 J_\ell^2/\xi^2 & i\ell J_\ell' J_\ell/\xi \\ -i\ell J_\ell' J_\ell/\xi & (J_\ell')^2 \end{pmatrix}, \qquad \xi = k_\perp \rho_{\perp b} \tag{2.32}$$

where $\rho_{\perp b}$ is the Larmor radius for fast-ions, and $J_\ell(\xi)$ is the ℓ^{th} order Bessel function of the first kind.

The expression for the tensor element K_{ij} in Eq. 2.30 has a resonant denominator from which the DCR resonance equation is given [13]:

$$\ell\omega_{ci} \approx \omega - k_\parallel v_{b\parallel} \tag{2.33}$$

where $\ell = 0$ corresponds to direct resonance and $|\ell| = 1$ corresponds to cyclotron resonance, with $\ell = 1$ being ordinary cyclotron resonance and $\ell = -1$ being anomalous cyclotron resonance. The focus of this thesis will be on $\ell = 1$ DCR modes; Eq. 5.7 is valid for modes driven by the $\ell = 1$ resonance – those driven by $\ell = 0$ or $\ell = -1$ would have opposite leading signs and differing h functions.

Eq. 2.33 is a local resonance condition, and orbit averaging is necessary to satisfy the global resonance and describe a net resonance between the wave and particle, averaged over its orbit, while not being locally in resonance everywhere because of the spatial inhomogeneity of the plasma [11].

Taking into account this spatial inhomogeneity and particle orbits, the growth rate of AEs

is [26]:

$$\gamma \simeq -\frac{\omega}{2}\frac{\sum_j \mathrm{Im}\int E_1^* \hat{\varepsilon}_{j11}^A E_1 d^3r}{\int E_1^2 |\hat{\varepsilon}_{11}| d^3r} \tag{2.34}$$

where E_1 is the perturbed electric field in the direction of mode propagation and the integral is taken over the plasma volume that the mode exists in. From Ref. [12], part of the numerator in this equation can be written as:

$$\int E_1^* \hat{\varepsilon}_{11}^A E_1 d^3r = \frac{8\pi^2 e^2 B}{\omega_c \omega^2 T}\int dP_\varphi d\mu d\mathcal{E}\tau_b \sum_{\ell,p}\frac{F_{\ell p}'^*(\omega-\omega_*^T)F_{\ell p}}{\omega-\ell\langle\omega_c\rangle-\langle\omega_D\rangle-p\omega_b} f \tag{2.35}$$

where $\mathcal{E}$ is the particle energy, P_φ is the toroidal canonical momentum, μ is the adiabatic moment, τ_b is the bounce frequency, f is the equilibrium distribution function, and $F'_{\ell p}$ are functions that account for wave particle interactions. Here ω_D and ω_b are the drift and bounce frequencies respectively and the brackets $\langle\cdots\rangle$ refer to an orbit-averaged quantity. From this resonant denominator, the orbit-averaged resonance condition is [26]:

$$\omega - n\omega_\varphi + p\omega_\theta - \ell\langle\omega_{ci}\rangle = 0 \tag{2.36}$$

where ω_φ and ω_θ are the characteristic poloidal and toroidal orbit frequencies for passing particles as described in Section 1.2 (positive for passing ions moving in the beam direction), n is the toroidal mode number, $p = m + s$ where m is the poloidal mode number and s is the toroidicity-induced sideband number (or resonance order), and $\langle\omega_{ci}\rangle$ is the orbit-averaged beam ion cyclotron frequency. Here, ℓ refers to the different types of resonance as in Eq. 2.33. It is important to note that previous studies of beam-driven Alfvén eigenmodes have found that a small s is required for strong wave-particle interactions, and thus mode resonances are implausible for large s [27].

2.8. Damping sources

CAE/GAEs are subject to damping through interactions with the thermal bulk plasma. The dominant source of damping is likely continuum damping, which as described earlier

and in Ref. [25] is when the wave is damped strongly through phase mixing as it has different phase velocities at different radii. For CAEs this is apparent because simulations have commonly shown mode conversion near the location of the Alfvén resonance [28, 29]. Many studies have shown that GAEs are also expected to primarily experience continuum damping [30, 25].

In practice Alfvén waves are also expected to be damped by thermal bulk electrons through Landau damping and transit-time damping [18, 31]. These processes have been heavily reviewed in textbooks like Ref. [32] and [1]. Landau damping occurs when there is a gradient in the particle velocity distribution function at the location of the resonance: energy is exchanged between the wave and particles in the bulk plasma that have velocities comparable to the phase velocity v_{ph} of the wave and therefore interact strongly with it. Particles with velocities slightly less than v_{ph} are accelerated while particles with velocities greater than v_{ph} are decelerated. Landau damping occurs when a gradient in the distribution function exists such that there are more particles gaining energy from the wave. Transit-time damping occurs when transiting particles exchange energy with the wave; the net exchange in energy results in wave damping [33]. Both of these damping processes involve particles that move along the magnetic field with the phase velocity of the wave [34].

For the work presented in this dissertation, a comprehensive identification of CAE/GAE damping was not conducted and would require calculations of kinetic effects of the bulk plasma in addition to the fast-ions; this constitutes future work.

Generally the background damping rate depends only plasma parameters and not on properties of the fast-ions. In Ref. [34], the electron damping rate in a slab is derived for compressional modes. This calculation is generalized to shear waves in Ref. [14]; in this approximation, both CAEs and GAEs will have electron damping scaling as

$$\gamma_{\mathrm{damp}} \sim \beta_e y e^{-y^2} \tag{2.37}$$

where γ_{damp} is the damping rate, $\beta_e = \frac{P_e}{B^2/2\mu_0}$ is the electron beta where P_e is the electron pressure and B is the magnetic field, and $y = \omega/k_{\parallel} v_{\mathrm{th,e}}$. Thermal ions in the population

are not considered because they are unlikely to have sufficient energy to resonate with and damp the waves.

CHAPTER 3

The DIII-D tokamak

3.1. Overview of DIII-D

The DIII-D tokamak is a fusion research experiment operated by General Atomics in San Diego, CA [35, 36]. The results presented in this dissertation are from L-mode (low confinement) beam-heated plasmas. Typical operating parameters for L-mode plasmas are listed in Table 3.1, and a cutaway view of the DIII-D tokamak is shown in Fig. 3.1 [37].

Symbol	Parameter	Value
B_t	Toroidal magnetic field	2 T
I_p	Plasma current	1 MA
R_0	Major radius	1.67 m
a	Minor radius	0.67 m
τ_{pulse}	Plasma duration	$5-6$ s
$\langle n_e \rangle$	Line averaged electron density	$1-3\times10^{13}$ cm^{-3}
$T_e(0)$	Electron temperature at magnetic axis	$2-4$ keV
D	Main ion species	Deuterium
β	Plasma beta	< 0.5

Table 3.1: Typical operating parameters for L-mode plasmas in DIII-D.

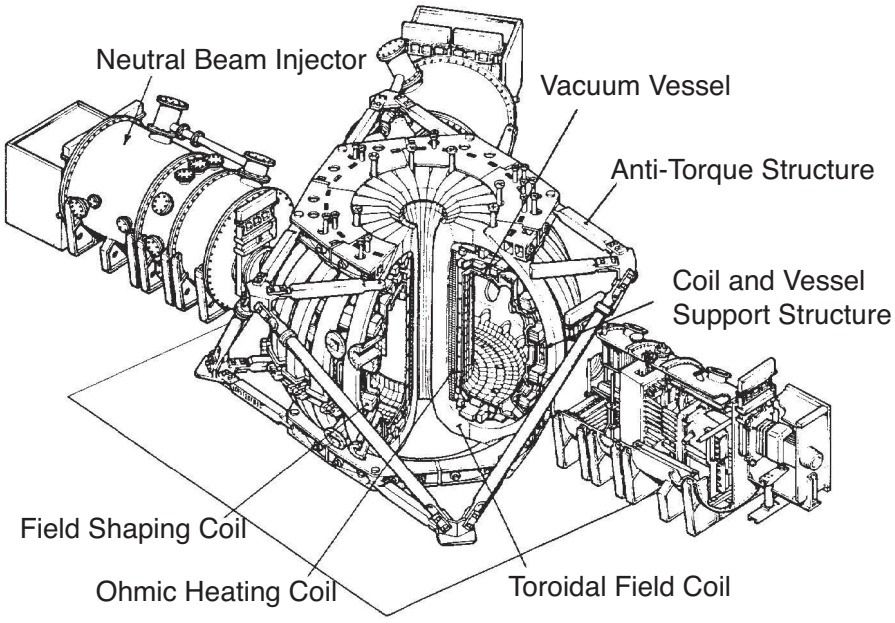

Figure 3.1: Cutaway view of DIII-D showing three of the four neutral beam injectors [37].

3.2. Neutral beam injection

The largest heating system on the DIII-D tokamak is the neutral beams [37]. There are four neutral beam injectors in total, and each injector contains two sources that inject at different angles, with the capability of cumulatively providing up to 20 MW of heating power to the plasma via < 80 keV deuterium ions [38]. The beamlines can also operate with hydrogen and helium, but the results discussed in this thesis are from deuterium plasmas only. Fig. 3.3 shows the four neutral beam injectors, with eight separate beamlines that inject onto the midplane. The beams inject ions with energies (beam voltages) in the range of $40 \leq V_{\mathrm{b}} \leq 85$ kV and currents in the range of $40 \leq I_{\mathrm{b}} \leq 65$ A. Each beam can be turned on for a minimum of 5 ms with a minimum spacing of 10 ms between beam pulses, allowing for modulation of beams to control the injected energy and torque [39]. Additionally, the beams also serve as diagnostic beam sources for the charge exchange recombination (CER) diagnostic [40], used for ion temperature profiles and plasma rotation measurements, and the motional Stark effect (MSE) diagnostic [41, 42], used for measurements of the plasma q profile.

Neutral beam production consists of several stages [1]. In DIII-D, a filament-based plasma source first produces ions that are accelerated to the required energy [38]. This results in an ion beam that is passed through a large gas chamber in order to be neutralized – this is necessary because a neutral beam is required in order to cross the magnetic field of the tokamak and penetrate the plasma. Finally, the resulting neutral stream of particles is collimated as it enters the tokamak. The final apertures of the neutral beams entering the tokamak are 12 cm wide by 48 cm tall [38]; when the neutral beams actually enter the plasma they have an approximately Gaussian distribution and have a full-width at half-maximum at a horizontal width of 10 cm and vertical height of 26 cm [43].

This process is illustrated in Fig. 3.2, which is taken from the DIII-D internal website. The high voltage feedthrough brings in over 80,000 Volts DC into the ion source enclosure. This ion beam is aligned and enters the neutralizer which consists of a deuterium gas target. This yields a neutral beam, and any remaining charged particles are turned by the reflecting magnet into the ion dumps which consist of a set of thick copper plates with water cooling channels. Finally, the beam path is collimated through the gas baffle and other magnetic collimators before entering the vessel. The cryopanels inside the beamline help to maintain vacuum pumping for the deuterium used for the ion source and neutralizer and consist of a liquid Helium surface shielded by a liquid Nitrogen panel.

A deuterium ion source will produce both the atomic ion D^+ and the molecular ions D_2^+ and D_3^+. All three of these species will pass through the accelerator and acquire the same energy, but the molecular ions D_2^+ and D_3^+ will have lower velocity due to their higher mass. These particles dissociate in the neutralizer and the resulting beam will have atoms that are at full energy, one-half energy, and one-third energy. In DIII-D, for 80 keV deuterium, the injected beam is typically 76% full, 16% half, and 7% third energy [37].

Beam current and voltage are measured at the source, before the neutralization and collimation processes. During these processes, while voltage remains the same, current is lost due to neutralization efficiency and transmission efficiency (determined from the ion dump and calorimeter shown in Fig. 3.2). Because of this, for the analysis presented here, the beam injection rate is considered in place of the beam current. The injection rate is

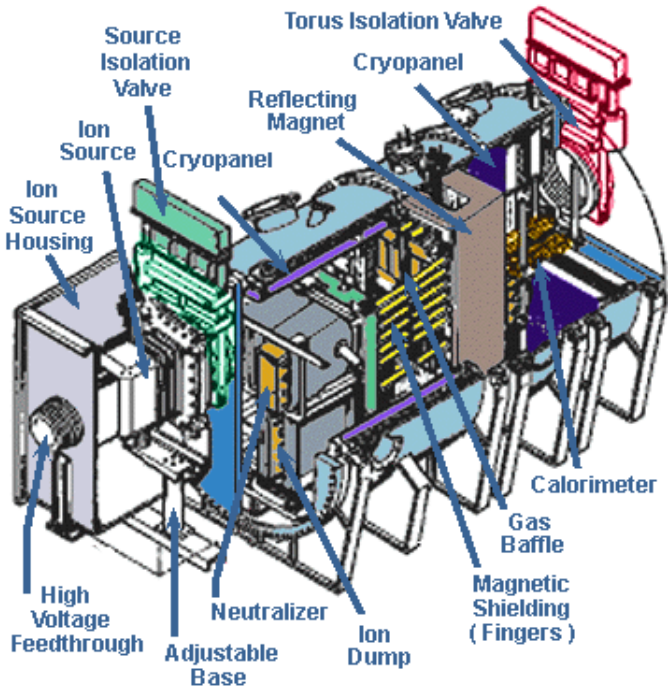

Figure 3.2: The anatomy of a DIII-D beamline, taken from the DIII-D internal website.

calculated as beam power divided by voltage in keV, and is expressed for convenience in Amps.

3.2.1. Beam geometry

The DIII-D beamlines are located at toroidal angles of 30°, 150°, 210°, and 330° at the midplane, as shown in Fig. 3.3. Each beam is named according to its toroidal location and orientation within the beam housing (e.g., 30L, 30R) [38]. An example of the separate injection geometries (tangential, perpendicular) within a neutral beam injector is shown in Fig. 3.3 for the 150L and 150R beams. The two tangential and perpendicular sources inject at angles of 47° and 63° tangent to the magnetic axis, with tangency radii (R_{TAN}) of 1.14 and 0.74 m respectively [37].

The 30°, 150°, and 330° beamlines inject in the co-current direction, where the plasma current I_p is counter-clockwise viewed from above and the toroidal magnetic field B_t is clockwise for the results discussed in this thesis. The 210° beamline injects in the counter-current direction, and is important for driving rotation and heating plasmas [38,

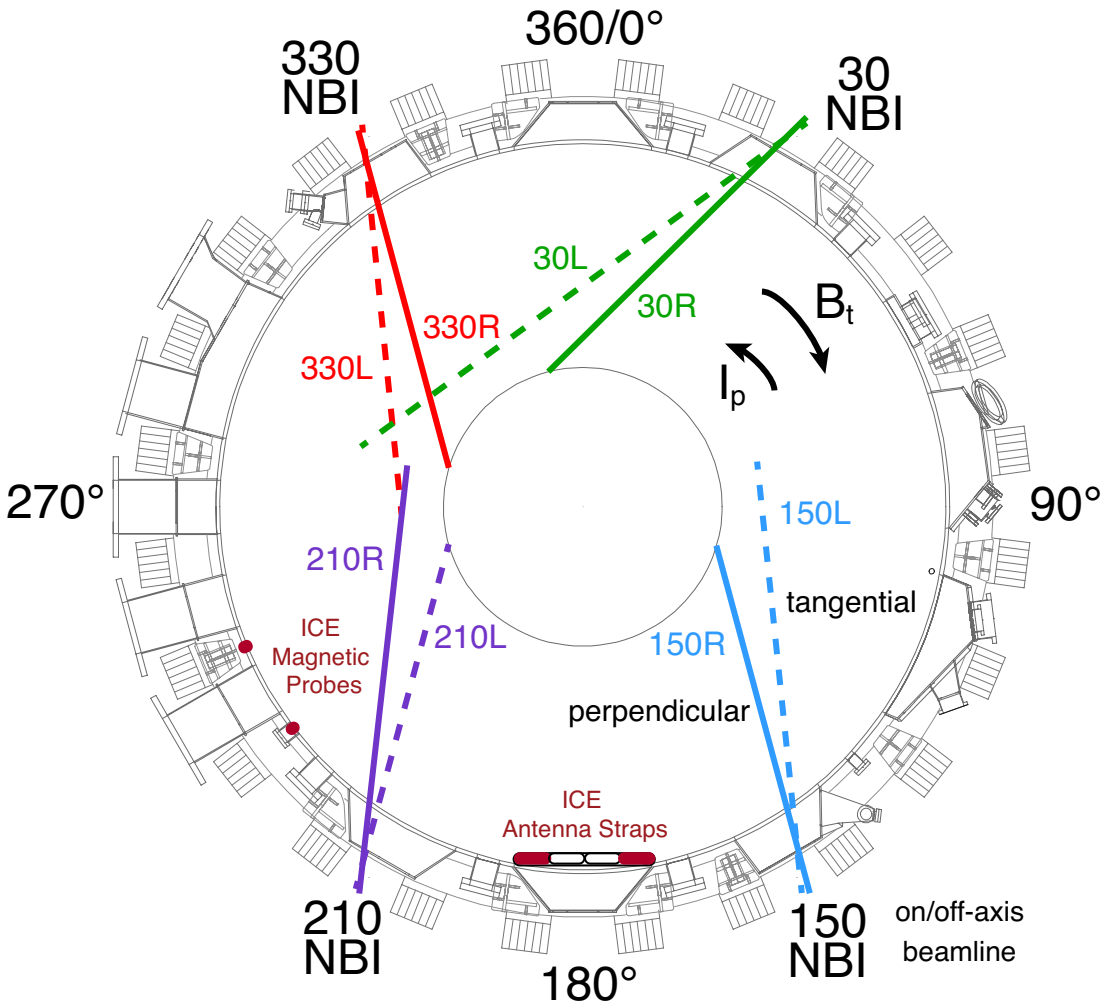

Figure 3.3: Top view of DIII-D showing the neutral beam system. An example beam injection geometry is labeled for the beam at 150 for the tangential and perpendicular beamlines. The two ICE systems are also shown at their approximate location on the machine [44].

45].

The 150° beamline, consisting of the 150L and 150R beams, can be tilted downward [46, 47] by up to 16.4°, allowing for off-axis heating and current drive. For the toroidal field direction (clockwise), tilting the beam results in more perpendicular injection, allowing exploration of a wider parameter space. For the results presented in this thesis, the 150R beam was fully tilted at 16.4° to inject off-axis.

3.2.2. Variable beam perveance

A feature of the DIII-D beams is the capability of variable beam perveance (VBP) [38], which allows the voltage (energy) and current (injection rate) of the beams to be independently varied within certain limits while maintaining acceptable beam divergence. As mentioned earlier, historically the pulse widths of the beams can be modulated to control the total time-averaged injected power; this is the typical approach for machines like DIII-D, NSTX-U, and others [48]. Other forms of in-shot beam power variation have been implemented on other machines; on the Mega Ampere Spherical Tokamak (MAST), the beam source current was controlled in real time to allow variations in neutral beam power [49], and on the Tokamak Experiment for Technology Oriented Research (TEXTOR), the vertical aperture of the neutral beam injector was varied in-shot to achieve NBI power variation [50]. However, VBP on the DIII-D beams has been used in a unique way by allowing for the first simultaneous in-shot variation of beam voltage (energy) and current (injection rate/density) [48] to investigate the stability of a fast-ion driven mode.

The perveance Π of a beam is a parameter that accounts for the requirement for neutral beams to maintain acceptable beam divergence while undergoing changes to beam power, current, and voltage. Perveance is related to the current I_b and voltage V_b as $\Pi = I_\mathrm{b}/V_\mathrm{b}^{3/2}$, and the technical challenges and considerations of the development of VBP are discussed in Refs. [39, 51].

As mentioned earlier, neutral beam production involves the extraction of an ion beam that

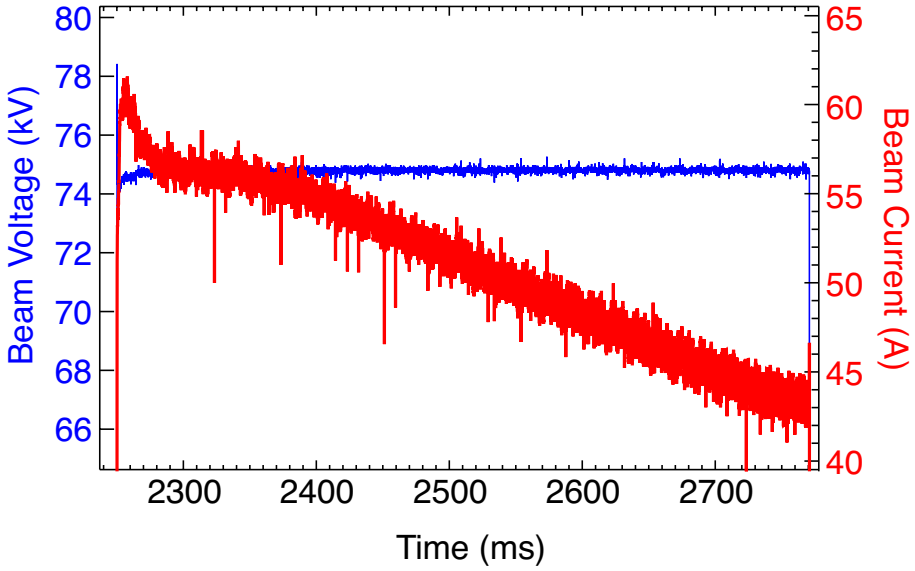

Figure 3.4: The voltage of the 150R beam is held constant while the beam current is ramped down by approximately 40%, taken from discharge #172026.

is passed through a large gas chamber for neutralization. The space charge of the un-neutralized ions can affect the path and direction of the eventual produced neutral beam: electrostatic fields arising from the space charge can deflect particles from the desired path [38]. Perveance is a parameter that indicates the amount to which space charge affects the deflection, and therefore divergence, of the neutral beam. In DIII-D, for each neutral beam there is typically an ideal value of perveance for which the accelerated ions are deflected minimally. Variable beam perveance allows for NBI to operate away from this optimum value. The NBI system has a built-in machine protection circuit measuring stray ion impacts that will shut off the beam if the perveance reaches a value that deviates too much from the optimum value; the allowable perveance range is estimated through experience to be approximately 15% from optimum [38].

Because an acceptable beam divergence must be maintained, any variation of beam current or voltage is limited by their relationship through perveance $\Pi = I_b/V_b^{3/2}$. A typical operating mode uses the Plasma Control System (PCS) to automatically adjust the

beam current to maintain optimum perveance with a pre-programmed voltage [38, 52]. For the results presented in this thesis, however, during VBP both the beam voltage and current are pre-programmed: the neutral beam power is controlled by holding either voltage or current constant, and varying the other parameter while staying within the allowable perveance range. The maximum voltage slew rate was 40 kV/s with a variation of $\Delta V = 20$ kV in a single shot across a range of beam current changes [38]. An example of one of these VBP ramps is shown in Fig. 3.4, where the current of the 150R (off-axis) beam is ramped down by approximately 40% while the voltage is held constant.

3.3. Diagnostics on DIII-D

DIII-D features a wide variety of diagnostics that contribute to experimental measurements. The following section consists of a brief overview of the main diagnostics that were used during the experiment, but is by no means a comprehensive summary of all available diagnostics. Some of the more prominent and/or relevant tokamak diagnostics and their measurements on DIII-D are listed in the table below.

Name of Diagnostic	Measurement
Motional Stark Effect (MSE)	Pitch angle of magnetic field
Charge exchange recombination (CER)	T_i, impurity density, rotation speed
Electron cyclotron emission (ECE)	$T_e(r,t)$
Thomson scattering	$T_e(r,t)$, $n_e(r,t)$
Multi-channel CO_2 interferometer	Line-averaged density fluctuations
Beam emission spectroscopy (BES)	Localized long-wavelength density fluctuations
Phase contrast imaging (PCI)	Multiscale electron density fluctuations
Fast-ion loss detector (FILD)	Pitch angle and gyroradii of lost fast-ions
Fast-ion deuterium-alpha (FIDA)	Diagnosing fast-ion population

3.3.1. Motional Stark effect (MSE)

The motional Stark effect (MSE) diagnostic is primarily used to measure the pitch angle profile of the magnetic field, providing valuable information about the tokamak safety factor q as well as the profile of the radial electric field E_r. MSE data is also extremely vital in providing accurate equilibrium reconstruction estimates. In DIII-D, MSE utilizes the Balmer alpha line emitted from high-energy neutrals that are injected into the plasma [42]. As the neutrals travel across the magnetic field in the plasma, they are subject to a strong Lorentz electric field $\boldsymbol{E} \propto \boldsymbol{v} \times \boldsymbol{B}$. This causes the alpha emission to undergo Stark splitting, with 9 distinct lines and two polarization states (parallel and perpendicular to the electric field). Given the initial velocity of beam injection, measuring the polarization angle of the emission gives the pitch angle of the magnetic field.

Figure. 3.5 shows the MSE diagnostic on DIII-D. The original MSE diagnostic was an 8-channel system (shown in the figure as "Central MSE"), designed for radial resolution in the core. The multichord MSE system was improved later to include an additional 8 chords (shown in the figure as "edge MSE") to expand radial resolution to the outer 30 cm of the plasma. The current MSE system provides reliable measurements for beam energies of > 65 keV and toroidal magnetic fields of > 0.8 T [42].

3.3.2. Charge exchange recombination (CER)

The charge exchange recombination (CER) spectroscopy systems on DIII-D are used to measure ion temperature, impurity density, and rotation speed profiles [40]. Charge exchange recombination refers to the process by which spectral lines are excited through charge exchange between ions in the plasma and energetic particles from NBI. The reaction associated with this process is:

$$D^0 + A^{Z+} \longrightarrow D^+ + A^{(Z-1)+*} \longrightarrow D^+ + A^{(Z-1)+} + \gamma \tag{3.1}$$

where D is the injected deuterium atom from NBI, A is an ion in the bulk plasma, and γ is the excited spectral line.

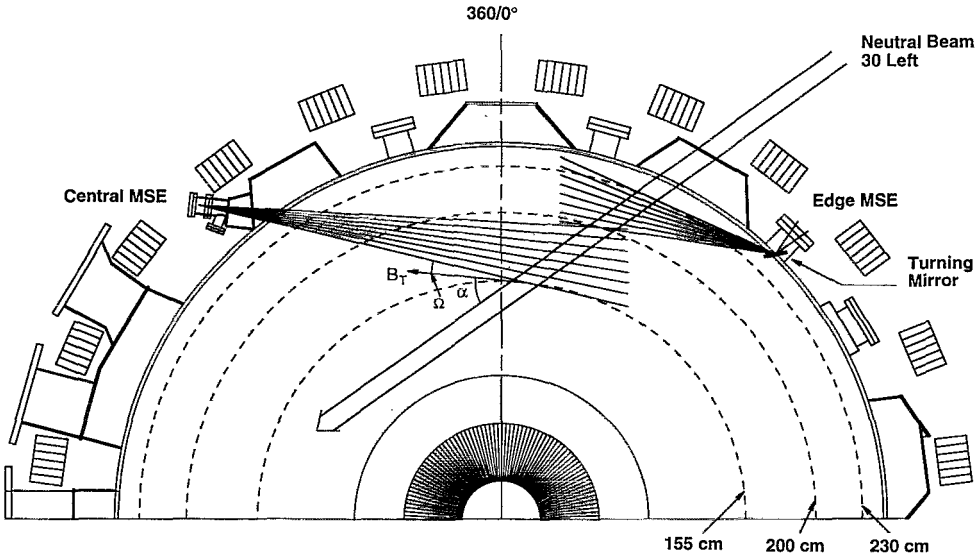

Figure 3.5: Taken from Ref. [42]. This schematic shows the geometry of the 16-chord MSE diagnostic on DIII-D.

Spectroscopically measuring the emitted spectral line gives valuable information about the plasma: determining the Doppler shift allows the calculation of bulk plasma motion, and measuring the Doppler broadening of the line gives the ion temperature of the plasma. The intensity of the line, indicated in Eq. 3.1 by γ, is determined solely by the charge exchange that takes place.

Fig. 3.6 shows the plan and cross section views of the CER spectroscopy system. The system consists of 80 spatial views, with 48 tangential and 32 vertical, that intersect the neutral beams at the midplane. The measurement from each cord is spatially localized at the intersection of the viewchord and the neutral beam. In order for CER to function, one of the beams at either the 30° or 330° tangential position needs to be on (30L/R or 330L/R). These beams are typically modulated in order to eliminate signal interference and provide good localization of the measurement.

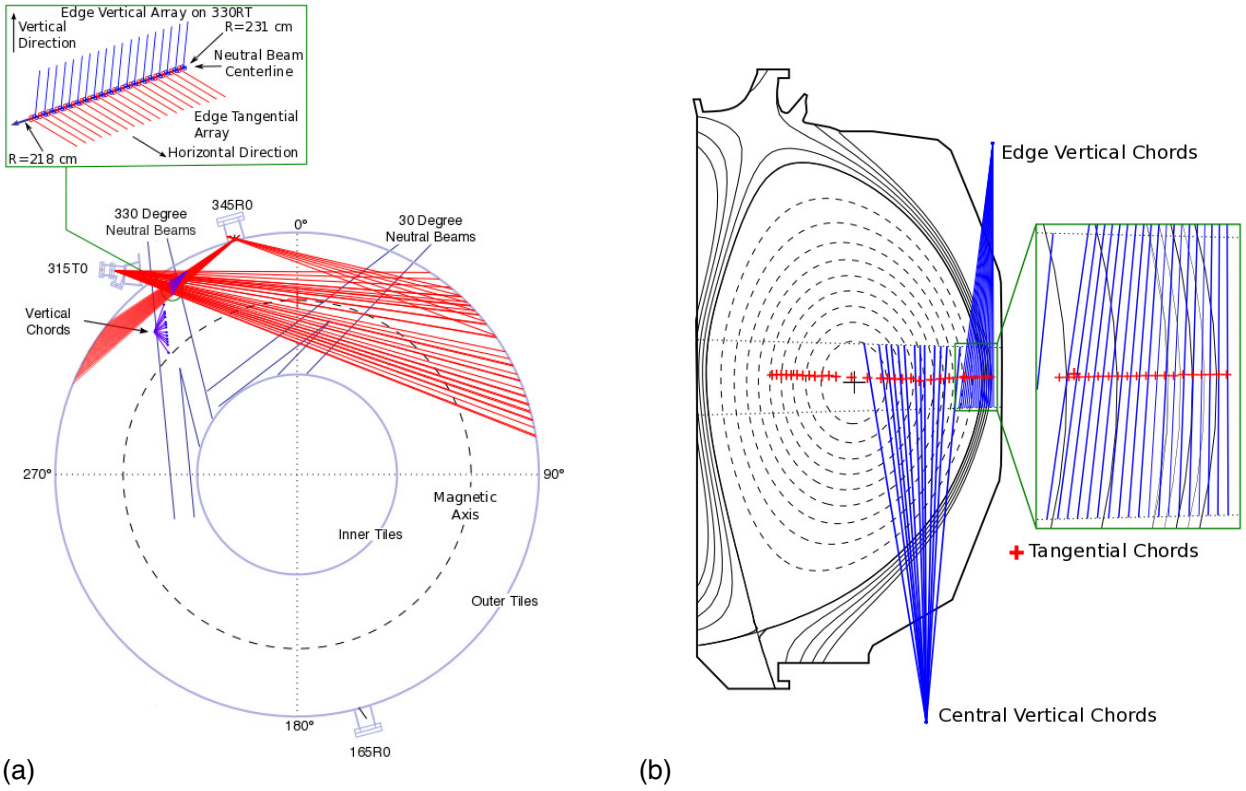

Figure 3.6: (a) The plan view and (b) the cross section view of the CER system, showing where the chords are in the DIII-D vessel.

3.3.3. Electron cyclotron emission (ECE)

The electron cyclotron emission (ECE) diagnostic measures the electromagnetic radiation emitted by the gyration of electrons around the field lines of a magnetically confined plasma [1] and correlates the intensity of this emission to T_e. The diagnostic is able to obtain spatial resolution of $T_e(r,t)$ through the spatial dependence of the magnetic field.

The ECE heterodyne radiometer on DIII-D has 40 channels, upgraded in 2003 from its original 32 [6]. This upgrade allowed for T_e measurements into the magnetic axis at maximum field (2.15 T), as well as improving on central T_e measurements in low-field discharges. An example of the electron temperature profile measured from ECE is shown in Fig. 3.7.

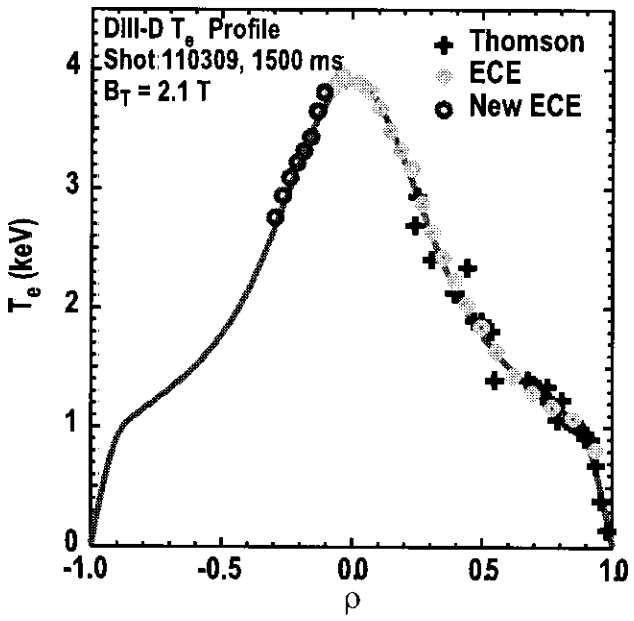

Figure 3.7: Electron temperature (T_e) profile as a function of normalized effective plasma radius ρ for a DIII-D discharge measured from the ECE radiometer [6].

3.3.4. Thomson scattering

The Thomson scattering system is a spectral diagnostic and is used to measure electron temperature and density. A laser is shot into the plasma, and T_e is determined from the

degree of broadening of the spectrum of the scattered radiation [1]. From electromagnetic theory it follows that the power scattered per unit solid angle per unit frequency is:

$$P_s(\omega) = P_0 r_e^2 \sin^2 \psi n_e L S(k, \omega) \tag{3.2}$$

where P_0 is the total incident laser power, r_e is the electron radius, ψ is the angle between the electric field vector of the incident ray and the scattered ray, L is the interaction length, and $S(k, \omega)$ is the spectral density function [1]. $S(k, \omega)$ is dependent on the electron velocity distribution.

The intensity of the spectrum of scattered light is proportional to plasma density, while the spectral width and blue-shift give the electron temperature of the plasma.

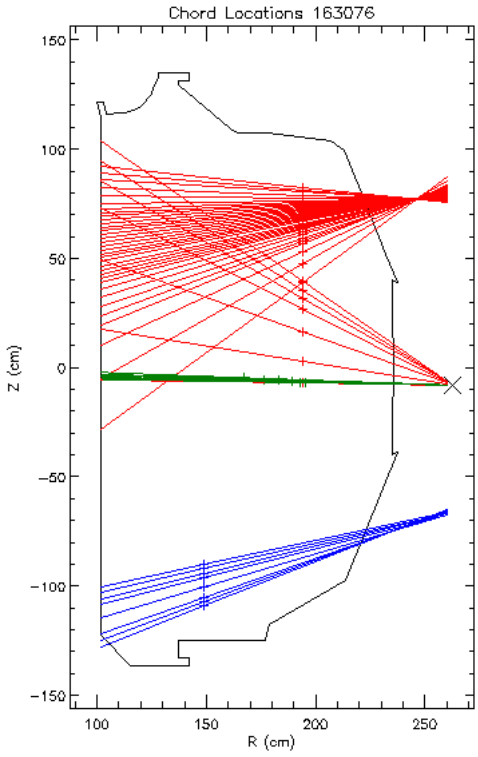

Figure 3.8: Viewing chords of the DIII-D Thomson scattering system. The red lines indicate the chords on the core laser path; the blue indicate chords on the divertor path; and the green indicate the horizontal/tangential chords.

The DIII-D Thomson scattering system uses neodymium-doped yttrium aluminum garnet lasers which have three entry points to the plasma, shown in Fig. 3.8: the core laser path,

the divertor path, and the horizontal/tangential path. Combined, these give data from up to 70 simultaneous spatial points through viewing chords, providing the electron temperature and density profiles.

3.3.5. Multi-channel CO_2 interferometer

DIII-D uses a heterodyne CO_2 interferometer to measure the electron density of the plasma [53]. Theoretically, the phase change of a coherent beam passing through a plasma is proportional to the electron density integrating along the beam path [1]:

$$\Delta\phi = \frac{\lambda e^2}{4\pi\epsilon_0 m_e c^2} \int n_e \mathrm{d}l \tag{3.3}$$

where λ is the wavelength of the beam.

Typical interferometers on tokamaks use a two-color system in order to separate mechanical vibrations in the measurement; essentially, a two-color system means that there are two interferometers that operate at different wavelengths along the same optical path. This is true of the interferometer on DIII-D, shown in Fig. 3.9, which utilizes a 10.6 μm CO_2 laser in order to reduce the effects of refraction of the beams by transverse density gradients, which can be large on non-circular tokamak plasmas like those in DIII-D [54]. The small wavelength ensures that any phase shifts from refraction due to density gradients is minimized. The CO_2 laser is combined with a 0.63 μm He-Ne laser in the implementation of the two-color system. There are four interferometer chords in total, as shown in the figure: three vertical and one radial. Each chord yields a line-integrated electron density along the chord. The CO_2 interferometer can also be used as a forward scattering diagnostic for low-k density fluctuations by measuring line-integrated density perturbations.

3.3.6. Fast-ion loss detector (FILD)

The fast-ion loss detector (FILD) is located on the outer wall of DIII-D and provides measurements of the pitch angles and gyroradii of energetic ions that reach its position

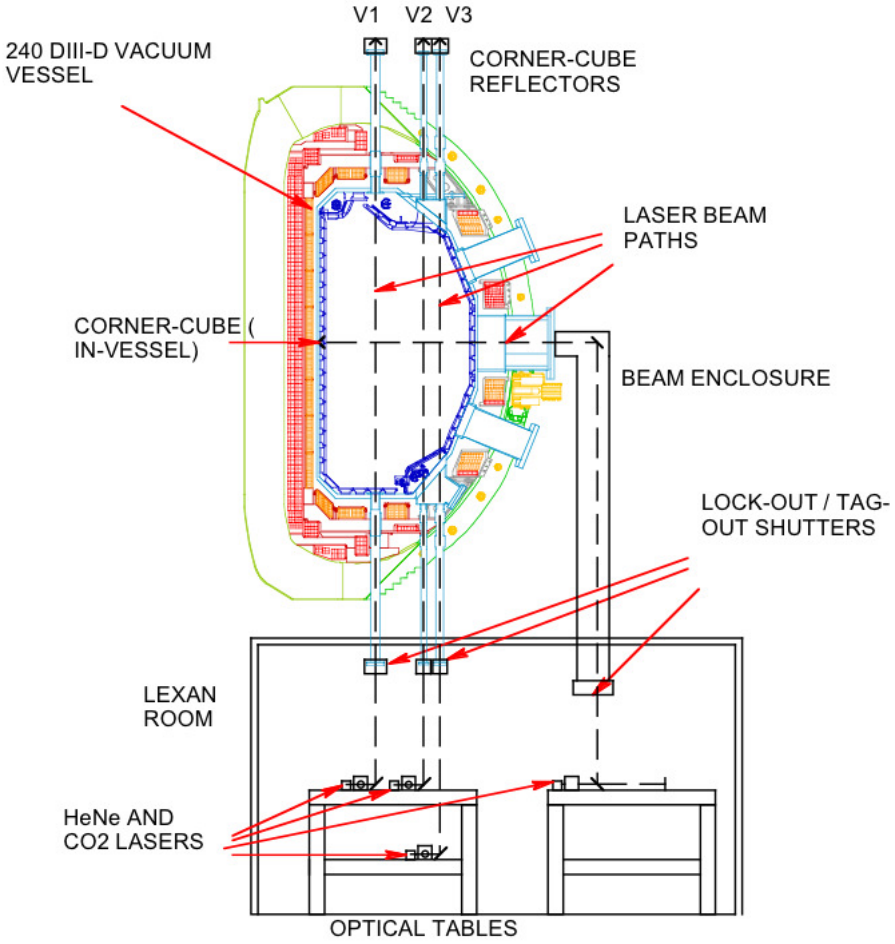

Figure 3.9: The two-color interferometer layout on DIII-D [54].

[55]. Currently, there are two operating FILDs, located at the 225° and 165° toroidal positions.

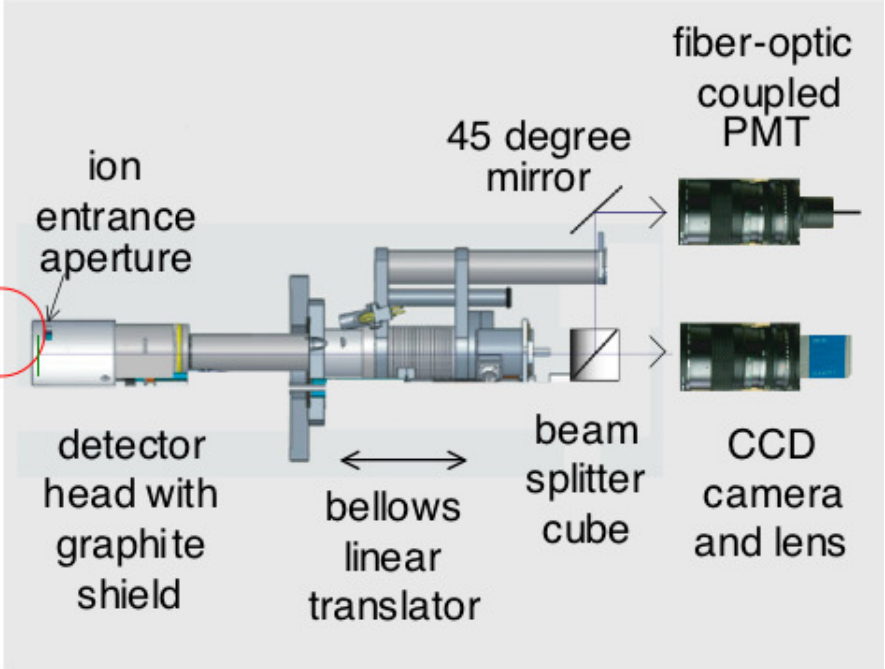

Figure 3.10: A schematic of the FILD diagnostic [55].

The FILD diagnostic includes a scintillator-based particle detector system. The schematic for the FILD is shown in Fig, 3.10. It is installed just below the outer midplane of DIII-D and can be inserted past the first wall; because of this capability, the scintillator is protected by a graphite heat shield with a narrow slit cut into it as seen in the figure. The red circle in the figure is drawn to visualize a fast-ion orbit that might reach the scintillator. The bellows linear translator allows the radial position of the FILD to be adjusted manually. The light from the scintillator is then split through a beam splitter cube into two paths: one goes to a CCD camera providing images of the scintillator surface, while the other enters a photomultiplier tube and provides a two-dimensional light pattern that yields information on the gyroradii and pitch angle of escaped fast-ions.

3.3.7. Fast-ion deuterium-alpha detector (FIDA)

The fast-ion deuterium-alpha (D_α) (FIDA) diagnostic is used, essentially, to diagnose one component of the fast-ion velocity [56]. The measured signal is a combination of fast-ion pitches ($v_\parallel/v$) and total energies in a portion of velocity space. Currently, there are two FIDA systems on DIII-D that work towards diagnosing the fast-ion population; these are shown in Fig. 3.11.

FIDA functions by utilizing the charge exchange between the injected atoms from NBI and the energetic ions in the bulk plasma. After charge exchange occurs, a portion of the neutralized fast deuterons are in the $n = 3$ atomic orbital state; these particles emit photons during the $n = 3 \rightarrow n = 2$ transition. Since these fast deuterons are travelling at velocities much higher than the thermal speed of the plasma, the emitted photon undergoes a Doppler shift. The resulting emitted spectral line is thus modified with a broad low-intensity feature that consists of blue- and red-shifted wings about the D_α line [57].

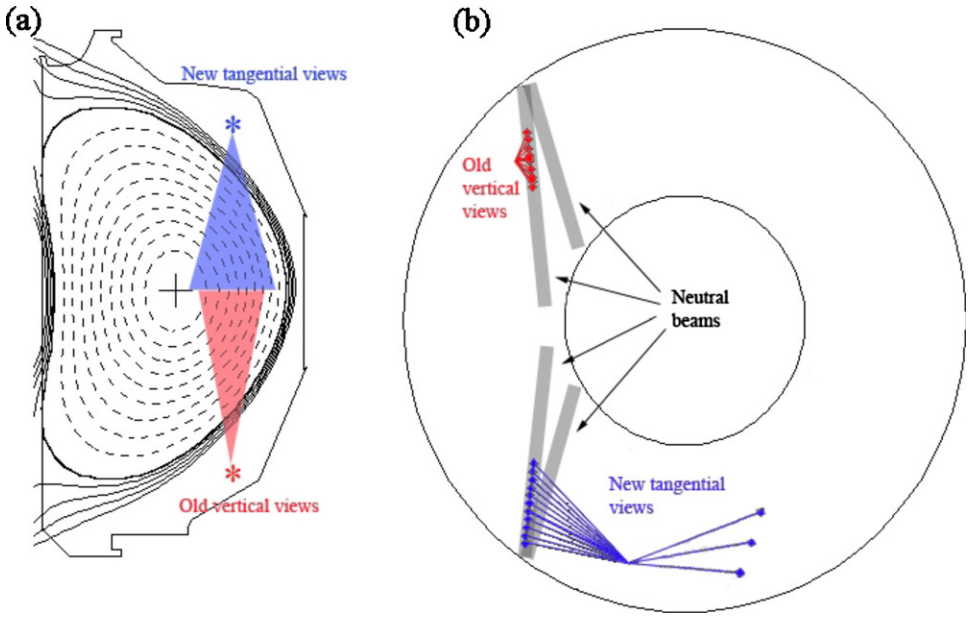

Figure 3.11: (a) Cross-section and (b) plan view of DIII-D showing poloidal projection of the 2 FIDA systems and their viewing chords, taken from Ref. [57].

The emitted photons are collected using an array of viewing chords. The locations of these

chords are shown in Fig. 3.11. The old FIDA system utilizes one of DIII-D's co-injecting beams, while the new system utilizes a counter-injecting beam. The different sightline geometries combined with the neutral sources are used in analyzing the signal by providing different weightings in fast-ion velocity space. FIDA uses beam modulation to optimize its measurement acquisition.

3.4. Magnetic fluctuation measurements via ICE coils

The Ion Cyclotron Emission (ICE) fast magnetic fluctuation diagnostic was utilized for magnetic fluctuation measurements [44], and consists of two sets of magnetic sensors located at the plasma edge in the outboard midplane (i.e. at the vertical midplane of the plasma, on the high major radius side). The ICE diagnostic measures emission in the Ion Cyclotron Range of Frequencies (ICRFs) excited by energetic ions from the neutral beams, and is capable of analyzing signals between $1 - 100$ MHz. ICE features high bandwidth, high speed acquisition (up to 200 MHz, 8 GB/shot), and has digitizers that allow exploitation of the full bandwidth of other fluctuation diagnostics (e.g. the CO_2 interferometer [54]).

The systems that constitute the ICE diagnostic are shown in Fig. 3.12. System 1 (Fig. 3.12)(a) consists of two antenna straps located approximately at the toroidal angle of 180°, toroidally separated by 13.3°. System 2, restored in 2017, consists of a set of magnetic field sensing loops incorporated into the carbon tiles located toroidally at 231.7° and 249.3° with a toroidal separation of 17.6°, shown in Fig. 3.12(b). ICE also includes a poloidally separated toroidal coil [58] that is used for bandpass measurements [59]. The results discussed in this dissertation consist of data acquired from ICE System 2. The locations of the two ICE systems can be seen in a top view of DIII-D in Fig. 3.3.

The electronic components of the ICE diagnostic are shown in a block diagram in Fig. 3.13 from Ref. [44], and described thusly:

> The outputs of the antenna straps (System 1) connect to a plastic enclosure via a RG58 cable. Within the vacuum vessel, the antenna probes (System 2)

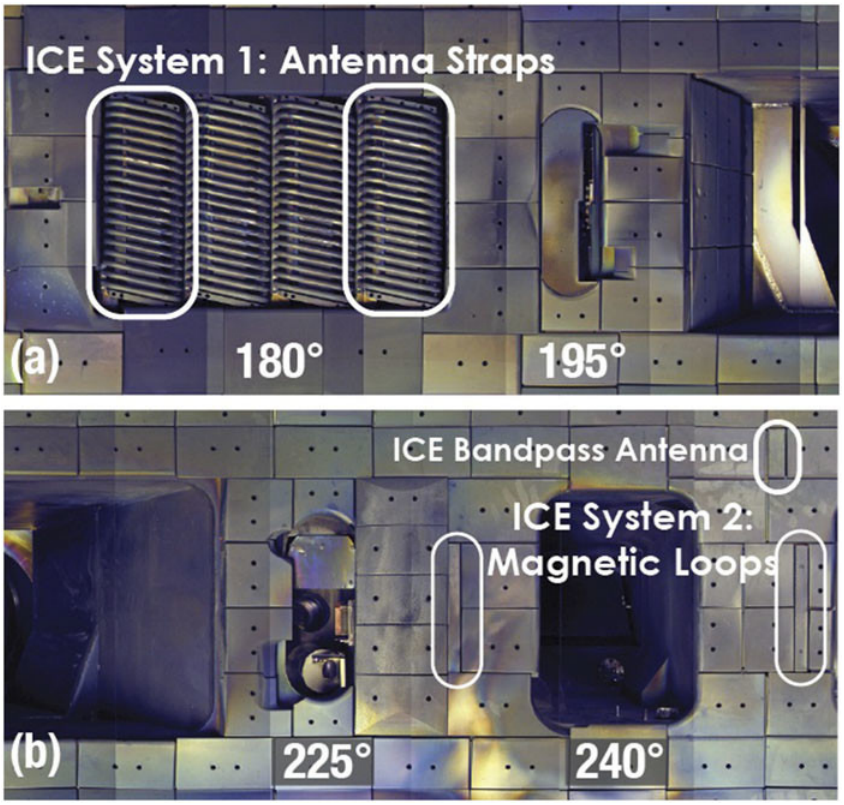

Figure 3.12: The ICE diagnostic consisting of (a) a set of antenna straps at 180°, (b) a set of tile antennae at 240°, and a tile probe used for bandpass measurements [44].

connect to a SubMiniature version A (SMA) feedthrough via a semi-rigid bakeable vacuum-compatible coaxial cable with a characteristic impedance of about 30 Ω. On the air side of the feedthrough, the SMA connectors are connected in parallel to a 75 Ω impedance-matching resistor and 50 Ω semi-rigid cables. Another semi-rigid coaxial cable transmits the signal to a BNC breakout panel within the plastic box. Inside this box, both ICE systems then connect to safety breaks, designed to provide 5 kV DC isolation for both inner and outer conductors. All three systems use slightly different DC break designs, but all originate from the RF program. The signal is transmitted to the electronic annex via RG213 (System 1) or RG214 (System 2) cables that have an electrical length of at least 75 m. In the annex, the cables terminate on a BNC breakout panel. Within the DIII-D annex, RG58 cables are used.

First, the signals are amplified by 5×(14 dB) with a 350 MHz SR445A preamplifier, and then, they are digitized using a 200 MHz GaGe CSE1642 digitizer. Typically, the signals are anti-aliased using a Mini-Circuits BLP-100+ low-pass filter before the amplifier, providing data below the 100 MHz Nyquist frequency. [$\cdots$] The frequency response of these systems is limited by the DC breaks. These breaks have an approximately flat electrical response from 1 MHz to ∼120 MHz, with a 3 dB point at ∼150 MHz. [$\cdots$] As this magnetic diagnostic is unshielded in the machine hall, it is also susceptible to electrical noise and pickup.

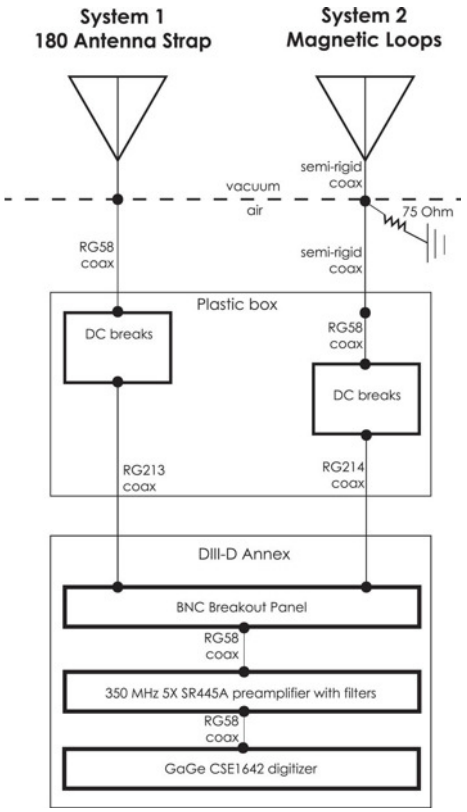

Figure 3.13: Electronic components of the ICE diagnostic [44].

The effects of the DC breaks on the results discussed in this dissertation are negligible as the frequency range of interest is sub-cyclotron (< 10 MHz).

3.4.1. Data analysis

ICE data is stored in MDSplus in 80 ms segments, for up to 5 s of data per shot, and recorded in Volts. An example of one 80 ms segment of the raw signal obtained from one of the loops of ICE System 2 is shown in Fig. 3.14, where magnetic fluctuations are correlated with neutral beam injection. Spectral analysis is performed by calculating $\delta b(t)$ through numerical integration of the measured $d(\delta b)/dt$ at each loop. $\delta b(t)$ is divided into time records with a 50% overlap, and each record undergoes Fast Fourier Transform (FFT) analysis after conditioning with a Hanning window to reduce the effects of artificial discontinuities and spectral leakage in the FFT. This results in a set of complex values $\delta b(t, f)$ at each loop, and the power of the magnetic fluctuation measured from ICE is $|\delta b|^2$.

When a single toroidal mode number is dominant at the measured mode frequency, a two-point toroidal mode number n can be obtained using the toroidally separated magnetic field sensing loops that constitute ICE System 2. The resolution of this toroidal mode number is limited by the toroidal separation of the loops as $|n| \leq 180/\Delta\phi \lesssim 10$. Toroidal mode numbers with $|n| > 10$ are not resolvable, and any mode number measurement obtained has a possibility of being aliased by integer multiples of ~ 20.

Unfortunately, there is an unknown and non-negligible path length difference between the two signals obtained from ICE System 2 (the set of tile antennae at $\sim 240°$). The signal path is from each of the loops to the digitizer located in the DIII-D annex noted in Fig. 3.13. Preliminary tests of the RG214 coaxial cables that exit the DC breaks at the top of the vessel and enter the DIII-D annex show that there is variation in signal amplitude on the order of 50% between certain cables, indicating varying lengths and/or losses between the cables. The cables have since been replaced without an accurate measure of the path length difference, so the error associated with a mode number measurement is too high to accurately quantify a toroidal mode number associated with a coherent wave. However, the relative difference between the measured mode numbers in a spectrum of modes can still be evaluated without loss in reliability.

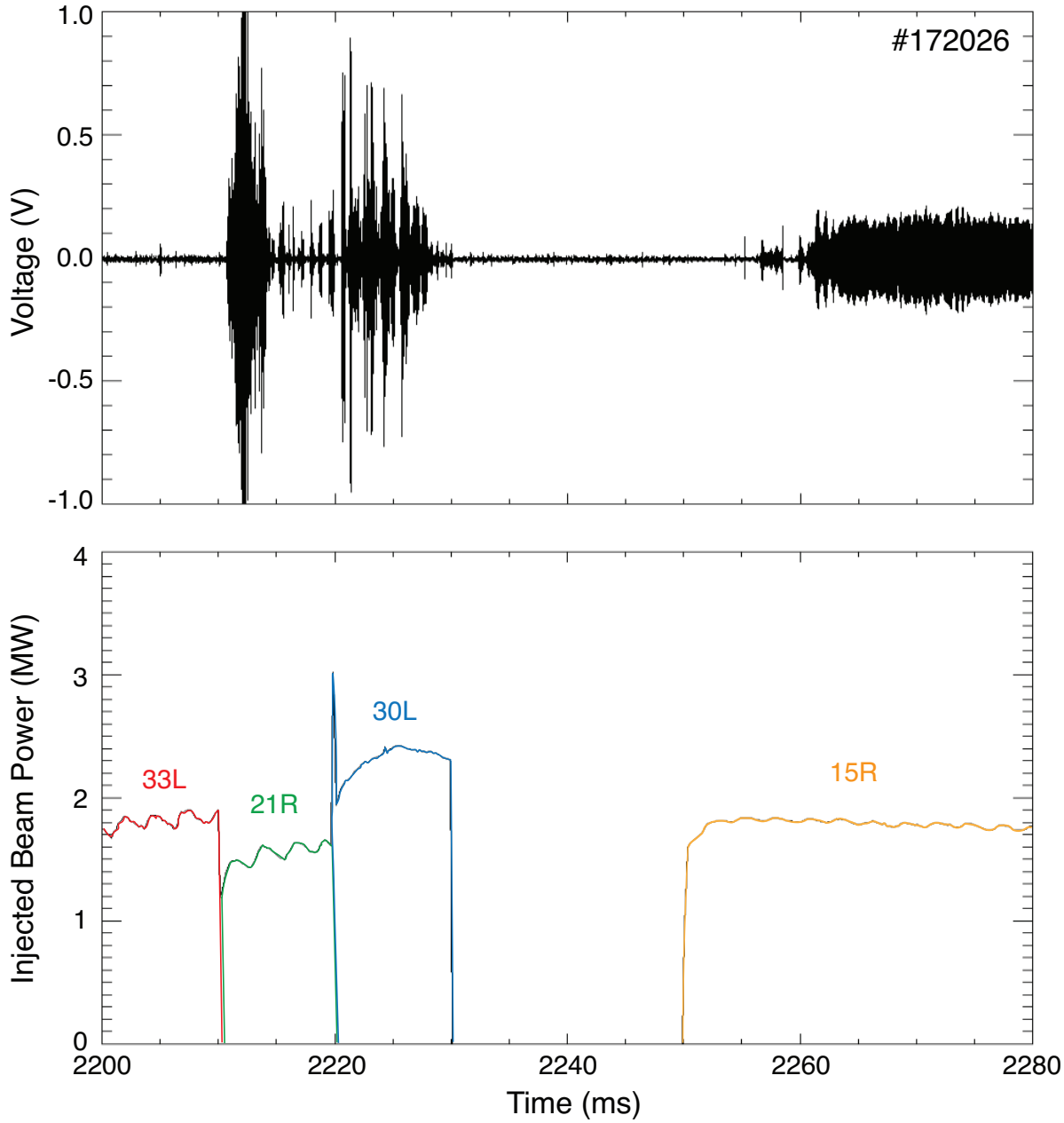

Figure 3.14: An example of the raw signal obtained from one of the magnetic field sensing loops of ICE System 2. Several bursts of magnetic fluctuations are seen in response to neutral beam injection.

CHAPTER 4

Experimental design

CAE/GAE stability was studied over a broad range of parameters during the experiment. These modes are driven unstable by Doppler-shifted cyclotron resonance with fast-ions and are approximately governed by the resonance condition [12] as described in Chapter 2:

$$\omega_{ci} \approx \omega - k_{\|} v_{b\|} \tag{4.1}$$

where ω_{ci} is the cyclotron frequency, $k_{\|}$ is the parallel wave number, and $v_{b\|}$ is the parallel beam velocity. Anisotropy in the fast-ion population is necessary for fast-ion drive of CAE/GAEs [11], so the gradient of the fast-ion distribution with respect to $v_{b\|}$ and $v_{b\perp}$ is also important in mode stability. The experiment was designed with these considerations in mind.

4.1. Plasma conditions and considerations

The experiment was designed as a phase space parameter scan to determine stability thresholds. The primary focus of the experiment was directed towards beam perveance scans in order to separately determine beam density and velocity dependencies of the excited modes for a variety of different beam energies, injection angles, and directions in deuterium plasmas. B_t, I_p, and n_e ramps were also performed to investigate the v_A and ω_{ci} dependence of the modes. Table 4.1 summarizes the plasma parameters that this experiment operated under.

Parameter	Value
Plasma Current I_p	0.7–1.0 MA (Normal dir.)
Toroidal Field B_t	1.28–2.0 T (Normal dir.)
Shape	Inner wall-limited, elliptical
Safety Factor on-axis q_0	0.95
Safety Factor at 0.95 flux surface q_{95}	4.80
Aspect Ratio R/a	$1.72/0.67 = 2.57$
Elongation κ on-axis	1.25

Table 4.1: Experimental parameters.

Here, the "normal direction" indicates that the plasma current I_p is counter-clockwise and the toroidal magnetic field B_t is clockwise as viewed from above, as described in Chapter 3. The shape of the plasma was chosen to be an inner wall-limited, elliptical plasma for simplicity, as shown in an equilibrium reconstruction of the flux surfaces in Fig. 4.1. As mentioned earlier, only L-mode plasmas were studied during this experiment.

4.2. Parametric scans

The focus of this experiment was on understanding how different beam geometries, injection energies, and injection rates affect CAE/GAE activity. To accomplish this, a unique beam programming was utilized to separate the dependence of mode activity on each beam geometry. The beam programming is shown in Fig. 4.2, and the order of the injecting beams is chosen such that it is least likely to cause a disruption of locking due to sudden rotation change. The beams are labeled as described in Chapter 3, and six beams with different injecting geometries were cycled through during each discharge, summarized in Table 4.2. It should be noted that DIII-D has eight beamlines in total, but the beamlines at toroidal angles of 30° and 330° have identical injecting geometries.

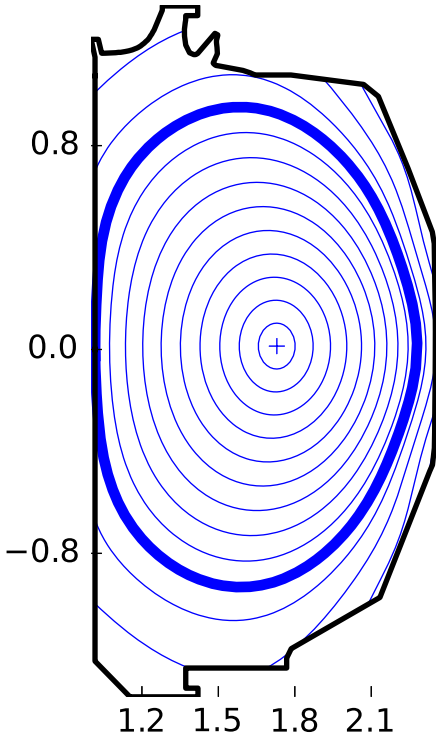

Figure 4.1: For this experiment, the plasma was chosen to be an inner wall-limited, elliptical plasma. The flux surfaces from an equilibrium reconstruction are shown, with the last closed flux surface shown in bold.

Beam Name	Injection Direction	Co- or Ctr- I_p	Tangential/Perpendicular
330L	On-axis	Co-I_p	Tangential
150R	Off-axis	Co-I_p	Tangential
330R	On-axis	Co-I_p	Perpendicular
150L	Off-axis	Co-I_p	Perpendicular
210L	On-axis	Ctr-I_p	Tangential
210R	On-axis	Ctr-I_p	Perpendicular

Table 4.2: The different beams and their injection geometries used during the experiment.

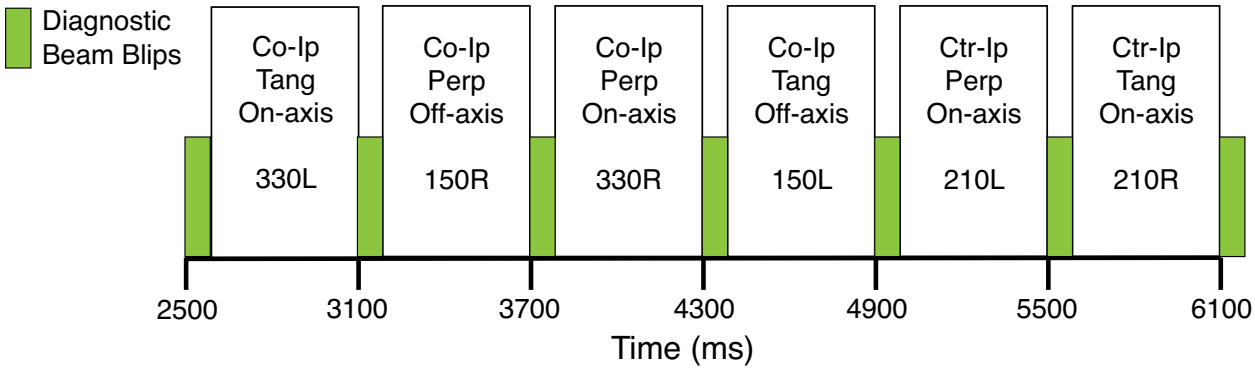

Figure 4.2: The beam programming for the experiment. Each of the six beams with different injection geometries is cycled through during each discharge, preceded by a < 100 ms period of diagnostic beam blips.

As mentioned in Chapter 3, several diagnostics rely on NBI. CER uses the charge exchange process between bulk ions and energetic particles from NBI to measure the ion temperature, impurity density, and rotation speed profiles. FIDA analyzes the spectral line of this charge exchange process to diagnose components of the fast-ion velocity distribution. MSE utilizes the spectral emission from injected energetic particles to provide measurements of the pitch angle profile of the magnetic field, giving information on the tokamak safety factor q as well as the profile of the radial electric field. The information provided by these diagnostics are all essential in calculations such as

equilibrium reconstruction and modeling of the fast-ion population. The programming for these diagnostic beam blips is shown in Fig. 4.3. Each beam blip lasts 10 ms and involved a beam injecting at full power (81 keV).

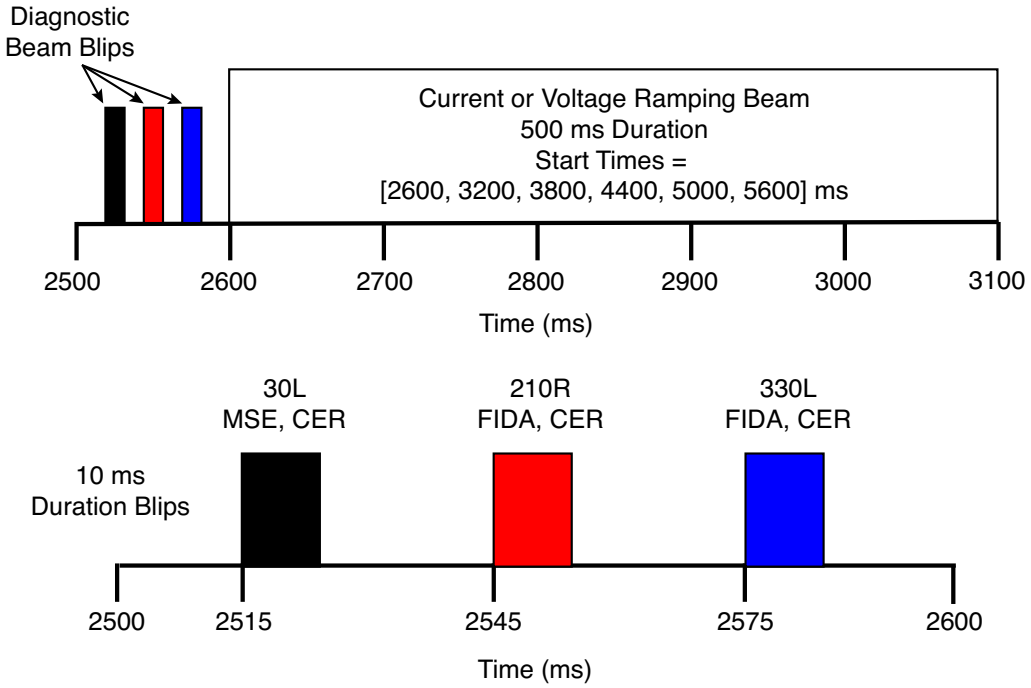

Figure 4.3: Diagnostic beam blips used during the experiment. These blips occurred before the start of each beam-on period.

4.2.1. Beam perveance scans

Beam perveance scans were an essential part of this experiment. This is a uniquely applied capability of the DIII-D beams, and it allowed for the separate variation of beam current and voltage, which offers an opportunity to separately determine beam density and velocity dependencies of any excited modes. Each of these scans was performed at magnetic fields between $1.28 - 2.0$ T.

The process of doing these perveance scans is visualized in Fig. 4.4. The optimal operating parameters for the beams to maintain acceptable beam divergence are approximately between voltages of $60 - 75$ keV, source currents of $46.25 - 62.5$ A and powers of $1.0 - 2.0$ MW, though in practice each beam had different operating capabilities in terms of

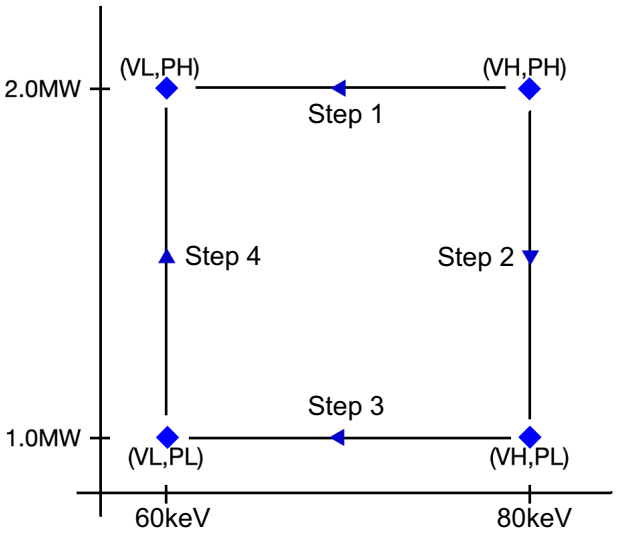

Figure 4.4: Beam perveance scans performed during the experiment. Sequentially, the beam current and voltage were varied separately.

maximum power and voltage. These scans utilized the programming as shown in the upper figure of Fig. 4.3. Following the diagnostic beam blips, a current or voltage ramp lasting 500 ms occurred. Each of the six beams was cycled through throughout the duration of the discharge, and every step in Fig. 4.4 refers to a separate discharge. For example, a beam was held at constant high source current (PH) and the voltage was scanned from 75 $\rightarrow$ 60 keV (VH $\rightarrow$ VL) in Step 1. In the next discharge, in Step 2, the beam was held at constant high voltage (VH) and the source current was scanned from 62.5 $\rightarrow$ 46.25 A, nominally, such that the power ramped from 2.0 $\rightarrow$ 1.0 MW (PH $\rightarrow$ PL), and so on. As mentioned in Chapter 3, it is important to note that the nominal value for the source current is not the same as the current that enters the plasma due to losses from neutralization and collimation processes in the beamline. Therefore, for the analysis presented here, the beam injection rate will be used and is calculated as beam power divided by voltage in keV, expressed for convenience in Amps. During each discharge, the injection rate was ramped down by up to $\sim 40\%$.

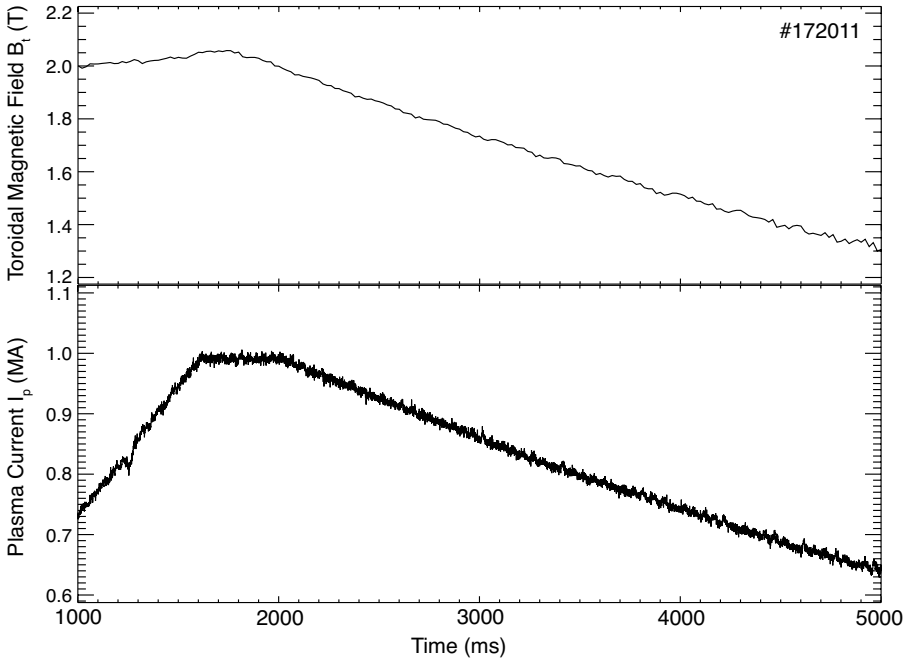

Figure 4.5: The toroidal magnetic field B_t was ramped from $\sim 2.0 \rightarrow 1.3$ T during a magnetic field scan. The plasma current I_p was ramped concurrently to keep B_t/I_p constant.

4.2.2. Magnetic field scans

In addition to the beam perveance scans, other parameter scans were also performed throughout the course of the experiment. These included toroidal magnetic field scans, as shown in Fig. 4.5. During these discharges, the magnetic field B_t was ramped down through decay from $\sim 2.0 \rightarrow 1.3$ T with the motivation of identifying a magnetic field threshold for the onset of CAE/GAEs. The plasma current I_p was concurrently ramped in order to keep B_t/I_p constant; this was intended to keep the tokamak safety factor q constant, which is important in the stability of GAEs as mentioned in Chapter 2.

4.3. Measurements of Alfvén eigenmodes

In this experiment, a wide variety of parameter scans were performed. Notably, high frequency AEs were observed at most $B_t \leq 1.8$ T. Beam perveance scans were performed at magnetic fields of $1.28 - 2.0$ T and beam energies ranging from $V_b \sim 60 - 75$ keV.

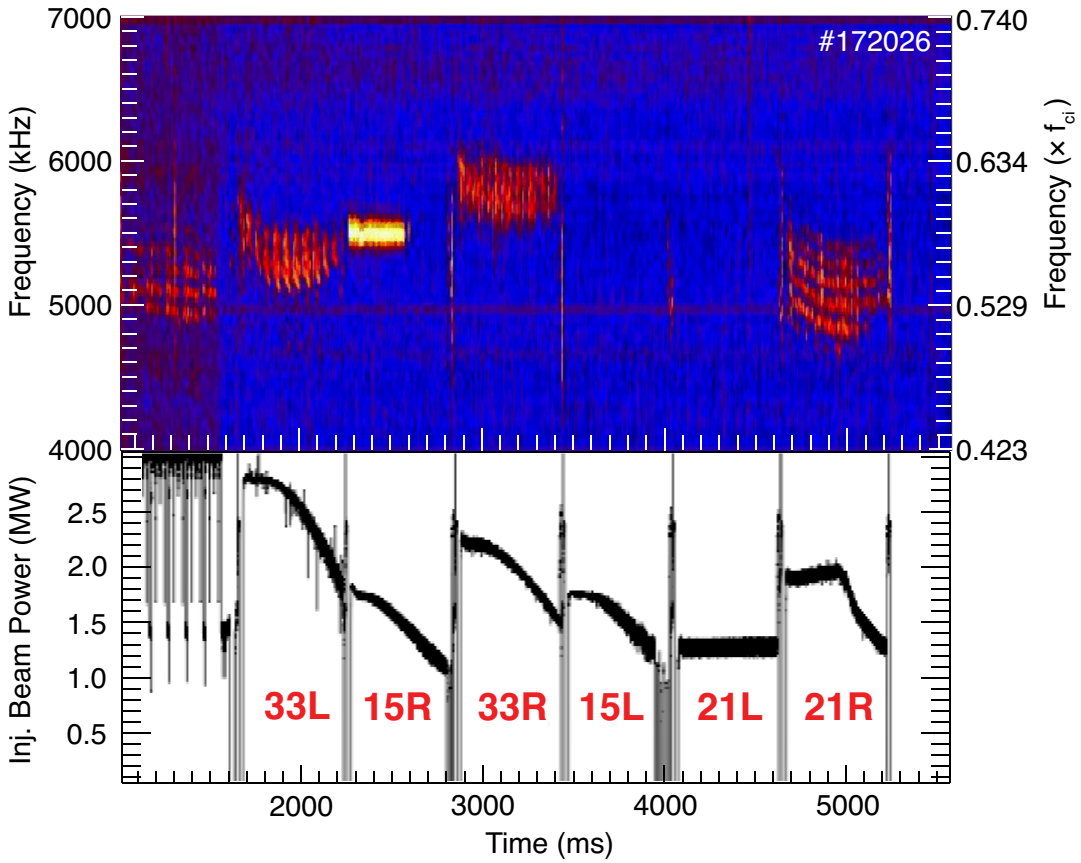

Figure 4.6: During a $B_t = 1.28$ T discharge, beam injection rate scans were performed at constant high beam voltage of $V_b \sim 75$ keV for six different beam geometries. Different beams excited modes at different frequencies, and four of the six total geometries were found to excite modes.

4.3.1. Dependence on beam geometry

Fig. 4.6 shows discharge #172026, a beam perveance scan at the lowest magnetic field of $B_t = 1.28$ T and highest beam voltage of $V_b \sim 75$ keV, yielding a wide range of CAE/GAE activity. At this field, the cyclotron frequency was $f_{ci} = 9460$ kHz at the magnetic axis, and the observed mode activity occurs at a high fraction of f_{ci} ($f \sim 0.6 f_{ci}$). It is seen from the figure that high frequency AEs were excited by four of the six different beam geometries (33L, 15R, 33R, and 21R), including a counter-I_p injecting beam (21R) and an off-axis beam (15R). The perveance scans are shown in the lower plot of Fig. 4.6; notably,

not all beams operated at full voltages and currents. Table 4.3 summarizes the operating parameters of the beams used during this scan. Different beams were found to excite modes at different frequencies.

Beam name	Operating voltage	Source current range
33L	75 keV	$72 \rightarrow 51$ A
15R	75 keV	$58 \rightarrow 43$ A
33R	75 keV	$66 \rightarrow 49$ A
15L	75 keV	$58 \rightarrow 43$ A
21L	62 keV	$37 \rightarrow 37$ A
21R	76 keV	$56 \rightarrow 44$ A

Table 4.3: Beam operating parameters during the beam perveance scan. Each beam was held at constant high voltage while the source current was ramped down.

The focus of the analysis in the next chapter will be on the spectrum of modes at $\sim 2250 - 2750$ ms excited by the off-axis co-injecting tangential beam 15R. This spectrum of modes is the only threshold observed across the wide range of beam perveance scans, though other beams do excite modes that closely approach a threshold. Seen in Fig. 4.6, the modes excited by the 21R beam appear to have amplitude that decreases with current and are almost stabilized. The 33L and 33R beams also appear to excite modes that may decrease in power with current. These are not analyzed in this dissertation and are the subject of future work. Importantly, the observed threshold from the 15R beam was repeatable as approximately the same threshold was observed during several repeat discharges during the experiment that had the same plasma parameters and beam injection rate scans.

4.3.2. Dependence on other plasma parameters

The following section describes observations that were made during the experiment but deeper analysis is left to future work.

4.3.2.1. B_t ramp observations

A B_t threshold was observed for AE excitation during a discharge in which the toroidal field was ramped down from $\sim 2.0 \rightarrow 1.2$ T, as seen in Fig. 4.7. The modes appear to be driven unstable once the toroidal field reaches a value of $B_t < 1.6$ T, corresponding to an Alfvén velocity of $v_A = 3.41 \times 10^6$ m/s with a beam injection velocity of $v_b = 2.8 \times 10^6$ m/s. As mentioned earlier, the plasma current I_p was ramped down concurrently to maintain a constant q.

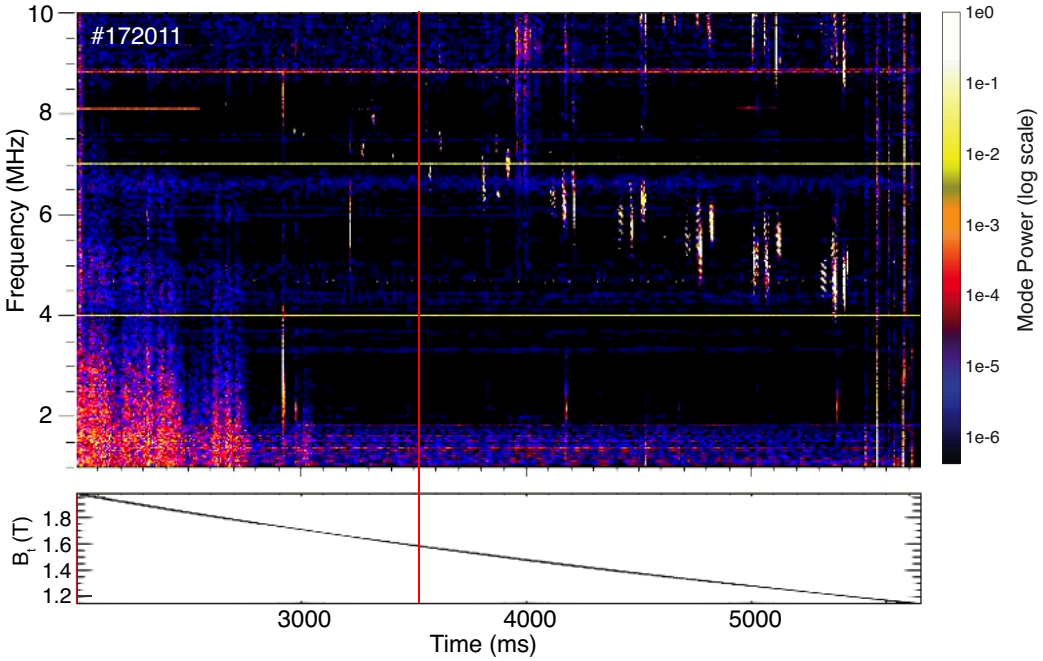

Figure 4.7: A B_t threshold of $\sim$ 1.6 T was observed for the excitation of high frequency AEs during a B_t ramp discharge.

During this discharge, it is interesting to note that the frequencies of the excited modes are consistent with analytic theory which predicts high frequency AEs to be driven unstable at frequencies of $f/f_{ci} > 0.5$ [60], which is shown by the $0.5 f_{ci}$ line in Fig. 4.8. The spectrum consists of several, likely distinct, bursting modes. Additionally, the frequencies of the excited modes appear to be proportional to the Alfvén velocity v_A as shown in Fig. 4.9. However, because the electron density n_e is relatively constant over the B_t ramp, there is no way to distinguish between the frequency scaling with f_{ci} or with v_A.

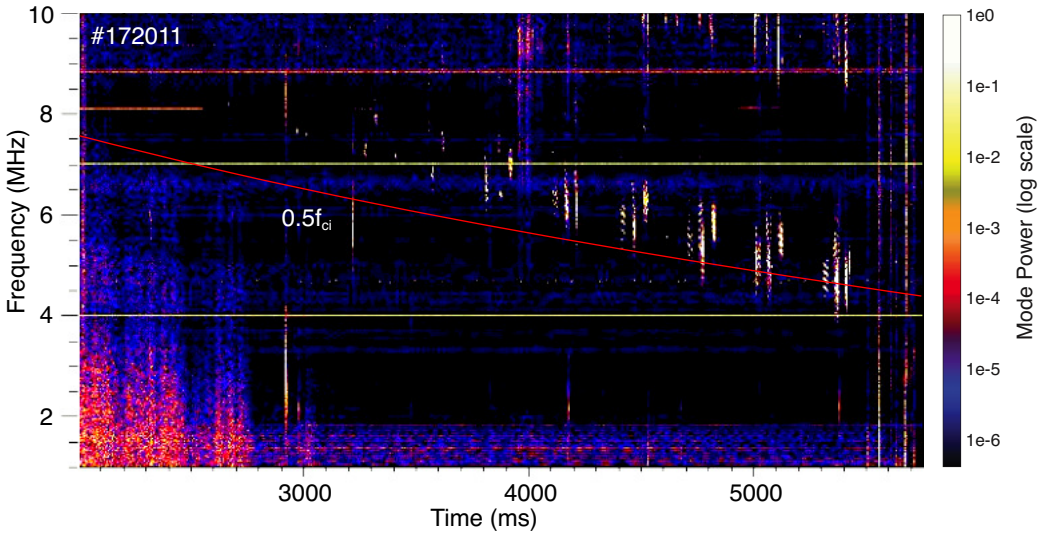

Figure 4.8: The $0.5f_{ci}$ line is plotted on top of the AE spectrum during a B_t ramp, showing that the frequencies of the modes are consistent with analytic theory predicting unstable AEs above $f/f_{ci} > 0.5$.

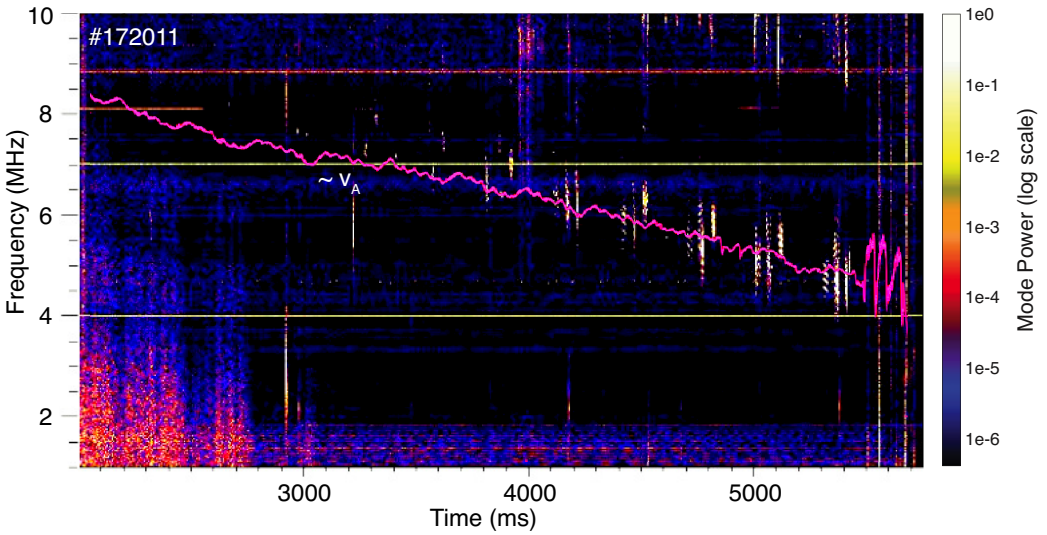

Figure 4.9: The Alfvén velocity v_A is plotted on top of the AE spectrum during a B_t ramp, showing that the frequency of the modes is proportional to v_A.

4.3.2.2. n_e ramp observations

An electron density ramp was performed on a discharge at $B_t = 1.33$ T. As shown in the bottom plot of Fig. 4.10, the density n_e is increased by a factor of ~ 2 from $\sim 2.2 \times 10^{13}$ cm^{-3} to $> 4.0 \times 10^{13}$ cm^{-3}. Mode onset occurs before the electron density increases appreciably, at around $n_e = 2.4 \times 10^{13}$ cm^{-3}. An interesting observation here is that the frequency is not proportional to the Alfvén speed v_A; the density rises by a factor of ~ 2, but the frequency does not drop by a factor of $\sqrt{2}$ as expected by the low frequency Alfvén dispersion relations in Section 2.1. This is likely because the low frequency dispersion relations are not valid in the regime where $f \sim f_{ci}$, which is certainly true here: the cyclotron frequency f_{ci} in this discharge is around 10 MHz, so $f/f_c \sim 0.6$.

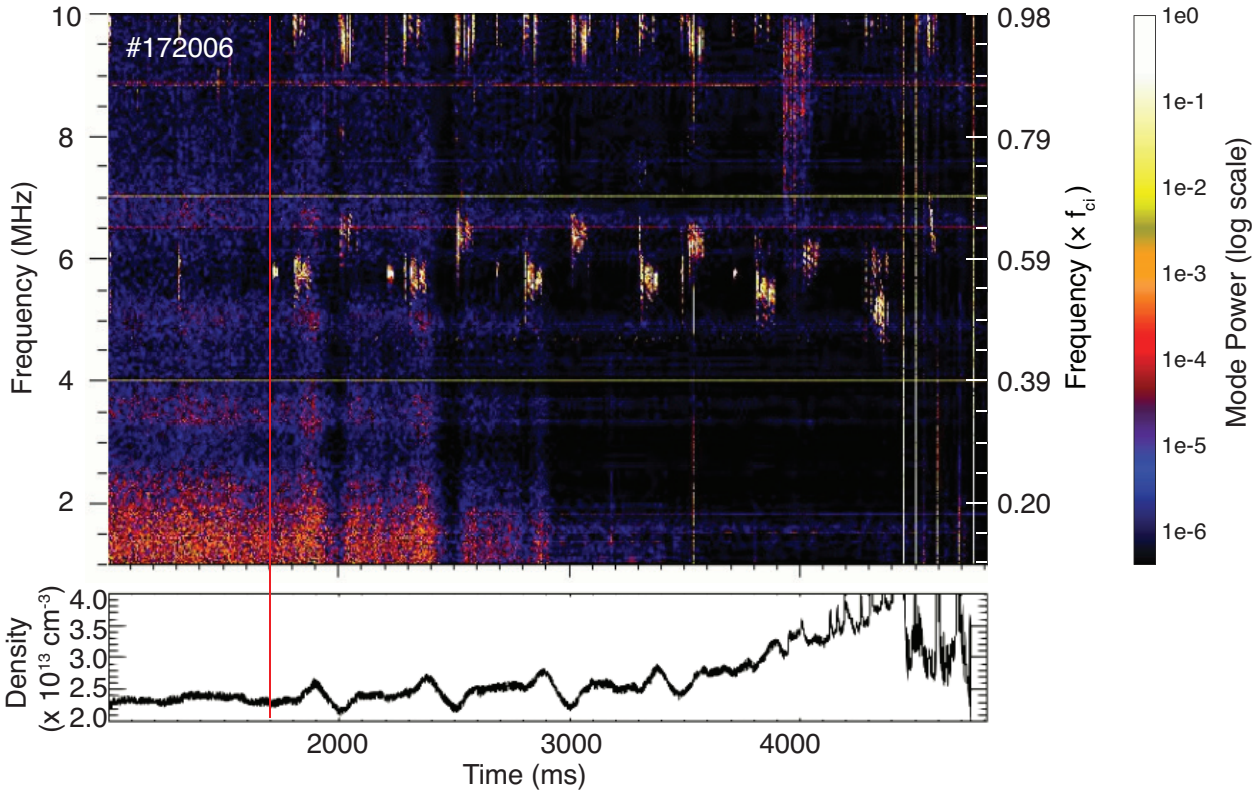

Figure 4.10: An n_e scan in which the electron density is increased by a factor of ~ 2 shows the frequencies of the unstable modes are not proportional to the Alfvén speed v_A.

Within a single mode within the spectrum, however, the frequency does scale with the Alfvén speed, as shown in Fig. 4.11. The green line in the figure is drawn to be

proportional to v_A calculated from the electron density. Clearly, the frequency of the mode follows v_A within each burst of mode activity; as density ramps upwards, v_A decreases, and frequency decreases as well. This may indicate that the mode number is changing with each burst in the spectrum, since the overall frequency of the spectrum does not follow the Alfvén speed.

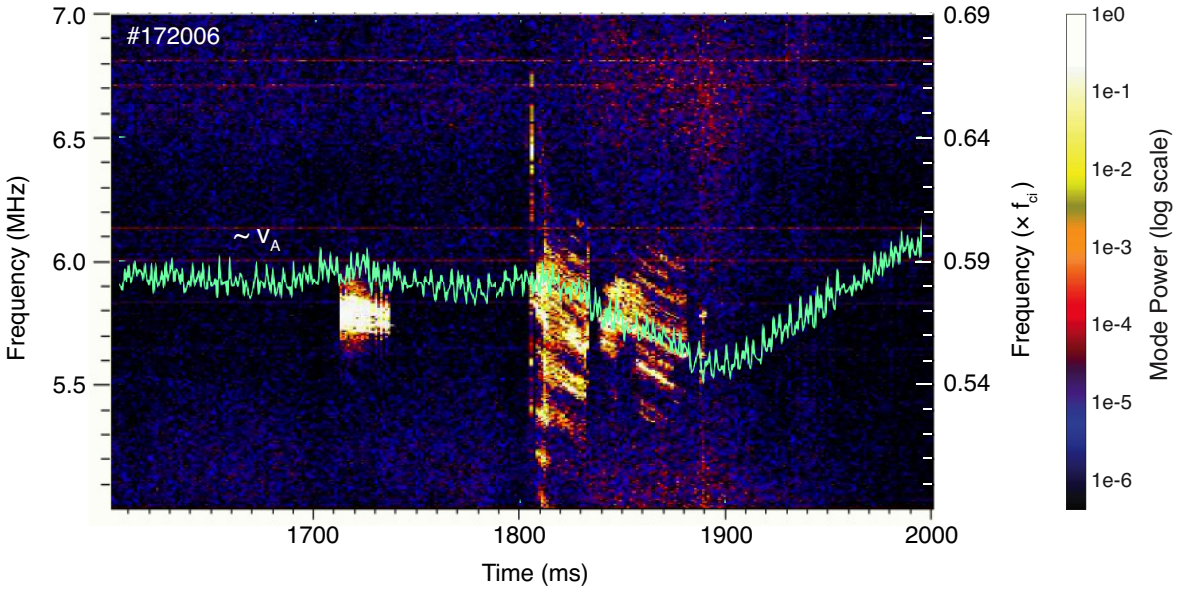

Figure 4.11: Within a burst of mode activity, the frequency scales with the Alfvén speed (drawn in green).

Throughout the parameter scans in the experiment, many thresholds for mode onset were observed. As stated earlier, the focus of the analysis in the following chapter will be on the only threshold observed for a beam perveance scan, in which a spectrum of modes was controllably stabilized during a beam current ramp.

CHAPTER 5

Controlled fast-ion density ramp stabilizing AEs

The discharge of interest is one in which the beam injection rate was ramped down by $\sim 40\%$ while beam voltage (energy) was held constant. During this discharge, the 150R beam (the off-axis perpendicular beam) was held at constant beam energy of $V \sim 75$ keV for a $B_t \sim 1.28$ T plasma. Shortly after the 150R beam began to inject, a highly coherent spectrum of modes was observed to be excited, shown in Fig. 5.2. It is important to note that in this plasma, the cyclotron frequency was $f_{ci} = 9460$ kHz at the magnetic axis, $R_0 = 1.72$ m, and the Alfvén velocity was $v_A = 3.26 \times 10^6$ m/s on axis for this plasma. The slowing-down time of the beam ions is $t < 50$ ms, calculated from the transport modeling code TRANSP [61, 62]. These values are summarized in Table. 5.1.

Plasma parameter	Value
Toroidal magnetic field B_t	1.28 T
Ion cyclotron frequency f_{ci}	9460 kHz
Magnetic axis R_0	1.72 m
Alfvén velocity v_A	3.26×10^6 m/s on axis
Slowing-down time of fast-ions	< 50 ms
Electron temperature T_e	1.2 keV
Electron density n_e	3.45×10^{13} cm^{-3} on axis
Electron thermal velocity $v_{\mathrm{e,th}}$	1.45×10^7 m/s
Ion thermal velocity $v_{\mathrm{i,th}}$	2.19×10^5 m/s
$v_{\mathrm{e,th}}/v_A$	4.45
$v_{\mathrm{i,th}}/v_A$	0.0675

Table 5.1: Plasma parameters during the experiment.

It should also be noted that the toroidal field B_t and plasma current I_p were constant during the time range of interest, and other parameters such as temperature and density were effectively constant variations of $< 12\%$. The cyclotron frequency f_{ci} has a fractional variation of about 28% from its value at the magnetic axis across the radial extent of the plasma. These are summarized in Table 5.2.

Plasma parameter	% Variation
Toroidal magnetic field B_t	$< 2\%$
Plasma current I_p	$< 0.4\%$
Electron density n_e	$< 11\%$
Electron temperature T_e	$< 12\%$

Table 5.2: Plasma parameters and their % variation during the time range of interest.

This plasma featured a peaked density profile, with safety factor $q \sim 1$ for minor radius $r < 20$ cm (corresponding to normalized effective plasma radius $\rho_{\text{eff}} < 0.3$), rising steeply for $r > 20$ cm. The density profile, as well as the ion temperature, electron temperature, and q profiles are shown in Fig. 5.1. The ion temperature T_i and plasma rotation frequency f_{ROT} are estimated from the CER diagnostic, which utilizes a diagnostic beam blip taken $\sim 20 - 30$ ms before the turn-on of the exciting 150R beam. They are approximated to be $T_i \sim 1$ keV and $f_{\text{ROT}} \sim 7$ kHz.

5.1. Stabilization of AEs

Fig. 5.2(a) shows the magnetic fluctuation level $|\delta b|^2$ versus frequency and time on a logarithmic color scale under a 60 dB mask (meaning only portions of the spectrum within six orders of magnitude of the maximum mode power are shown). Fig. 5.2(b) shows the raw signal of the magnetics measurement from the ICE loops. The onset of this spectrum

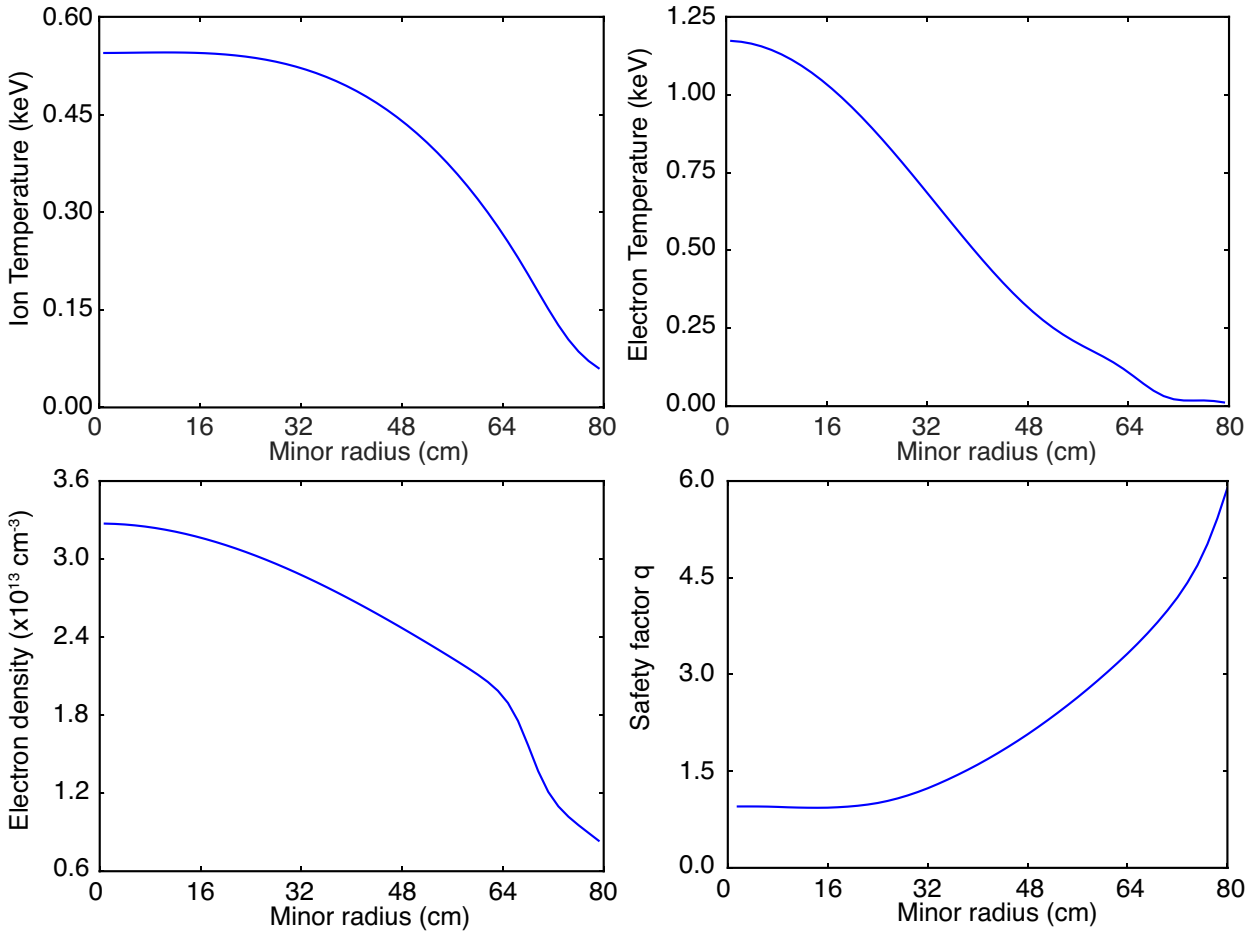

Figure 5.1: Profiles for ion temperature T_i, electron temperature T_e, electron density n_e, and tokamak safety factor q during the experiment.

of modes was at $t = 2260$ ms, about ~ 10 ms after the beam was turned on. These modes were observed at frequencies of $f \sim 5500 - 5600$ kHz, or $f \sim 0.58 f_{ci}$. As shown in Fig. 5.3, the spectrum at the time of mode onset ($t \sim 2260$ ms) appears to consist of a broader band, lower power structure at $f \sim 5550$ kHz, combined with two narrow band modes, one with high power at $f \sim 5520$ kHz and one with lower power at $f \sim 5490$ kHz, separated by a ~ 30 kHz frequency gap. The $f \sim 5520$ kHz narrow band peak is overwhelmingly higher power than the other peaks by $\sim 2 - 3$ orders of magnitude, and the noise level of the ICE diagnostic was over six orders of magnitude below the highest power peak.

Fig. 5.2(c, d) shows the time history of mode power with relation to the injection rate of the exciting 150R beam. As the beam injection rate crosses below a threshold of ~ 18.5 A, the mode power $|\delta b|^2$ abruptly drops to zero. $|\delta b|^2$ does not undergo a smooth decrease to the noise level; it drops over 6 orders of magnitude in power in less than 3 ms. The spectrum is briefly re-excited at $t \sim 2585$ ms, but shuts off immediately. During this re-excitation, a higher frequency mode becomes the dominant mode in the spectrum. This feature will be discussed in detail below. The raw fluctuation trace from the ICE loops is shown in Fig. 5.5 along with RMS power for the time range during which the mode is stabilized and then briefly re-excited. In Fig. 5.5(c) the time window around mode stabilization is shown in detail, where the voltage envelope of the signal decays approximately exponentially.

The 10 ms delay between beam turn-on and mode onset (shown in Fig. 5.2(b,c)) is expected because a delay is required for resonant fast-ions to build up for mode drive. This delay is likely also caused in part by a remnant population of fast-ions from a beam with different injection geometry that turned off ~ 20 ms before the turn-on of the 150R beam, since the slowing-down time was < 50 ms. A similar delay is not expected between the injection rate crossing the threshold and stabilization of the modes because the beam distribution evolves very slowly. The raw fluctuation trace from the ICE loops is shown in Fig. 5.4 along with the RMS power for the time range during which the mode is first excited.

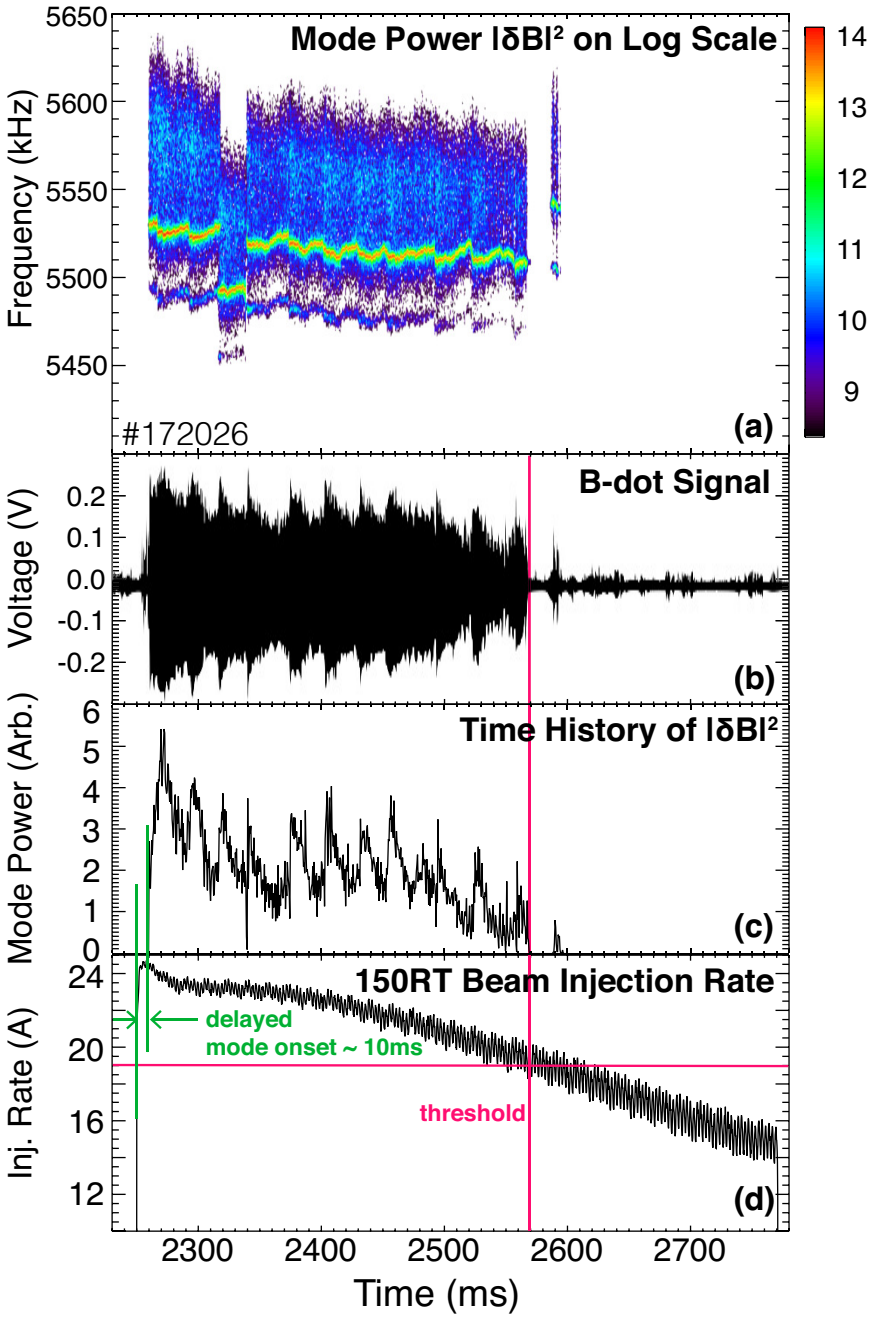

Figure 5.2: (a) $|\delta b|^2$ spectrum on a logarithmic scale showing a highly coherent spectrum of high-frequency Alfvén eigenmodes at $f \sim 5550$ kHz. (b) The raw fluctuation trace from the ICE loops. (c) Mode power $|\delta b|^2$ versus time and (d) beam injection rate versus time. Mode onset is ~ 10 ms after turn-on of the 150R beam, and the mode shuts off once beam injection rate crosses a threshold of ~ 18.5 A.

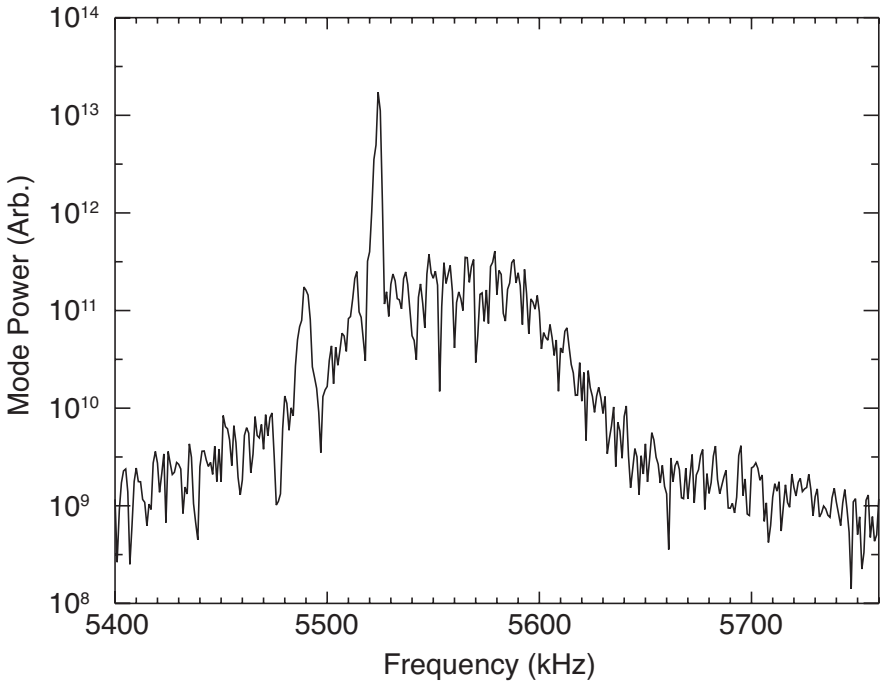

Figure 5.3: Mode power versus frequency at mode onset (t = 2260 ms) shows the highest power, narrow band peak at 5520 kHz.

5.2. Effects of sawtooth oscillations on mode stability

5.2.1. The Kadomtsev Model

Several models of the sawtooth instability have been proposed to be able to predict its properties in tokamak experiments. The most well-known of these is the Kadomtsev model, which describes a fast magnetic reconnection that occurs during the sawtooth crash [63]. In the Kadomtsev model, during each sawtooth oscillation an $m = 1$ magnetic island [1] forms when field lines inside and outside of the $q = 1$ flux surface reconnect with each other. This magnetic island grows, causing the hot plasma in the core to mix with the cooler plasma outside the $q = 1$ flux surface, flattening the temperature and density profiles. Eventually, the magnetic island replaces the plasma core and restores the q on axis to unity. This model is known as the Kadomtsev model with full magnetic reconnection [63], and an illustration of how the magnetic field evolves during the instability is shown in Fig. 5.6.

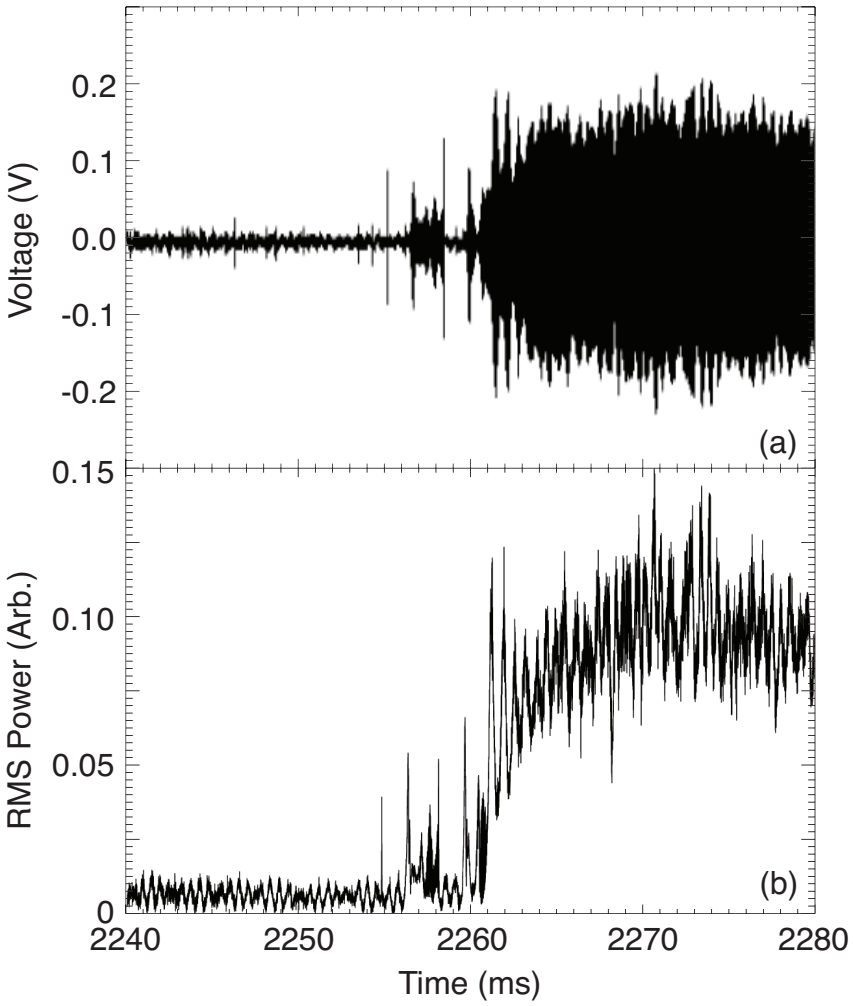

Figure 5.4: (a) The raw fluctuation trace from the ICE loops and (b) the RMS power, averaged over each 1 μs, versus time for the time range during which the mode is excited.

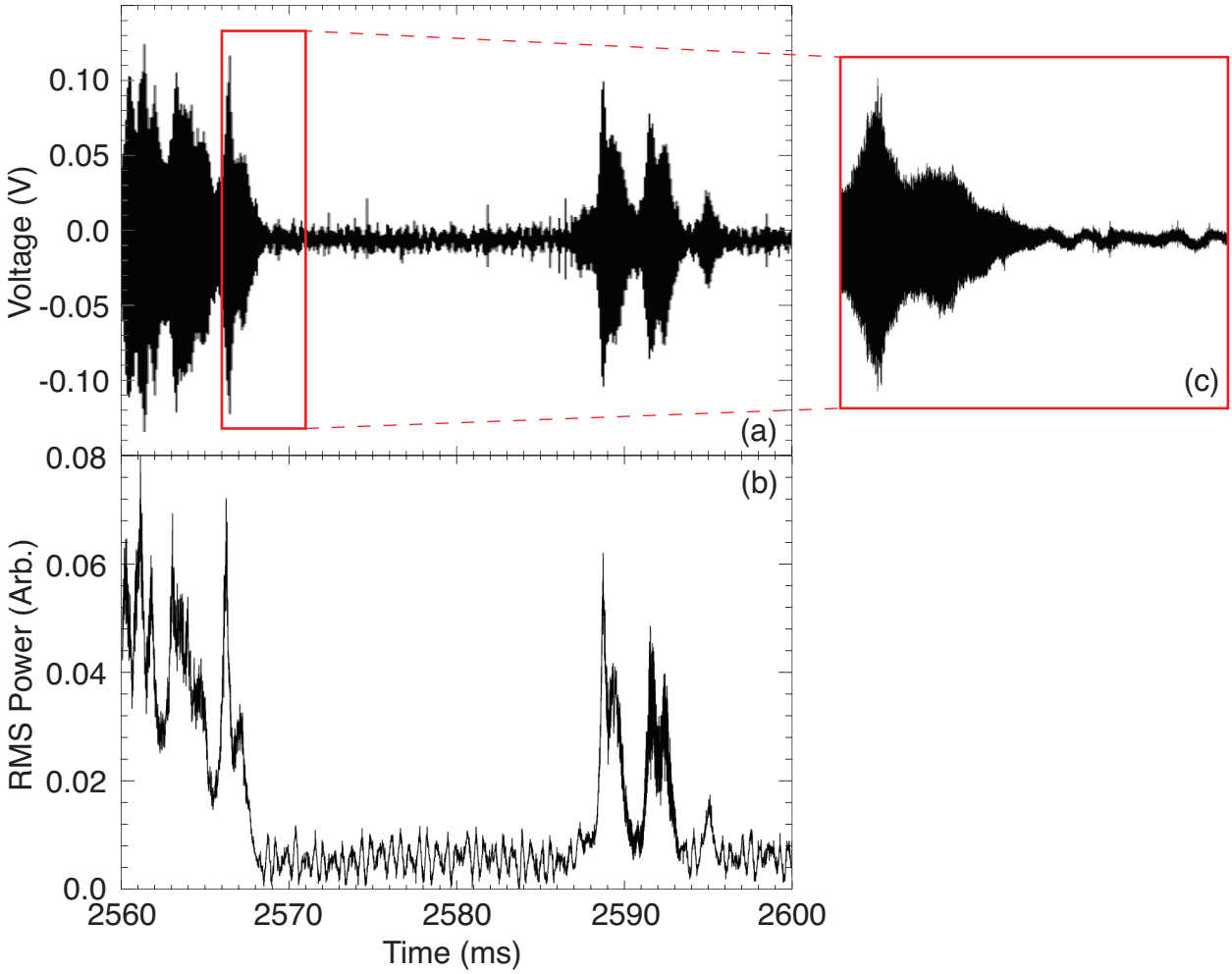

Figure 5.5: (a) The raw fluctuation trace from the ICE loops and (b) the RMS power, averaged over each 1 μs, versus time for the time range during which the mode is stabilized and then briefly re-excited. (c) The time window around mode stabilization in detail showing the exponential decay of the voltage envelope.

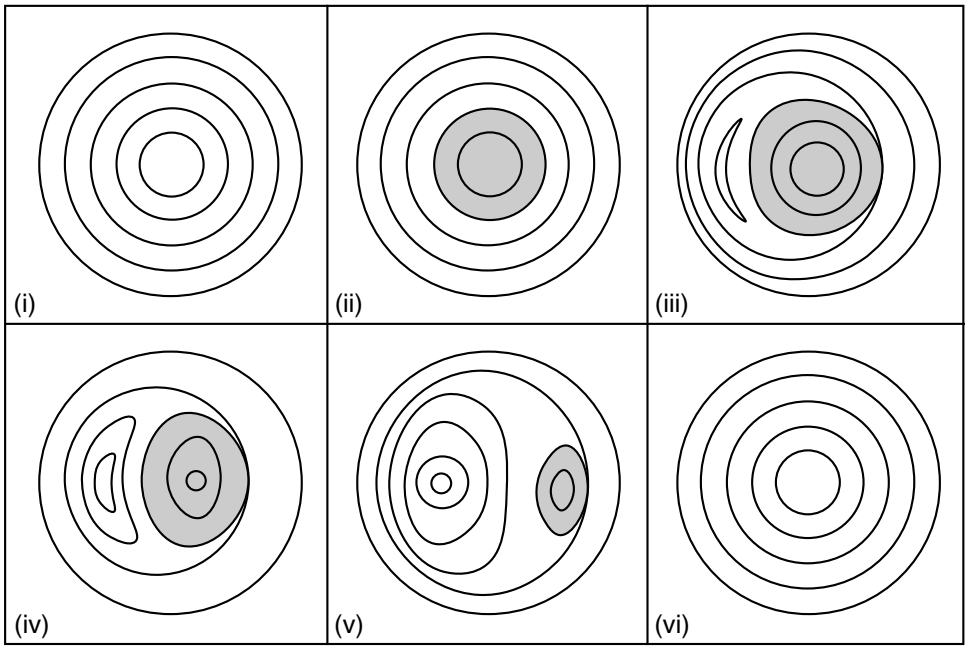

Figure 5.6: Development of the magnetic field structure during the sawtooth instability according to Kadomtsev's model, following Ref. [1]. The shaded region shows where $q < 1$, and the $m = 1$ instability displaces it and restores q at the core to unity.

Other models of the sawtooth instability have been developed, such as the Wesson model [64] which describes a quasi-interchange instability [65] causing the crash, or the Porcelli model [66] which predicts sawtooth trigger times. The Kadomtsev model has also been modified such that the magnetic flux is only partially reconnected during each sawtooth crash [67]; this model works well for discharges with q values that remain below unity even after each crash. For the results discussed in this thesis, however, only the Kadomtsev model with full magnetic reconnection was used.

5.2.2. Sawtooth oscillations during experiment

Sawtooth oscillations were present in this plasma before, during, and after the time range of interest. This can be seen in Fig. 5.7, which shows ECE data for electron temperature near the edge of the plasma varying with each sawtooth crash (referencing Fig. 5.2, the 150R beam injects from $t = 2250 - 2770$ ms).

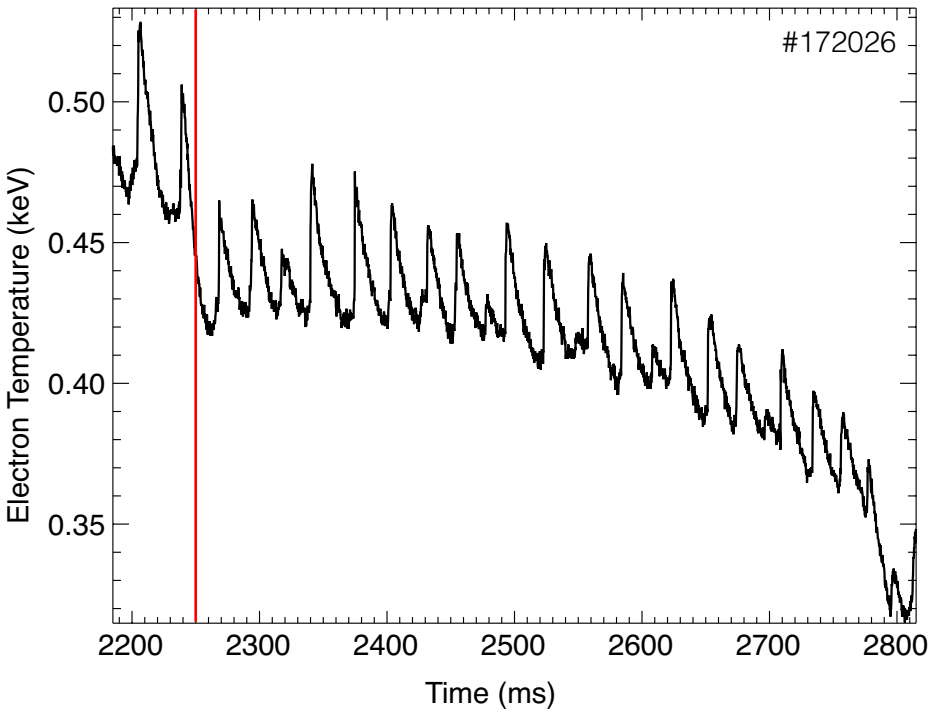

Figure 5.7: ECE data showing electron temperature at the outer region of the plasma modulating during sawtooth oscillations. The red line indicates the time that the 150R beam turns on.

From Fig. 5.2(b), it is apparent that sawtooth oscillations modulate the mode power by as much as 50%. A sawtooth event is likely responsible for the brief re-excitation in the spectrum at $t \sim 2575$ ms as it causes small changes to the equilibrium and fast-ion distribution. A double sawtooth crash is also responsible for the change in the spectrum at $t \sim 2320$ ms, where the lower frequency mode at $f \sim 5490$ kHz temporarily becomes the dominant mode. It is important to note that the presence of sawteeth complicate this analysis, as the oscillations cause intermittent fast-ion transport throughout the beam ramp. A complete picture of the effects of sawtooth oscillations on mode stability is not known and constitutes future work.

5.3. Damping considerations

As mentioned in Section 2.8, AEs are expected to be damped primarily by continuum damping and electron thermal damping such as Landau damping. The background damping rate does not have dependence on properties of the fast-ions or the fast-ion distribution. Table 5.2 shows that plasma parameters such as toroidal magnetic field B_t, plasma current I_p, electron density n_e, and electron temperature T_e were effectively constant during the current ramp. n_e and T_e in the core of the plasma (at the magnetic axis) are shown in Fig. 5.8.

From Eq. 2.37, AEs should have electron thermal damping that scales as β_e, the electron beta, where $\beta_e = \frac{P_e}{B^2/2\mu_0}$ where P_e is the electron pressure and B is the magnetic field. The poloidal electron beta, over the time range in which the current ramp took place, is shown in Fig. 5.9. It is apparent that β_e decreases slightly during the current ramp, by about 12%, which suggests that the electron thermal damping rate should also decrease during this time.

From these considerations, it can be estimated that background damping of these modes should be either constant or decreasing slightly and that the effects of damping on mode stabilization should be negligible compared to the changes in fast-ion drive.

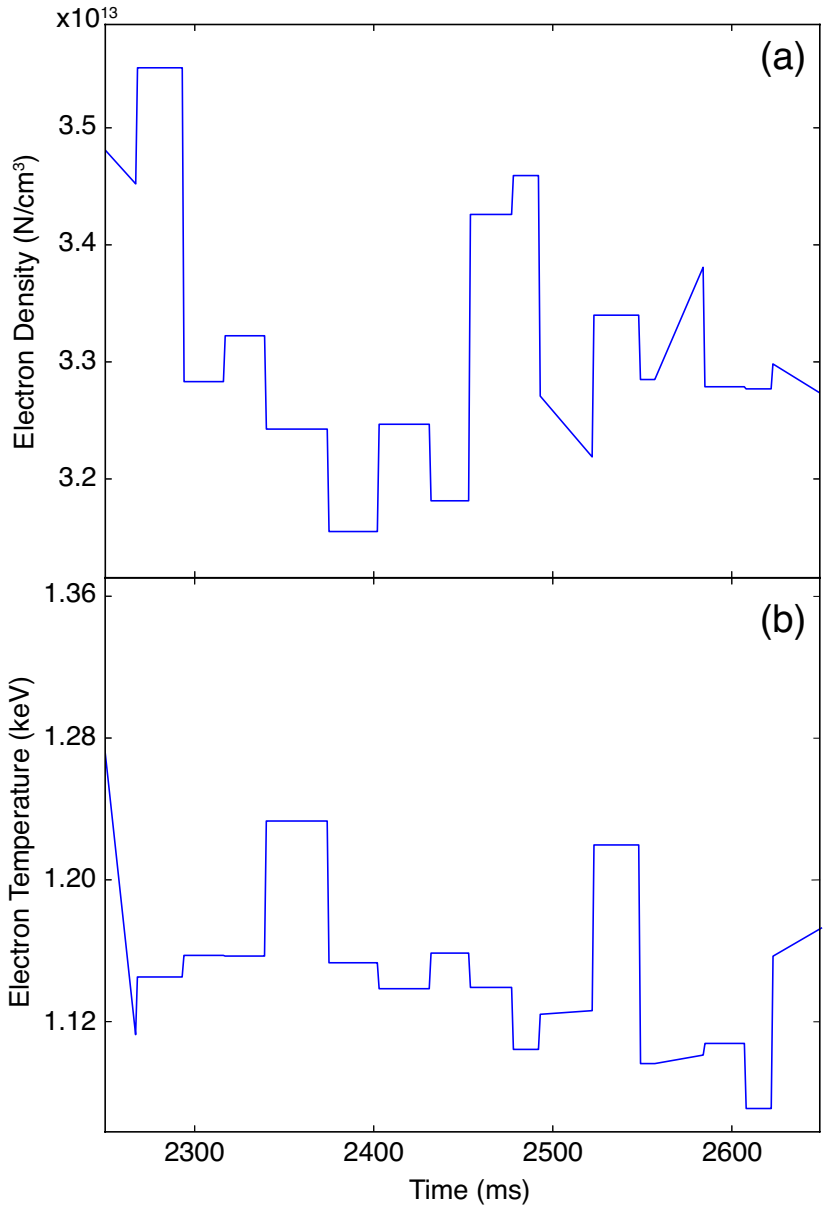

Figure 5.8: (a) Electron density and (b) electron temperature at the magnetic axis over the time range of the current ramp, calculated from TRANSP.

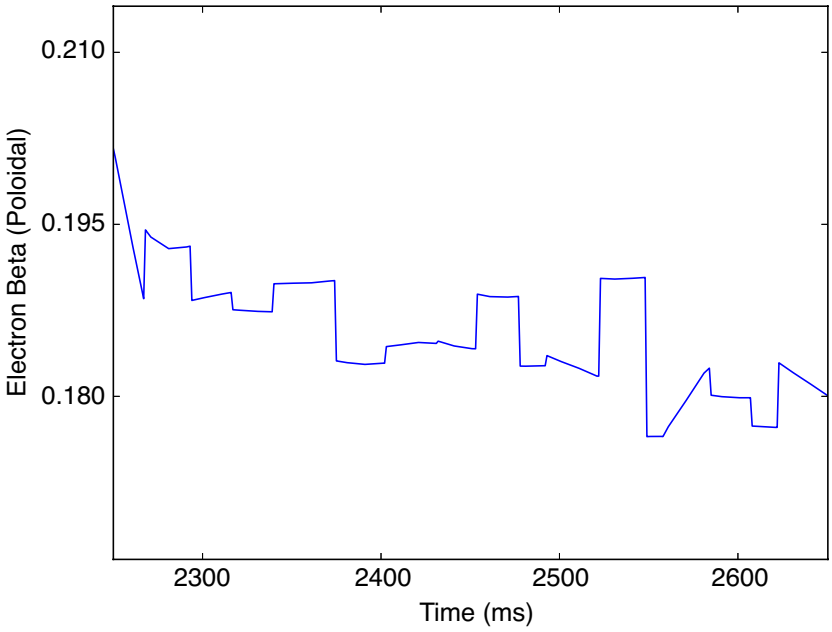

Figure 5.9: The poloidal electron beta of the plasma during the current ramp, calculated from TRANSP.

5.4. Beam current scaling with mode power

Fig. 5.10 shows the mode power $|\delta b|^2$ versus beam injection rate I_b, with the instability threshold at $I_b \sim 18.5$ A. Due to sawteeth being present during the lifetime of the mode, only the points within 7 ms preceding a sawtooth crash were considered for determining the scaling between mode power and injection rate. This window allows for maximum relaxation to the fast-ion distribution without sawteeth as the minimum time between sawtooth crashes is 14 ms. However, sawtooth oscillations were likely responsible for residual redistributions of the fast-ion population that were not accounted for in this analysis and could cause significant deviations from the expected scaling. The marginal excitation of the mode, however, is present regardless of sawteeth.

The observation of a threshold demonstrates a fundamental property of resonant-driven AEs: that the growth rate of these modes is set by the competition between fast-ion drive and damping processes like Landau damping. Previous simulations of CAEs have demonstrated this property, as shown in Fig. 5.11. The beam density was varied while

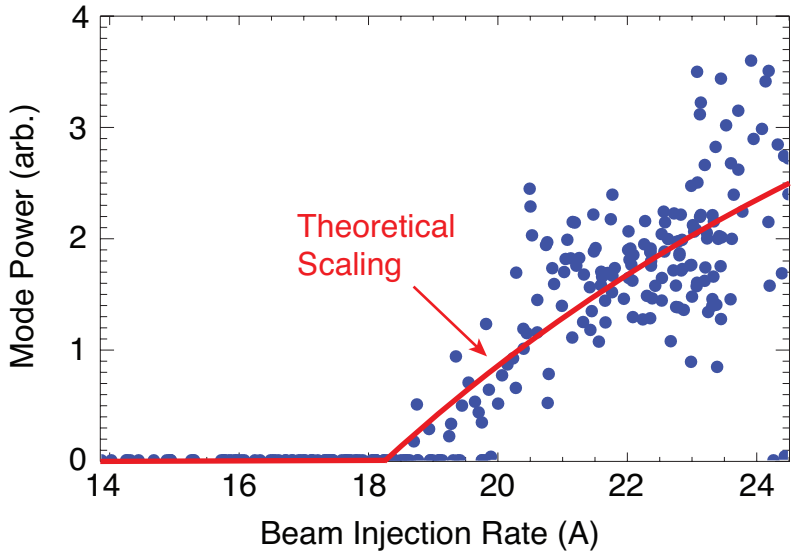

Figure 5.10: Mode power $|\delta b|^2$ versus beam injection rate I_b shows that the mode is unstable for a threshold of $I_b \sim 18.5$ A. The theoretical scaling $|\delta b|^2 \sim (1 - I_{b,\text{threshold}}/I_b)$ [68] is shown in red.

keeping the shape of the distribution constant, leading to the observation of an instability threshold [28]. In this study, it is posited that fast-ion drive increases with beam density such that there is a critical value where fast-ion drive balances damping from other sources, leading to a beam density threshold.

This argument, given for CAEs in simulation, is applicable to other energetic ion driven AEs. Particularly, this experiment as designed should yield a similar beam density threshold because the slow injection rate ramp is expected to approximately produce a distribution that changes self-similarly over time (i.e. only by a scale factor).

The mode power scaling as seen in Fig. 5.10 is consistent with predictions for single mode collisional saturation near marginal stability [68], $|\delta b|^2 \sim (1 - \gamma_d/\gamma_L) \sim (1 - I_{b,\text{threshold}}/I_b)$, where γ_d is the growth rate from fast-ion drive and γ_L is the damping rate. A fit on the data was performed using a non-linear least squares fit to the function $y = A(1 - B/x)$, where $y = |\delta b|^2$ and $x = I_b$, and A (a scale factor) and $B = I_{b,\text{threshold}}$ were determined through the fit. This scaling is plotted over the data in Fig. 5.10 and is a reasonably good fit with correlation coefficient $R^2 = 0.54$. It is worth noting that there is a deviation from

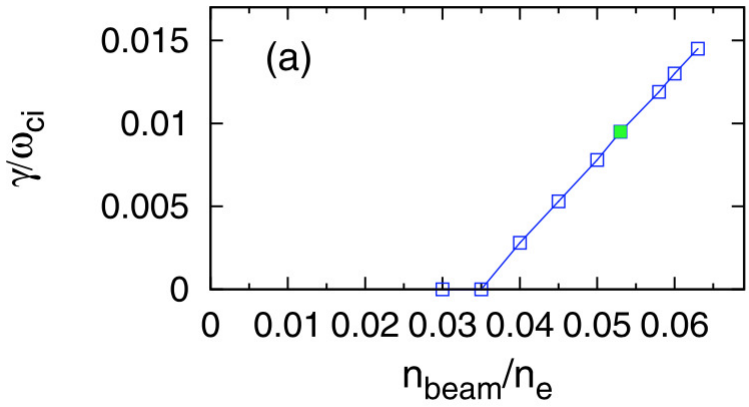

Figure 5.11: From Ref. [28], the growth rate γ of a CAE is shown versus the beam density.

the fit, as seen in Fig. 5.2(c) around $t \sim 2380 - 2450$ ms, corresponding to an injection rate of $I_b \sim 21 - 22.5$ A in Fig. 5.10. The reason for this issue in the monoticity of the scaling is unknown and constitutes future work; however, the overall scaling is still qualitatively consistent with the theory for single mode collisional saturation.

The observed beam injection rate threshold implies $\gamma_d/\gamma_L > 0.84$, indicating that the mode was near marginal stability during the entire beam ramp. Previous simulations of CAEs found a much stronger saturation scaling of $|\delta b|^2 \sim \gamma^4 \sim (I_b - I_{b,\text{threshold}})^4$ due to being in the collisionless regime and likely far from marginal stability [28].

In practice, transients in the fast-ion population after beam turn-on complicate this simple picture of the distribution evolving self-similarly. The remnant population of fast-ions (mentioned earlier, from a beam with different injection geometry) that existed before beam turn-on also affected the shape of the distribution. Nonetheless, the threshold, observed at the end of the beam ramp, is unlikely to be affected by these considerations, which occurred early in the ramp. Sawteeth are more likely to complicate this picture because the mode is at marginal stability; the mode amplitude modulation caused by sawteeth could have resulted from only minor changes in the distribution function or bulk plasma.

5.5. Comparison of AE frequency and amplitude with theoretical expectations

5.5.1. Orbit-averaged resonance condition

The fast-ion population was analyzed in order to determine the resonant particles and the source of mode drive. Existing theory predicts AEs in this sub-cyclotron frequency range are excited through Doppler-shifted cyclotron resonance with fast-ions [12]. Fast-ion drive comes from resonant ions that satisfy the orbit-averaged resonance equation [12]:

$$\omega - n\omega_\phi + p\omega_\theta - \ell\langle\omega_{ci}\rangle = 0 \tag{5.1}$$

where n is the toroidal mode number; ω_ϕ and ω_θ are the characteristic toroidal and poloidal orbit frequencies and are positive for passing ions moving in the beam direction; and $\langle\omega_{ci}\rangle$ is the orbit-averaged cyclotron frequency. $p = m + s$ where m is the poloidal mode number and s is the toroidicity-induced sideband number (or resonance order), and s, ℓ are integers, with $\ell = 0$ corresponding to direct resonance and $\ell = 1$ corresponding to Doppler-shifted cyclotron resonance.

5.5.2. Modeling codes

5.5.3. The ORB_GC code

The ORB_GC code [69] is used to calculate the characteristic poloidal and toroidal orbit frequencies. ORB_GC is a code that calculates orbit frequencies using a constants of motion (COM) approach. Given equilibrium, initial position, and velocity, a pitch ($\chi = v_\parallel/v$) is determined everywhere along major radius and vertical position (R, z) using conservation of energy (E), adiabatic moment (μ_0), and toroidal canonical angular momentum (P_ϕ), where [69]

$$\mu_0 = M_i v_\perp^2/2B = \frac{E}{B}(1 - \chi^2) \tag{5.2}$$

and

$$P_\phi = \psi - \frac{F v_\parallel}{\omega_{ci}} = \psi - \frac{F\chi}{ZeB}(2M_i E)^{1/2} \tag{5.3}$$

where $F = B_t R$. ORB_GC uses poloidal flux (ψ) and magnetic field (B) that are computed by the equilibrium fitting code (EFIT, described below) on the (R, z) grid. The pitch and energy, in combination with the spatial structure of the magnetic field, then give the information needed to calculate the curvature and gradient drift velocities. Finally, the total guiding center velocity including drifts is integrated for one poloidal transit, and this gives the toroidal and poloidal frequencies, ω_ϕ and ω_θ respectively. For this analysis, ORB_GC was modified to include a gyrophase integration, which then gives an orbit-averaged cyclotron frequency $\langle \omega_{ci} \rangle$.

5.5.4. The TRANSP code

The integrated transport modeling code TRANSP was used to model the evolution of the fast ion distribution as a function of pitch, energy, position, and time. TRANSP is a time-dependent equilibrium and transport solver for tokamak plasma discharges [70] first developed at the Princeton Plasma Physics Laboratory (PPPL) in the 1970s; it has since been continually advanced and is one of the primary codes used for both prediction and analysis of experimental tokamak data [71]. TRANSP can be used to calculate beam deposition, fast-ion orbits, charged particle collisions, charge exchange transport of beam particles, and beam-driven currents and momentum transfer [70] through Monte Carlo techniques, taking inputs from external measurements and from the equilibrium fitting code EFIT, described in the next section. The TRANSP code has been found to be reasonably accurate with comparisons for many kinds of problems from experimental data from various tokamaks. An example of the high level of agreement between TRANSP simulation and experimental measurements is shown in Fig. 5.12, which is taken from a 2000 study by R. V. Budny on local transport in the Joint European Tokamak (JET) [72] and shows a comparison of neutron emission rates from measurement and TRANSP simulation.

This analysis uses the NUBEAM [71] module in TRANSP to predict the fast-ion distribution everywhere in (R, z) space, and has multiple models for taking into account

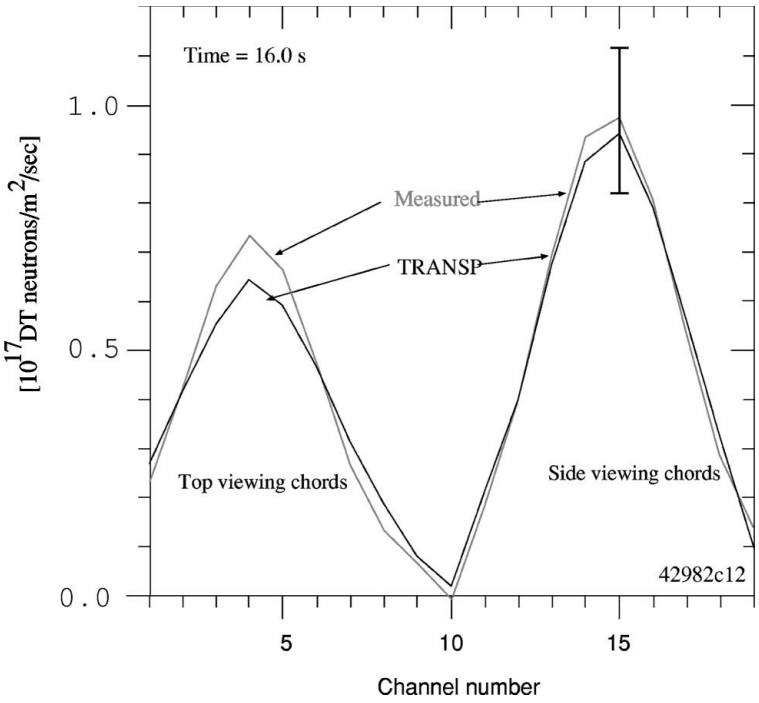

Figure 5.12: Neutron emission rates from measurement and from TRANSP simulation show good agreement in this study from Ref. [72].

the effect of sawtooth oscillations. NUBEAM is a Monte Carlo package for time-dependent NBI physics, evaluating the deposition, slowing down, and thermalization of fast ions in tokamaks. It includes NBI physics such as neutral beam deposition, fast-ion orbiting, power deposition, beam driven current, and momentum transfer, in addition to accounting for particle collisions, charge exchange, and beam particle transport [71]. In this analysis, NUBEAM used the full reconnection Kadomtsev model [63] for sawtooth oscillations, and assumed no anomalous fast ion diffusion otherwise. TRANSP and ORB_GC resonance analysis were managed via the OMFIT (One Modeling Framework for Integrated Tasks) [73] modeling framework. OMFIT is a modeling and data analysis software for magnetically confined fusion research experiments, and utilizes modules that cover a wide range of different physics areas. Some of these include equilibrium reconstruction, profiles analysis, gyrokinetic simulations, transport modeling, plasma heating, and stability analysis.

5.5.5. Equilibrium reconstruction via EFIT

5.5.5.1. The Grad-Shafranov equilibrium equation

The Grad-Shafranov equation is an equilibrium equation that is typically used to describe axisymmetric scenarios like tokamak equilibria. It is written as a differential equation for the poloidal flux function ψ mentioned earlier, using $p(\psi)$ and $f(\psi)$ as functions for plasma pressure and current flux. A detailed derivation may be found in Ref. [1], and the derivation for the Grad-Shafranov equation will be summarized briefly.

Beginning with the equilibrium equation:

$$\boldsymbol{J} \times \boldsymbol{B} = \nabla p \tag{1.2}$$

This equation can be written it in terms of the poloidal flux function ψ in cylindrical coordinates. Working in Ampère's law, we arrive at the Grad-Shafranov equation:

$$R\frac{\partial}{\partial R}\frac{1}{R}\frac{\partial \psi}{\partial R} + \frac{\partial^2 \psi}{\partial z^2} = -\mu_0 R^2 p'(\psi) - \mu_0^2 f(\psi) f'(\psi) \tag{5.4}$$

The Grad-Shafranov equation can be numerically solved for equilibrium reconstruction in tokamak plasmas. Equilibrium reconstruction can give valuable information such as location of flux surfaces, current density profiles, plasma pressure profiles, plasma geometry, and more.

5.5.5.2. The EFIT code

Equilibrium reconstruction of tokamaks is important in understanding quantitative measurements taken during experiment. The predecessors of the EFIT code [74, 75] used magnetic measurements from outside of the plasma to determine information like plasma geometry, stored plasma energy, and current profiles. These external magnetic measurements are from diagnostics such as the Motional Stark Effect (MSE) diagnostic [42], which measures the direction of magnetic field lines within the plasma, as well as other external diagnostics like magnetic probes and poloidal flux loops. Equilibrium

reconstruction is done by solving the Grad-Shafranov equilibrium equation [1], using measurements as constraints on the toroidal current density. EFIT builds on its predecessors by implementing a Picard linearization scheme for computational efficiency while allowing for a distributed plasma current source [76] within MHD equilibrium constraints. The analysis shown in this dissertation uses external magnetics data as well as MSE as constraints on equilibrium reconstruction.

5.5.6. The hybrid MHD code HYM

HYM is a hybrid MHD code that is used to model the effects of energetic beam ions on the equilibria of tokamak plasmas, and in particular the physics and properties of fast-ion driven Alfvén eigenmodes [22, 28]. It was first adapted for NSTX but has since also been adapted for use on DIII-D plasmas; the results of these simulations will be discussed later.

The HYM code is a 3-dimensional nonlinear global stability code in toroidal geometry [28]. It includes multiple fluid and kinetic models that can be combined to treat the components of a plasma. The combination used in simulations of NSTX and DIII-D treats the plasma as consisting of two components: first, the thermal background plasma is treated using a one-fluid MHD model; second, the energetic beam ions are treated with a kinetic Vlasov description [22, 28]. These are then coupled through a current coupling scheme, using the momentum equation for the thermal background plasma [28]:

$$\rho d\boldsymbol{V}/dt = -\nabla p + \mu_0(\boldsymbol{J} - \boldsymbol{J}_b) + \boldsymbol{B} - qn_b(\boldsymbol{E} - \eta\delta\boldsymbol{J}) + \nu\Delta\boldsymbol{V} \tag{5.5}$$

where ρ is the thermal plasma density, $\boldsymbol{V}$ is the thermal plasma velocity, p is the pressure, n_b is the beam ion density, $\boldsymbol{J}_b$ is the beam ion induced current, $\boldsymbol{B} = \boldsymbol{B}_0 + \delta\boldsymbol{B}$ is the total magnetic field, $\boldsymbol{E}$ is the perturbed electric field, $\boldsymbol{J} = \frac{1}{\mu_0}\nabla \times \boldsymbol{B}$ is the plasma current and $\delta\boldsymbol{J}$ is the perturbed plasma current, and ν is a viscosity coefficient. Quasineutrality is assumed ($n_e = n_b + n_i$). This momentum equation enters in with the rest of the fluid equations to describe the thermal plasma.

HYM implements a numerical model for simulation which assumes that the total energy in

the system, consisting of the sum of the thermal plasma energy and the beam energy, is conserved [19]:

$$E_{tot} = \int (2\mu_0 B^2 + \frac{p}{\gamma - 1} + \rho\frac{V^2}{2})d^3\boldsymbol{x} + \int m_i \frac{v^2}{2} F d^3\boldsymbol{v} d^3\boldsymbol{x} \tag{5.6}$$

where F is the beam ion distribution function.

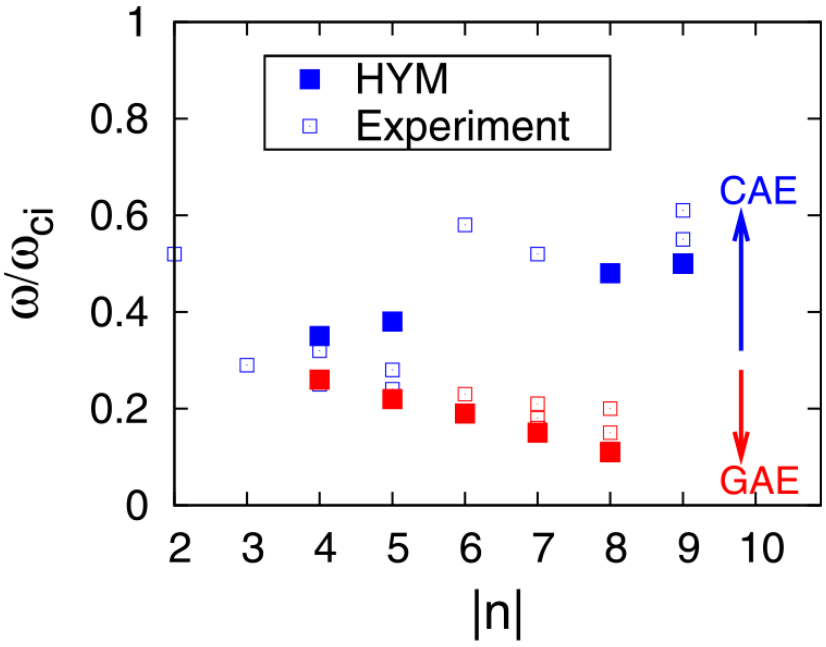

Figure 5.13: Taken from Ref.[28]. Frequency versus toroidal mode number for GAEs (red) and CAEs (blue) from experimental measurements and HYM simulations.

The beam ions are modeled using the full-orbit equations of motion and a particle-in-cell (PIC) simulation method in conjunction with the delta-f method [77]. The delta-f method, described in detail in Ref. [77], essentially evolves the perturbed beam ion distribution function F along a set of characteristics that solve the full-orbit equations; it is used in the HYM code to reduce numerical noise. This method requires the equilibrium distribution function of the beam ions to be known, and the perturbed distribution function $\delta F = F - F_0$ is then integrated along particle trajectories from the full-orbit equations of motion. The equilibrium distribution function F is chosen to account for parameters like the injection velocity and pitch-angle distribution of the beam, the plasma flux, and

prompt-loss boundaries [28]. In particular HYM can take the beam ion density, magnetic field, and plasma profiles from TRANSP modeling. HYM simulations have been extensively run on experimental data for NSTX and NSTX-U, yielding detailed measurements of CAE/GAE amplitudes and mode structures over different ranges of toroidal and poloidal mode numbers. Figure. 5.13 shows the results from a 2017 study of CAEs and GAEs on NSTX, found in Ref. [28], from both experimental measurements and from HYM numerical simulations. It can be seen that there is reasonably good agreement between experimental observations and HYM.

5.6. Analysis of fast-ion population with TRANSP

The fast-ion population was modeled via TRANSP simulation, using the NUBEAM module to predict the physics of NBI during the discharge. Fast-ion density is shown in Fig. 5.14, averaged over $\rho_{\text{eff}} < 0.3$ where ρ_{eff} is the normalized effective plasma radius based on toroidal flux described earlier. This value is chosen to indicate the region over which the q-profile is flat. The fast-ion density in this figure is plotted versus pitch ($v_{\|}/v$) and energy for times before beam turn-on, shown in Fig. 5.14(a), and after mode onset, shown in Fig. 5.14(b).

As mentioned in Chapter 2, CAE/GAEs are driven by resonant fast-ions in an anisotropic population, with CAE/GAE drive (γ_{EP}) approximated as an integral over the velocity space gradients of the distribution, assuming large anisotropy:

$$\gamma_{\text{EP}} \propto - n_{\text{EP}} \int h\left(\chi, v\right) \frac{\partial f_{\text{EP}}(\chi, v)}{\partial \chi} d\chi \Big|_{v_{b\|} = v_{\|,\text{res}}} \tag{5.7}$$

where $\chi = v_{\|}/v$ is the pitch. From this equation it is clear that CAE/GAE drive γ_{EP} is dependent on the sign of the gradient of the fast-ion population with respect to pitch ($\partial f_{\text{EP}}/\partial \chi$) at the location of resonance.

Before beam turn-on, in Fig. 5.14(a), the resonance lines drawn show that the resonances for $p = 0, 5$ intersect a region at pitch of $v_{\|}/v \sim 0.65$ and energy of ~ 45 keV where

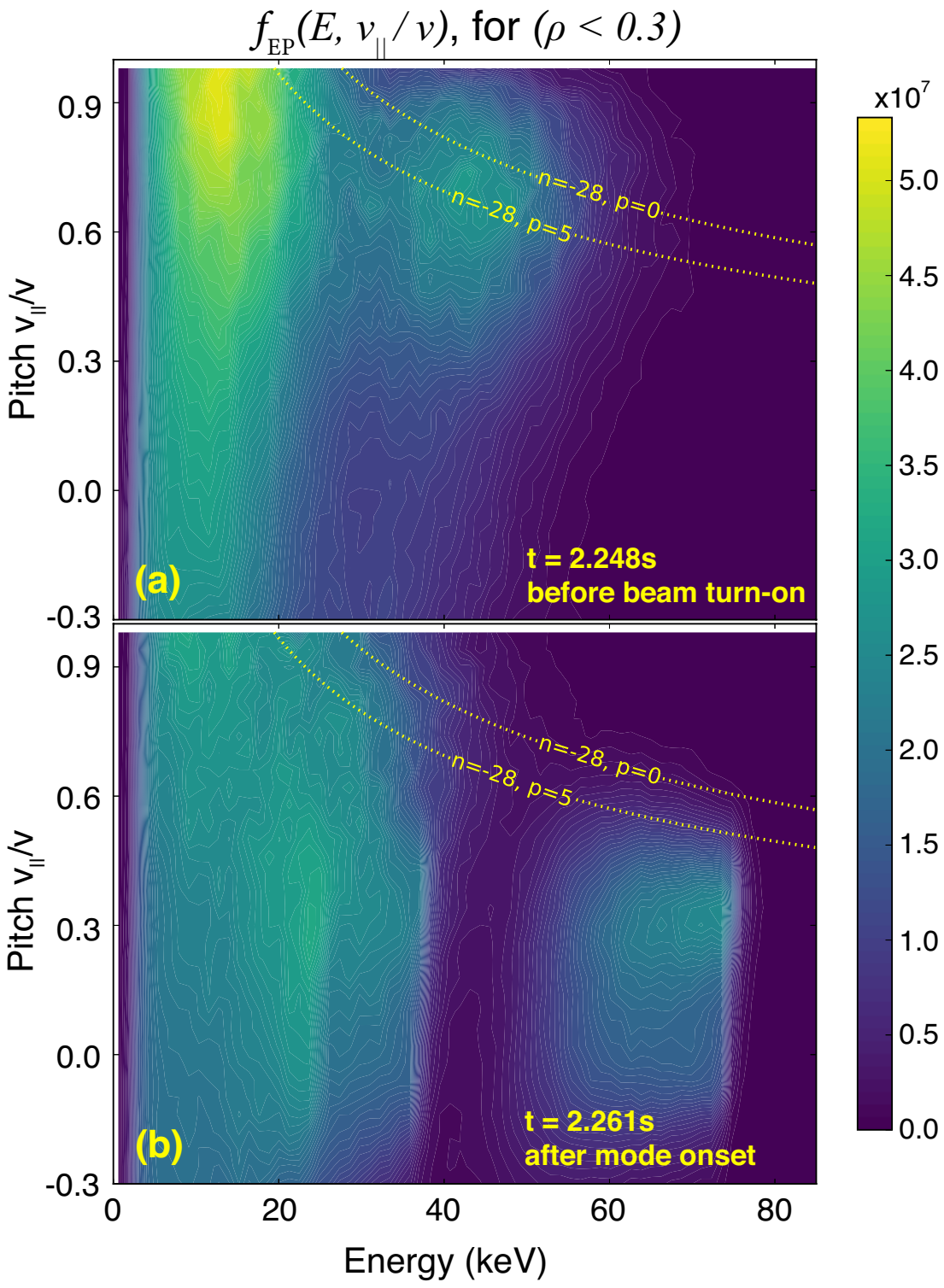

Figure 5.14: Fast-ion density as a function of pitch $v_{\|}/v$ and energy in keV, for times (a) before beam turn-on and (b) after mode onset, averaged over $\rho < 0.3$. The resonance lines for $n = -28, p = 0, 5$ are plotted.

$\partial f_{\rm EP}/\partial\chi > 0$; because of this, the mode would be damped by the fast-ions as $\gamma_{\rm EP} < 0$. In comparison, after beam turn-on and mode onset, the resonance lines pass through a region at $v_\parallel/v \sim 0.3$ and high energy of $\sim 60 - 75$ keV with $\partial f_{\rm EP}/\partial\chi < 0$, leading to drive from the fast-ions. In this figure, $p = 0$ corresponds to $s = 0$ for the observed frequency as calculated from the finite-frequency corrected dispersion relations discussed in Chapter 2 and derived in Ref. [11].

5.7. Identification of a GAE

The mode shown in Fig. 5.2 is identified as a GAE from analysis of the fast-ion population in Fig. 5.14(b) and considerations of the dispersion relations and the DCR resonance equation, $\omega_{ci} \approx \omega - k_\parallel v_\parallel$, which is an $\ell = 1$ approximation of the orbit-averaged resonance equation (Eq. 5.1) as stated earlier:

$$\omega - n\omega_\phi + p\omega_\theta - \ell\langle\omega_{ci}\rangle = 0 \tag{5.1}$$

First, it will be shown that this mode is implausible to be a CAE. From the dispersion relations, discussed in Chapter 2, it is clear that CAEs must have parallel phase velocity of $\omega/k_\parallel > v_A$, while GAEs must have $\omega/k_\parallel < v_A$. The fast-ion population in Fig. 5.14(b) shows that the resonant subset of particles peaks at high energy, $\sim 60 - 75$ keV, for a pitch of $v_\parallel/v \sim 0.3$. It is also clear that there are little to no particles above a pitch of $v_\parallel/v \sim 0.7$. The frequency of the mode ($f \sim 5520$ kHz) in conjunction with the beam energy ($60 - 75$ keV) indicate that the only particles present are sub-Alfvénic, with $v_0/v_A \leq 0.8$ where v_0 is the injection velocity calculated from the beam energy.

Referencing the orbit-averaged resonance equation (Eq. 5.1) above, the $\ell = 0$ resonance requires super-Alfvénic particles ($v_\parallel/v_A > 1$) for CAEs without large sideband resonances ($s \gg 1$). As discussed earlier, mode resonances are implausible for large s because strong wave-particle interactions require a small s [27]. Precluding the $\ell = 0$ resonance for CAEs, we consider the $\ell = 1$ resonance, which at this frequency corresponds to $v_\parallel/v_A = 0.9$. Since the only particles present have $v_0/v_A \leq 0.8$, it is clear that an $\ell = 0$ resonance for CAEs also cannot be satisfied without a large toroidal sideband number s. Therefore, we can

conclude that this mode is highly unlikely to be a CAE.

On the other hand, analysis of this mode shows that it is likely a GAE. As discussed earlier, GAEs are typically core-localized [13, 19] and form at a minimum in the q-profile. Because this plasma features a peaked density profile with $q \sim 1$ for $\rho < 0.3$, this indicates that the location of the mode is near the magnetic axis.

Again considering the DCR resonance equation $\omega_{ci} \approx \omega - k_{\|} v_{\|}$, the lowest possible $\omega/k_{\|}$ occurs for passing particles at $k_{\perp} \sim 0$; any non-zero $k_{\perp}$ pushes the resonance lines to the higher pitch region in Fig. 5.14(b) in the fast-ion distribution where there are less particles. Since $k_{\perp} \sim 0$ is the most plausible resonance, the data is consistent with an $m = 0$ mode to minimize $k_{\perp}$.

From the dispersion relation for GAEs [11], an $m = 0$ mode at this frequency has toroidal mode number of $|n| = 28$. In this convention, a positive toroidal mode number indicates a co-propagating mode (in the direction of plasma current), while a negative toroidal mode number indicates a counter-propagating mode. Again referencing the orbit-averaged resonance equation (Eq. 5.1), it is clear that a $n = +28$ mode satisfying this equation for Doppler-shifted cyclotron resonance ($\ell = 1$) requires an implausible large toroidal sideband number s. Direct resonance ($\ell = 0$) requires even larger values of s. We can therefore rule out $n = +28$, and the resonance line for $n = -28, p = 0$ is shown in Fig. 5.14(b) to pass through the region of the fast-ion population with the high energy peak at 60-75 keV where $\partial f_{\mathrm{EP}}/\partial \chi < 0$ leading to fast-ion drive. The $n = -28, p = 5$ line shows that a relatively small sideband number moves the resonance lines closer to the peak. These considerations show that the mode is most likely a GAE.

5.8. Comparison with analytic theory

The results presented here are consistent with predictions from analytic theory and simulations of GAE excitation and suppression in NSTX/NSTX-U. A 2017 study of GAEs (Ref. [78]) found that counter-propagating GAEs were the most unstable modes on NSTX, driven by high pitch-angle fast-ions in the distribution, supported by simulation and

experimental measurements. Similarly, a 2019 study (Ref. [19]) on simulations of GAEs in NSTX-U found that unstable counter-propagating GAEs were suppressed through neutral beam injection from a beam source with large tangency radius, confirming experimental results.

The beam density threshold presented in 5.1 can be explained through consideration of Eq. 5.7, which is derived from analytic theory of DCR CAE/GAEs. As the beam density n_{EP} is slowly ramped down over time, the partial derivative of the fast-ion distribution with respect to pitch $\partial f_{\mathrm{EP}}/\partial\chi$ is not expected to change significantly; therefore, the fast-ion drive γ_{EP} decreases in time as n_{EP} decreases. At a certain point, the fast-ion drive is no longer large enough to overcome the mode damping from the thermal plasma, and the mode then rapidly decays.

Quantitative predictions from analytic theory [11] also agree well with experimental measurements. Analytic theory predicts GAEs to be driven unstable by a neutral beam distribution with normalized injection velocity $v_0/v_A = 0.8$ and peak $v_\parallel/v \approx 0.3$ when $0.5 < f/f_{ci} < 0.8$, as shown in Fig. 5.15. This theory takes into account finite frequency corrections, which are required for accuracy in analysis of modes at frequencies at a large fraction of f_{ci}. The observed frequency of the mode of interest in the lab frame is $f/f_{ci} = 0.58$; taking into account the plasma rotation, the observed frequency in the plasma frame is $f = f_{\mathrm{measured}} + nf_{\mathrm{ROT}}$, where f_{ROT} is the plasma rotation frequency, and is estimated from charge-exchange recombination spectroscopy (CER) to be $f_{\mathrm{ROT}} = 7$ kHz. This frequency falls comfortably within the frequency range predicted from quantitative analytic theory calculations.

The identification of this mode as a GAE is also consistent with analytic theory and simulation. Fast-ion drive for $\ell = 1$ GAEs is predicted to be the largest for modes with $k_\parallel \gg k_\perp$ [11], which reinforces the argument made in favor of the mode having a poloidal mode number of $m = 0$. Additionally, the HYM code [28], described earlier, was used to model a repeat DIII-D discharge (#172019). The simulations searched for unstable modes within a broad range of toroidal mode numbers and found unstable counter-propagating GAEs with $f \geq f_{ci}$ for mode numbers $n = -22, -23, -24, -25$. It also found that GAEs

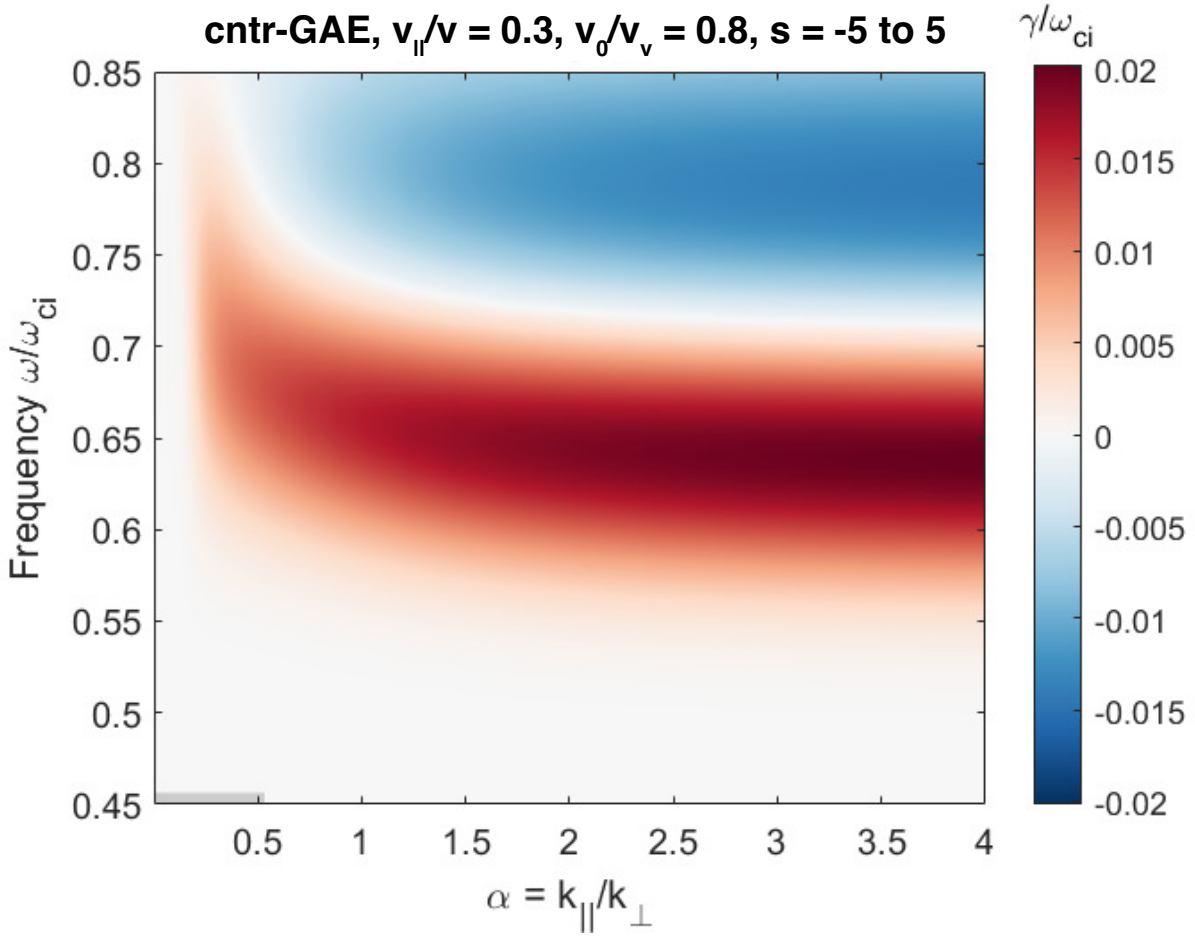

Figure 5.15: Predictions from analytic theory showing counter-propagating GAEs driven unstable by NBI with normalized injection velocity $v_0/v_A = 0.8$ and $v_\parallel/v \approx 0.3$ at frequencies of $0.5 < f/f_{ci} < 0.8$

.

were the most unstable mode for all toroidal harmonics, and that a wide range of toroidicity-induced sideband number ($\Delta p \sim 10$) had significant effects to mode drive. The HYM code is believed to overestimate frequencies and underestimate toroidal mode numbers for unstable modes with significant f/f_{ci} because it uses a one-fluid MHD model for the background thermal plasma; two-fluid corrections to HYM simulations give smaller frequencies and higher values of toroidal mode numbers [79].

CHAPTER 6

Summary and Conclusions

6.1. Review of results

The focus of this dissertation was to study compressional (CAE) and global (GAE) Alfvén eigenmode activity in DIII-D and how the spectral characteristics and stability of these modes depend on plasma parameters. For this study, magnetic fluctuation measurements were obtained via the Ion Cyclotron Emission (ICE) diagnostic. DIII-D features neutral beam injection (NBI) that have the capability to independently vary beam energy and current; this capability was used in a unique manner to explore a wide parameter space for the experiment to determine stability thresholds for mode excitation.

The major result presented in this thesis is the controlled stabilization of one of these high frequency AEs, excited through Doppler-shifted cyclotron resonance (DCR) with fast-ions from NBI. This was achieved during a 1.28 T discharge where the energy of one of the off-axis neutral beams was kept constant while the injection rate was ramped down. This marks the first time a controlled energetic ion density ramp has stabilized a fast-ion driven Alfvén wave. Moreover, the scaling of mode power with beam injection rate was found to be consistent with theoretical expectations for collisional saturation near marginal stability.

The fast-ion population was analyzed through modeling codes like TRANSP and ORB_GC, allowing the identification of the resonant energetic particles in the population that were likely responsible for driving the mode. Through this analysis, as well as considerations from dispersion relations and resonance equations, this mode is identified as a shear-polarized GAE, which is the first identification of a GAE excited by sub-Alfvénic

fast-ions in a fusion research plasma.

6.2. Diagnostic development

For the analysis presented here, the ICE diagnostic was utilized for magnetic fluctuation measurements. Unfortunately, a toroidal mode number measurement was unable to be reliably obtained due to an unknown path length difference between the two toroidal loops comprising the ICE diagnostic system utilized for this experiment. Since the time of this experiment, the ICE system has been updated such that the current path length differences on the diagnostic are well-documented.

Future studies of fast-ion driven modes within the bandwidth of the ICE diagnostic (between $1 - 100$ MHz) should be able to obtain reliable toroidal mode number measurements, allowing for a more direct comparison with analytic theory and simulations and a significant improvement in resonance analysis.

6.3. Future work

In addition to toroidal mode number measurements in future experiments, there are many aspects of this experiment that can still be explored. The results presented at the end of Chapter 4 comprise of many interesting observations that can be analyzed. These include the observation of a toroidal magnetic field B_t threshold, an electron density n_e threshold, the scaling of mode frequency with v_A, and possible stability thresholds from other injecting beams. Understanding these different aspects of AE excitation is essential in furthering the physics knowledge of wave-particle interaction and the interplay between wave drive and damping. With the improvements on the ICE diagnostic, the modes can be characterized over a wider parameter space as intended in the experimental design.

Bibliography

[1] John Wesson. *Tokamaks*. 4th. Oxford University Press, 2011. ISBN: 978-0-19-959223-4.

[2] C. W. Hartman et al. "A conceptual fusion reactor based on the high-plasma-density Z-pinch". In: *Nuclear Fusion* 17.5 (Oct. 1977), pp. 909–918. ISSN: 0029-5515. DOI: 10.1088/0029-5515/17/5/004.

[3] Lyman Spitzer. "The Stellarator Concept". In: *The Physics of Fluids* 1.4 (July 1958), pp. 253–264. ISSN: 0031-9171. DOI: 10.1063/1.1705883.

[4] Linjin Zheng. *Advanced Tokamak Stability Theory*. Morgan & Claypool Publishers, 2015. ISBN: 978-1-62705-423-2. DOI: 10.1088/978-1-6270-5423-2. URL: http://iopscience.iop.org/book/978-1-6270-5423-2.

[5] I. T. Chapman. "Controlling sawtooth oscillations in tokamak plasmas". In: *Plasma Physics and Controlled Fusion* 53.1 (Nov. 2010), p. 013001. ISSN: 0741-3335. DOI: 10.1088/0741-3335/53/1/013001.

[6] M. E. Austin and J. Lohr. "Electron cyclotron emission radiometer upgrade on the DIII-D tokamak". In: *Review of Scientific Instruments* 74.3 (Mar. 2003), pp. 1457–1459. ISSN: 0034-6748. DOI: 10.1063/1.1530387.

[7] D. Stutman et al. "Correlation between Electron Transport and Shear Alfvén Activity in the National Spherical Torus Experiment". In: *Physical Review Letters* 102.11 (Mar. 2009), p. 115002. DOI: 10.1103/PhysRevLett.102.115002.

[8] Ellen G. Zweibel. "The basis for cosmic ray feedback: Written on the wind". In: *Physics of Plasmas* 24.5 (May 2017), p. 055402. ISSN: 1070-664X. DOI: 10.1063/1.4984017.

[9] B. Eliasson and K. Papadopoulos. "Pitch angle scattering of relativistic electrons near electromagnetic ion cyclotron resonances in diverging magnetic fields". In: *Plasma Physics and Controlled Fusion* 59.10 (Sept. 2017), p. 104003. ISSN: 0741-3335. DOI: 10.1088/1361-6587/aa8100.

[10] W. W. Heidbrink. "Basic physics of Alfvén instabilities driven by energetic particles in toroidally confined plasmas". In: *Physics of Plasmas* 15.5 (May 2008), p. 055501. ISSN: 1070-664X, 1089-7674. DOI: 10.1063/1.2838239.

[11] J. B. Lestz et al. "Analytic stability boundaries for compressional and global Alfvén eigenmodes driven by fast ions. I. Interaction via ordinary and anomalous cyclotron resonances". In: *Physics of Plasmas* 27.2 (2020), p. 022513. DOI: 10.1063/1.5127551. URL: https://doi.org/10.1063/1.5127551.

[12] N. N. Gorelenkov and C. Z. Cheng. "Alfvén cyclotron instability and ion cyclotron emission". In: *Nuclear Fusion* 35.12 (1995), p. 1743. ISSN: 0029-5515. DOI: 10.1088/0029-5515/35/12/I39.

[13] N. N. Gorelenkov et al. "Theory and observations of high frequency Alfvén eigenmodes in low aspect ratio plasmas". In: *Nuclear Fusion* 43.4 (Mar. 2003), pp. 228–233. ISSN: 0029-5515. DOI: 10.1088/0029-5515/43/4/302.

[14] J. B. Lestz. "Theory and Simulations of Compressional and Global Alfvén Eigenmode Stability in Spherical Tokamaks". In: *arXiv:2005.11013 [physics]* (May 2020). arXiv: 2005.11013. URL: http://arxiv.org/abs/2005.11013.

[15] M. V. Gorelenkova et al. "Kinetic theory of plasma adiabatic major radius compression in tokamaks". In: *Physics of Plasmas* 5.5 (Apr. 1998), pp. 1345–1353. ISSN: 1070-664X. DOI: 10.1063/1.872794.

[16] Ya. I. Kolesnichenko et al. "Localized fast magnetoacoustic eigenmodes in tokamak plasmas". In: *Nuclear Fusion* 38.12 (Dec. 1998), pp. 1871–1879. ISSN: 0029-5515. DOI: 10.1088/0029-5515/38/12/311.

[17] W. W. Heidbrink et al. "An investigation of beam driven Alfvén instabilities in the DIII-D tokamak". In: *Nuclear Fusion* 31.9 (Sept. 1991), pp. 1635–1648. ISSN: 0029-5515. DOI: 10.1088/0029-5515/31/9/002.

[18] N. N. Gorelenkov et al. "Beam ion driven instabilities in the National Spherical Tokamak Experiment". In: *Physics of Plasmas* 11.5 (Apr. 2004), pp. 2586–2593. ISSN: 1070-664X. DOI: 10.1063/1.1689667.

[19] E. V. Belova et al. “Numerical simulations of global Alfvén eigenmodes excitation and stabilization in NSTX-U”. In: *Physics of Plasmas* 26.9 (Sept. 2019), p. 092507. ISSN: 1070-664X. DOI: 10.1063/1.5116357.

[20] N. A. Crocker et al. “High spatial sampling global mode structure measurements via multichannel reflectometry in NSTX”. In: *Plasma Physics and Controlled Fusion* 53.10 (Aug. 2011), p. 105001. ISSN: 0741-3335. DOI: 10.1088/0741-3335/53/10/105001.

[21] N. A. Crocker et al. “Internal amplitude, structure and identification of compressional and global Alfvén eigenmodes in NSTX”. In: *Nuclear Fusion* 53.4 (2013), p. 043017. ISSN: 0029-5515. DOI: 10.1088/0029-5515/53/4/043017.

[22] E. V. Belova, N. N. Gorelenkov, and C. Z. Cheng. “Self-consistent equilibrium model of low aspect-ratio toroidal plasma with energetic beam ions”. In: *Physics of Plasmas* 10.8 (July 2003), pp. 3240–3251. ISSN: 1070-664X. DOI: 10.1063/1.1592155.

[23] G. Y. Fu and J. W. Van Dam. “Stability of the global Alfvén eigenmode in the presence of fusion alpha particles in an ignited tokamak plasma”. In: *Physics of Fluids B: Plasma Physics* 1.12 (Dec. 1989), pp. 2404–2413. ISSN: 0899-8221. DOI: 10.1063/1.859175.

[24] Yang Zhang et al. “Observation of fast-ion Doppler-shifted cyclotron resonance with shear Alfvén waves”. In: *Physics of Plasmas* 15.10 (Oct. 2008), p. 102112. ISSN: 1070-664X. DOI: 10.1063/1.2996323.

[25] W. W. Heidbrink et al. “Observation of compressional Alfvén eigenmodes (CAE) in a conventional tokamak”. In: *Nuclear Fusion* 46.2 (2006), p. 324. ISSN: 0029-5515. DOI: 10.1088/0029-5515/46/2/016.

[26] N N Gorelenkov. “Energetic particle-driven compressional Alfvén eigenmodes and prospects for ion cyclotron emission studies in fusion plasmas”. In: *New Journal of Physics* 18.10 (Oct. 2016), p. 105010. ISSN: 1367-2630. DOI: 10.1088/1367-2630/18/10/105010.

[27] R. Nazikian et al. “Excitation of Alfvén eigenmodes by low energy beam ions in the DIII-D and JET tokamaks”. In: *Physics of Plasmas* 15.5 (May 2008), p. 056107. ISSN: 1070-664X, 1089-7674. DOI: 10.1063/1.2839286.

[28] E. V. Belova et al. “Nonlinear simulations of beam-driven compressional Alfvén eigenmodes in NSTX”. In: *Physics of Plasmas* 24.4 (Mar. 2017), p. 042505. ISSN: 1070-664X. DOI: 10.1063/1.4979278.

[29] E. V. Belova et al. “Coupling of Neutral-Beam-Driven Compressional Alfvén Eigenmodes to Kinetic Alfvén Waves in NSTX Tokamak and Energy Channeling”. In: *Physical Review Letters* 115.1 (June 2015), p. 015001. DOI: 10.1103/PhysRevLett.115.015001.

[30] H. L. Berk et al. “Continuum damping of low-n toroidicity-induced shear Alfvén eigenmodes”. In: *Physics of Fluids B: Plasma Physics* 4.7 (July 1992), pp. 1806–1835. ISSN: 0899-8221. DOI: 10.1063/1.860455.

[31] James W. van Dam, Guo-Yong Fu, and C. Z. Cheng. “Thermonuclear Instability of Global-Type Shear Alfvén Modes”. In: *Fusion Technology* 18.3 (Nov. 1990), pp. 461–474. ISSN: 0748-1896. DOI: 10.13182/FST90-A29282.

[32] Francis F. Chen. *Introduction to Plasma Physics and Controlled Fusion*. Springer, Dec. 2015. ISBN: 978-3-319-22309-4.

[33] R. W. Short and A. Simon. “Landau damping and transit-time damping of localized plasma waves in general geometries”. In: *Physics of Plasmas* 5.12 (Dec. 1998), pp. 4124–4133. ISSN: 1070-664X, 1089-7674. DOI: 10.1063/1.873146.

[34] T. H. Stix. “Fast-wave heating of a two-component plasma”. In: *Nuclear Fusion* 15.5 (Oct. 1975), pp. 737–754. ISSN: 0029-5515. DOI: 10.1088/0029-5515/15/5/003.

[35] J. L. Luxon and L. G. Davis. “Big Dee - A Flexible Facility Operating Near Breakeven Conditions”. In: *Fusion Technology* 8.1P2A (July 1985), pp. 441–449. ISSN: 0748-1896. DOI: 10.13182/FST85-A40083.

[36] J. L. Luxon. "A Brief Introduction to the DIII-D Tokamak". In: *Fusion Science and Technology* 48.2 (Oct. 2005), pp. 828–833. ISSN: 1536-1055. DOI: 10.13182/FST05-A1042.

[37] J. L. Luxon. "A design retrospective of the DIII-D tokamak". In: *Nuclear Fusion* 42.5 (2002), p. 614. ISSN: 0029-5515. DOI: 10.1088/0029-5515/42/5/313.

[38] D. C. Pace et al. "Dynamic neutral beam current and voltage control to improve beam efficacy in tokamaks". In: *Physics of Plasmas* 25.5 (Apr. 2018), p. 056109. ISSN: 1070-664X. DOI: 10.1063/1.5016160.

[39] C. J. Pawley et al. "Advanced control of neutral beam injected power in DIII-D". In: *Fusion Engineering and Design*. Proceedings of the 29th Symposium on Fusion Technology (SOFT-29) Prague, Czech Republic, September 5-9, 2016 123 (Nov. 2017), pp. 453–457. ISSN: 0920-3796. DOI: 10.1016/j.fusengdes.2017.02.106.

[40] Raymond Seraydarian and Keith Burrell. "Multichordal charge-exchange recombination spectroscopy on the DIII-D tokamak". In: *Review of Scientific Instruments* 57 (Sept. 1986), pp. 2012–2014. DOI: 10.1063/1.1138774.

[41] D. Wróblewski and L. L. Lao. "Polarimetry of motional Stark effect and determination of current profiles in DIII-D (invited)". In: *Review of Scientific Instruments* 63.10 (Oct. 1992), pp. 5140–5147. ISSN: 0034-6748. DOI: 10.1063/1.1143463.

[42] B. W. Rice, D. G. Nilson, and D. Wróblewski. "Motional Stark effect upgrades on DIII-D". In: *Review of Scientific Instruments* 66.1 (Jan. 1995), pp. 373–375. ISSN: 0034-6748. DOI: 10.1063/1.1146416.

[43] Henry Chiu. "Measurement of Neutral Beam Profiles at DIII-D". In: *Fusion Technology* 34.3P2 (Nov. 1998), pp. 564–567. ISSN: 0748-1896. DOI: 10.13182/FST98-A11963673.

[44] K. E. Thome et al. "Radio frequency measurements of energetic-particle-driven emission using the ion cyclotron emission diagnostic on the DIII-D tokamak". In:

Review of Scientific Instruments 89.10 (July 2018), p. 10I102. ISSN: 0034-6748. DOI: 10.1063/1.5035561.

[45] P. Helander, R. J. Akers, and L.-G. Eriksson. "On neutral-beam injection counter to the plasma current". In: *Physics of Plasmas* 12.11 (Nov. 2005), p. 112503. ISSN: 1070-664X. DOI: 10.1063/1.2121287.

[46] W. W. Heidbrink et al. "Initial measurements of the DIII-D off-axis neutral beams". In: *Nuclear Fusion* 52.9 (Sept. 2012), p. 094005. ISSN: 0029-5515. DOI: 10.1088/0029-5515/52/9/094005.

[47] C. J. Murphy et al. "Overview of DIII-D off-axis neutral beam project". In: *2011 IEEE/NPSS 24th Symposium on Fusion Engineering*. June 2011, pp. 1–6. DOI: 10.1109/SOFE.2011.6052323.

[48] M. D. Boyer et al. "Feedback control of stored energy and rotation with variable beam energy and perveance on DIII-D". In: *Nuclear Fusion* 59.7 (May 2019), p. 076004. ISSN: 0029-5515. DOI: 10.1088/1741-4326/ab17f5.

[49] David A. Homfray et al. "Real time neutral beam power control on MAST". In: *Fusion Engineering and Design*. Proceedings of the 26th Symposium of Fusion Technology (SOFT-26) 86.6 (Oct. 2011), pp. 780–784. ISSN: 0920-3796. DOI: 10.1016/j.fusengdes.2011.01.124.

[50] Reinhard Uhlemann and Jef Ongena. "Variation of Injected Neutral Beam Power at Constant Particle Energy by Changing the Beam Target Aperture of the TEXTOR Neutral Beam Injectors". In: *Fusion Technology* 35.1 (Jan. 1999), pp. 42–53. ISSN: 0748-1896. DOI: 10.13182/FST99-A76.

[51] J. Rauch et al. "Upgrade to DIII-D National Fusion Facility PCS and Neutral Beam Systems: In-Shot Variation of Neutral Beam Particle Energy". In: *Fusion Science and Technology* 72.3 (Oct. 2017), pp. 500–504. ISSN: 1536-1055. DOI: 10.1080/15361055.2017.1333845.

[52] B. G. Penaflor et al. “Latest advancements in DIII-D Plasma Control software and hardware”. In: *2013 IEEE 25th Symposium on Fusion Engineering, SOFE 2013*. Dec. 2013, p. 6635496. DOI: 10.1109/SOFE.2013.6635496. URL: https://collaborate.princeton.edu/en/publications/latest-advancements-in-diii-d-plasma-control-software-and-hardwar.

[53] F. Glass et al. “Upgraded divertor Thomson scattering system on DIII-D”. In: *Review of Scientific Instruments* 87.11 (Nov. 2016), 11E508. ISSN: 0034-6748. DOI: 10.1063/1.4955281.

[54] T. N. Carlstrom, D. R. Ahlgren, and J. Crosbie. “Real-time, vibration-compensated CO2 interferometer operation on the DIII-D tokamak”. In: *Review of Scientific Instruments* 59.7 (July 1988), pp. 1063–1066. ISSN: 0034-6748. DOI: 10.1063/1.1139726.

[55] R. K. Fisher et al. “Scintillator-based diagnostic for fast ion loss measurements on DIII-D”. In: *Review of Scientific Instruments* 81.10 (Oct. 2010), p. 10D307. ISSN: 0034-6748. DOI: 10.1063/1.3490020.

[56] W. W. Heidbrink. “Fast-ion D-alpha measurements of the fast-ion distribution”. In: *Rev. Sci. Instrum.* (2010), p. 8.

[57] C. M. Muscatello et al. “Extended fast-ion D-alpha diagnostic on DIII-D”. In: *Review of Scientific Instruments* 81.10 (Oct. 2010), p. 10D316. ISSN: 0034-6748. DOI: 10.1063/1.3475367.

[58] George Watson and W. W. Heidbrink. “Density interferometer using the fast Alfvén wave”. In: *Review of Scientific Instruments* 74.3 (Mar. 2003), pp. 1605–1608. ISSN: 0034-6748. DOI: 10.1063/1.1527222.

[59] W. W. Heidbrink et al. “Characterization of off-axis fishbones”. In: *Plasma Physics and Controlled Fusion* 53.8 (July 2011), p. 085028. ISSN: 0741-3335. DOI: 10.1088/0741-3335/53/8/085028.

[60] S. X. Tang et al. “Stabilization of Alfvén Eigenmodes in DIII-D via Controlled Energetic Ion Density Ramp and Validation of Theory and Simulations”. In: *Physical Review Letters* 126.15 (Apr. 2021), p. 155001. DOI: 10.1103/PhysRevLett.126.155001.

[61] B. A. Grierson et al. “Orchestrating TRANSP Simulations for Interpretative and Predictive Tokamak Modeling with OMFIT”. In: *Fusion Science and Technology* 74.1-2 (Aug. 2018), pp. 101–115. ISSN: 1536-1055. DOI: 10.1080/15361055.2017.1398585.

[62] Francesca Poli et al. *TRANSP v18.2*. [Computer Software] https://dx.doi.org/10.11578/dc.20180627.4. Oct. 2018. URL: https://dx.doi.org/10.11578/dc.20180627.4.

[63] B. B. Kadomtsev. “Tokamaks and dimensional analysis”. In: *Sov. J. Plasma Phys. (Engl. Transl.); (United States)* 1:4 (Jan. 1975). URL: https://www.osti.gov/biblio/7346587.

[64] J. A. Wesson. “Sawtooth oscillations”. In: *Plasma Physics and Controlled Fusion* 28.1A (Jan. 1986), pp. 243–248. ISSN: 0741-3335. DOI: 10.1088/0741-3335/28/1A/022.

[65] K. M. Ferrière, C. Zimmer, and M. Blanc. “Quasi-interchange modes and interchange instability in rotating magnetospheres”. In: *Journal of Geophysical Research: Space Physics* 106.A1 (2001), pp. 327–343. ISSN: 2156-2202. DOI: 10.1029/2000JA000133.

[66] F. Porcelli, D. Boucher, and M. N. Rosenbluth. “Model for the sawtooth period and amplitude”. In: *Plasma Physics and Controlled Fusion* 38.12 (Dec. 1996), pp. 2163–2186. ISSN: 0741-3335. DOI: 10.1088/0741-3335/38/12/010.

[67] G. J. Kramer et al. “Magnetic safety factor profile before and after sawtooth crashes investigated with toroidicity and ellipticity induced Alfvén eigenmodes”. In: *Nuclear Fusion* 41.9 (Sept. 2001), pp. 1135–1151. ISSN: 0029-5515. DOI: 10.1088/0029-5515/41/9/302.

[68] H. L. Berk, B. N. Breizman, and M. Pekker. "Nonlinear Dynamics of a Driven Mode near Marginal Stability". In: *Phys. Rev. Lett.* 76 (8 Feb. 1996), pp. 1256–1259. DOI: 10.1103/PhysRevLett.76.1256. URL: https://link.aps.org/doi/10.1103/PhysRevLett.76.1256.

[69] M. A. Van Zeeland et al. "Measurements and modeling of Alfvén eigenmode induced fast ion transport and loss in DIII-D and ASDEX Upgrade". In: *Physics of Plasmas* 18.5 (May 2011), p. 056114. ISSN: 1070-664X, 1089-7674. DOI: 10.1063/1.3574663.

[70] R. J Goldston et al. "New techniques for calculating heat and particle source rates due to neutral beam injection in axisymmetric tokamaks". In: *Journal of Computational Physics* 43.1 (Sept. 1981), pp. 61–78. ISSN: 0021-9991. DOI: 10.1016/0021-9991(81)90111-X.

[71] Alexei Pankin et al. "The tokamak Monte Carlo fast ion module NUBEAM in the National Transport Code Collaboration library". In: *Computer Physics Communications* 159.3 (June 2004), pp. 157–184. ISSN: 0010-4655. DOI: 10.1016/j.cpc.2003.11.002.

[72] R. V. Budny et al. "Local transport in Joint European Tokamak edge-localized, high-confinement mode plasmas with H, D, DT, and T isotopes". In: *Physics of Plasmas* 7.12 (Nov. 2000), pp. 5038–5050. ISSN: 1070-664X. DOI: 10.1063/1.1320466.

[73] O. Meneghini et al. "Integrated modeling applications for tokamak experiments with OMFIT". In: *Nuclear Fusion* 55.8 (July 2015), p. 083008. ISSN: 0029-5515. DOI: 10.1088/0029-5515/55/8/083008.

[74] D. W. Swain and G. H. Neilson. "An efficient technique for magnetic analysis of non-circular, high-beta tokamak equilibria". In: *Nuclear Fusion* 22.8 (Aug. 1982), pp. 1015–1030. ISSN: 0029-5515. DOI: 10.1088/0029-5515/22/8/002.

[75] J. L. Luxon and B. B. Brown. "Magnetic analysis of non-circular cross-section tokamaks". In: *Nuclear Fusion* 22.6 (June 1982), pp. 813–821. ISSN: 0029-5515. DOI: 10.1088/0029-5515/22/6/009.

[76] L. L. Lao et al. “Reconstruction of current profile parameters and plasma shapes in tokamaks”. In: *Nuclear Fusion* 25.11 (1985), p. 1611. ISSN: 0029-5515. DOI: 10.1088/0029-5515/25/11/007.

[77] S. E. Parker and W. W. Lee. “A fully nonlinear characteristic method for gyrokinetic simulation”. In: *Physics of Fluids B: Plasma Physics* 5.1 (Jan. 1993), pp. 77–86. ISSN: 0899-8221. DOI: 10.1063/1.860870.

[78] E. D. Fredrickson et al. “Suppression of Alfvén Modes on the National Spherical Torus Experiment Upgrade with Outboard Beam Injection”. In: *Phys. Rev. Lett.* 118 (26 June 2017), p. 265001. DOI: 10.1103/PhysRevLett.118.265001. URL: https://link.aps.org/doi/10.1103/PhysRevLett.118.265001.

[79] E. Belova et al. “Validation of GAE simulation and theory for NSTX(-U) and DIII-D”. In: *28th IAEA Fusion Energy Conference (FEC 2020)*. Virtual, 2021.